UNIVERSITY OF CALIFORNIA
RIVERSIDE

Nonlinear Magnetization Dynamics in Nanoscale Confined Ferromagnets

A Dissertation submitted in partial satisfaction
of the requirements for the degree of

Doctor of Philosophy

in

Physics

by

Arezoo Etesamirad

March 2023

Dissertation Committee:

Dr. Igor Barsukov, Chairperson
Dr. Peng Wei
Dr. Roya Zandi

The Dissertation of Arezoo Etesamirad is approved:

Committee Chairperson

University of California, Riverside

Acknowledgments

Graduate school is a challenging but incredibly rewarding experience. It is a time filled with growth, friendship, and endless opportunities for learning. However, this would not have been possible for me without the individuals who helped me through this journey. I would like to take this opportunity to acknowledge all the people who have helped and supported me during these years.

First of all, I would like to express my heartfelt gratitude to my advisor, Prof. Igor Barsukov, for his resolved support, guidance, and insightful comments. His dedication to his students and his commitment to their success are a true testament to his character and professionalism. I am grateful for the opportunity to have had you as my advisor, and I will always remember the impact you have had on my life.

I would also like to thank my committee members, Dr. Roya Zandi and Dr. Peng Wei, for their time and effort in reviewing my dissertation. I would like to extend my sincere gratitude to Dr. Roman Verba, Dr. Jordan Katine, Dr. Ilya N. Krivorotov, Dr. Vasyl Tyberkevych, and Dr. Boris Ivanov. It was a pleasure to work with you. Your expertise and insights have added valuable perspectives to my research and made my projects stronger as a result.

I would like to thank Dr. Bassim Arkook, who was my mentor when I joined the lab. You taught me all the measurement and data analysis techniques patiently and were always there to answer my questions.

I would like to thank Rodolfo Rodriguez and Shirash Regmi for not only providing a supportive and collaborative environment at work but also for their friendship.

Your friendship, technical assistance, and shared passion for our research have made this experience truly enjoyable. I will always cherish the friendships I have formed with you.

I would also like to thank my other labmates: Joshua Bocanegra, David Nelson, Diego Camacho, Allison Tossounian, Travis Crumpton, Eric Hegan, Henry Woodington, Xian Wang, Rundong Jiang, and Sasha Korotneva for their friendship and the interesting discussions we had.

The past six years in Riverside have been some of the most wonderful times of my life, spending time with my supportive friends. I would like to thank all of them: Amin Safdari, Mahsa Servati, Marziye Jafariyazdani, Hodjat Asghari Esfeden, Hoda Naghibi, Valeh Ebrahimi, MohammadAmin Baniasadi, Sajjad Bahrami, Fahimeh Arab, Mohsen Karimi, Rasoul Ghadami, Yasin Mazloumi, Maryam Shahcheraghi, mahdi Kohansal, Sanaz Panahandeh, Negin Entezari, AmirAli Darvishzadeh, Shirin Masoumi, Shabnam Etemadi, Rabi Rad, Arash Mehrkesh, Mahbod Affarin, and Zahra Nataj.

Most importantly, I want to give my deepest thanks first to my parents, Narges Etesamirad and Mahmood Etesamirad, for their unconditional love and support. Their faith in me and my abilities has been a source of strength and motivation during the most challenging times of my academic journey. Although being on the other side of the planet may separate us physically, your love and support will always be with me. Thank you, Maman and Baba, for everything. Second to my little sister, Aida, I am so blessed to have you in my life. Thanks for your insignificant love and encouragement.

Last but not least, I would like to say thank you to my husband, Alireza, who has been my constant source of support and encouragement throughout my PhD journey. Your

unwavering love, patience, and understanding have given me courage. This achievement would not have been possible without you. Thank you for always being there for me; I love you!

To my beloved spouse, my lovely sister, and my dear parents.

ABSTRACT OF THE DISSERTATION

Nonlinear Magnetization Dynamics in Nanoscale Confined Ferromagnets

by

Arezoo Etesamirad

Doctor of Philosophy, Graduate Program in Physics
University of California, Riverside, March 2023
Dr. Igor Barsukov, Chairperson

The nonlinear magnetization dynamics in zero-dimensional magnets have received increasing attention in recent years due to their potential applications in high-density data storage and spintronic devices. It also shows parallels to AMO physics, nonlinear optics, quantum information systems, and even some astrophysical phenomena. Magnon scattering processes, which constitute a major dissipation channel in nanomagnets, play a major role in determining the energy efficiency of spintronic applications.

In this work, first I report an experimental observation of different kinds of magnon-magnon interactions affecting the magnetic damping within the nanomagnet. I focus on predominant nonlinear magnon scattering processes in nanomagnets, including degenerate and non-degenerate three magnon scattering and degenerate four magnon scattering. To do the experiment, I implement magnetic tunnel junction (MTJ) nanodevices, consisting of a free layer and a synthetic antiferromagnet at their core. It is shown these nonlinear processes can redefine and invert the nanomagnet's response to spin torques. A theory is established to explain this counter-intuitive effect, demonstrating the damping parameter

of a spin wave stops being frequency-independent and becomes a resonant function of the excitation frequency.

Controlling magnon processes and thus magnetic damping is the key to improving the performance of future computer systems. In this regard, I propose an approach for controlling magnon scattering by a nanoscale dipole switch. I demonstrate an experimental proof-of-concept in MTJ nanodevices. By triggering the spin-flop transition in the synthetic antiferromagnet and utilizing its dipole field, a three-magnon process in the free-layer is toggled. The switching of the synthetic antiferromagnet allows for controllably tuning the strength of the magnon interaction by at least one order of magnitude, leading to two distinct dissipative states.

Additionally, I study the magnetic switching of a nanoscale synthetic antiferromagnet (SAF) with a perpendicular order parameter incorporated in a MTJ structure. I drive the MTJ with microwave pulses and observe spin-flip switching of the SAF by resonant excitation of an individual magnon mode of the SAF. The magnon spectrum of the nanoscale SAF is discrete. Evaluation of the switching probability distributions shows that various modes from this spectrum can facilitate the switching. Moreover, it suggests a substantial contribution of the thermal spin-torque.

Finally, I investigate the electric noise in MTJs whose understanding is a prerequisite for employing them in next-generation applications. I observe random telegraph noise, which is frequently found in MTJs but not yet fully understood. By varying the temperature in the range of 80–300 K for an MTJ in the parallel state, we encounter anomalous device resistance (steps) attributed to magneto-structural phase transitions of iron oxide clusters

at the CoFeB/MgO interface. At temperatures of these anomalies, telegraph noise shows a significant increase. This correlation suggests that the oxide clusters have a significant impact on MTJ noise characteristics.

Contents

List of Figures

Chapter 1

Introduction

1.1 Motivation

This dissertation presents a study on the nonlinear dynamics of magnetization in zero-dimensional ferromagnets. This is an exciting topic of fundamental science which shows parallels to many other subfields of physics and has direct benefits for state-of-the-art technology. In magnets, collective spin excitations, known as spin waves[1], are quantized into magnons. Interactions between the magnons govern the magnetization dynamics. For instance, magnon processes result in nonlinear magnetic dissipation and determine the energy consumption of magnet-based applications. Controlling magnon processes is thus the key to improving the performance of spintronic applications.

Additionally, magnon processes offer a promising means of information processing and storage in both neuromorphic and quantum information systems due to their potential for low-power consumption and high-coherence properties. Magnons can be used in neuromorphic systems [2, 3, 4] as a means of information transfer and processing. For example,

magnon-based spin-wave logic gates have been proposed as a way to perform computation in a neuromorphic architecture. In quantum information systems, magnons can also play a role as a potential medium for quantum information storage and processing in which magnons in certain materials with long coherence times, are used as qubits in a quantum computing architecture. Interactions between magnons can also be utilized to perform quantum gates, opening the possibility of implementing a magnon-based quantum computing system.

Nonlinear magnetization dynamics in nanomagnets have long remained elusive, mainly due to the lack of sensitive spectroscopy techniques and nanofabrication challenges, hindering technological progress and delaying the development of the pertinent theoretical framework. With recent advances in experimental methods, I take the opportunity to tackle this research field.

To study nonlinear spin dynamics, I employ nanoscale magnetic tunnel junctions (MTJs), which consist, at their core, of two magnetic discs separated by an ultrathin insulating tunneling barrier used for tunneling magnetoresistance. The MTJ devices are the basic constituents of the flagship spintronic technologies used in Magnetic Random Access Memory (MRAM) to create non-volatile memory cells, which retain their stored information even when power is removed [5]. They can also be used to create magnetic sensors with a wide range of applications, including in navigation systems, automotive applications, and biomedical devices. Furthermore, MTJs can be used to create logic devices [6], such as spin-transfer torque logic gates, which use the spin-transfer torque effect to perform computations.

I use highly sensitive microwave spectroscopy techniques, spin torque ferromagnetic resonance (ST-FMR) and microwave emission spectroscopy, to investigate the nonlinear processes in MTJs which serve as a sample platform for zero-dimensional spin systems. The goal of my research is to understand and control nonlinear physics and to help develop faster and more energy efficient computers for the future.

1.2 Outline

This dissertation is structured as follows:

Chapter 2 presents an overview of magnetic tunnel junctions (MTJs) as a sample platform for nano-magnets, which have been utilized to investigate magnetization dynamics in this dissertation. The subsequent sections of the chapter provide a theoretical foundation for understanding magnetization dynamics in the presence of spin-torque, as well as a discussion of nonlinear contributions to magnetic damping that are pertinent to the research presented in this dissertation.

Chapter 3 introduces the experimental techniques employed to obtain the results presented in this dissertation. These techniques include magnetotransport measurements, spin-torque ferromagnetic resonance (ST-FMR), microwave emission spectroscopy, and noise spectroscopy methods.

Chapter 4 presents an examination of the discrete magnon spectrum of zero-dimensional magnets and identifies the inherent inter-magnon processes. The study found that resonant magnon processes have a significant impact on a nanomagnet's response to spin-torque. The mechanisms of this interaction between nonlinearity and spin-torque were

investigated, and it is believed to have far-reaching implications for the performance of magnetic memory and oscillators.

Chapter 5 describes an approach we utilized for engineering magnon interaction through the use of symmetry-breaking fields with nanoscale nonuniformity [7]. A nanoscale synthetic antiferromagnet was utilized as a switchable source of such fields, and the study achieved a tunability of magnon coupling by at least one order of magnitude. This has a significant impact on enhancing the energy efficiency of spintronic applications, controlling nonlinear response in neuromorphic networks, and promoting coherent magnon coupling for quantum information.

Chapter 6 describes my work in which I investigated the magnetic switching of a nanoscale synthetic antiferromagnet (SAF) with a perpendicular order parameter incorporated in a magnetic tunnel junction structure. I drove the MTJ with microwave pulses and observed spin-flip switching of the SAF by resonant excitation of an individual magnon mode of the SAF. The magnon spectrum of the nanoscale SAF is discrete. Evaluation of the switching probability distributions showed that various modes from this spectrum can facilitate the switching. Moreover, it suggested a substantial contribution of the thermal spin-torque. The results pave the way toward energy-efficient SAF-based applications and open avenues for functionalizing SAFs in nanoscale heterostructures.

Chapter 7 presents a collaborative investigation in which a correlation between electric noise and resistance anomalies in MTJs is discovered. This correlation suggests the presence of magneto-structural phase transitions in Iron-Cobalt-Oxide nanoclusters at the interface between the free layer and the tunneling layer in MTJs.

Chapter 8 represents a summary of the dissertation.

Chapter 2

Background Material and Formulation of Theoretical Framework

2.1 Background of spintronics

The 20th century saw a surge in technological development driven by the creation and improvement of electronic devices. The performance of these devices is based on the manipulation of the electrical charge. These devices have become essential for information technology applications by allowing for precise control over the flow of electrons. However, in addition to having a charge, an electron also has a spin of 1/2, meaning that a flow of electrons is not only a flow of charges (charge current), but it also potentially carries inner angular momentum (spin current[8]) if the electrons have a predominant spin direction.

Spintronics is a field of study that has emerged in recent decades, focusing on the manipulation of magnetization through spin current. This field combines and explores the two fundamental properties of electrons: charge and spin.

The term "spintronics" was first introduced in 1991 by scientists at Bell Telephone Laboratories [9], and since then, it has seen significant growth. The angular momentum of an electron, also known as spin, can be controlled by external means, allowing researchers to control the flow of electrons through a material. This makes spintronics a promising area for developing new applications in electronics, computing, and communication.

The advantages of spintronics over traditional electronics are numerous. Spintronic devices consume less energy and switch faster than conventional electronics. This is due to the fact that their operations are not limited by the flow of electrons but rather by the speed of their spin. This makes spintronic devices much more suitable for high-speed applications. Spintronic devices are also non-volatile, meaning they can retain their data even when the power is turned off. This makes them ideal for use in applications where data storage and retrieval are important, such as memory cards and hard drives.

One good example of spintronics application is spin valves, and more particularly, nanoscale Magnetic Tunnel Junctions (MTJs). The MTJ devices are at the forefront of spintronics technology: they are being developed for spin-torque memory [10, 11, 12, 13, 14], magnetic field sensors, microwave oscillators and detectors [15, 16, 17, 18], neuromorphic networks [2, 3, 4], and many other applications. In the following sections, I will discuss the fundamentals of spintronics, focusing on MTJs, the tunneling magnetoresistance effect, and the spin transfer torque effect [10]. In addition, I will describe the magnetization dynamics

[19] in the presence of spin-torque and the contribution of magnetic damping [20], which will serve as background information for the remainder of this dissertation.

2.2 Types of magnetoresistance

In magnetic materials, the magnetization direction influences the movement of electrons within the material, thereby altering the electrical resistance of the device. This phenomenon is observed in ferromagnets and is referred to as magnetoresistance (MR) effect. When electrons pass through a ferromagnetic material, the spin of the electrons influences the probability of their scattering, resulting in the MR effect. There are several types of magnetoresistance effects that can occur, either in single magnetic materials (e.g. anisotropic magnetoresistance) or multilayer systems (e.g. giant magnetoresistance and tunneling magnetoresistance).

Anisotropic Magnetoresistance (AMR) is a form of magnetoresistance effect that is caused by the anisotropic scattering of conduction electrons due to spin-orbit interaction [21]. This effect is dependent on the angle between the magnetization direction and the current flow direction in ferromagnetic films. In many materials, when the magnetization of a ferromagnet is parallel to the electrical current direction, the resistance is at its maximum. When the magnetization is perpendicular to the current flow direction, the resistance is at its minimum.

In the 1960s, researchers made a remarkable discovery that the electrical resistance of a material can be significantly altered by the presence of a magnetic field, even when the material itself is not magnetic but is in close proximity to a magnetic substance. This led

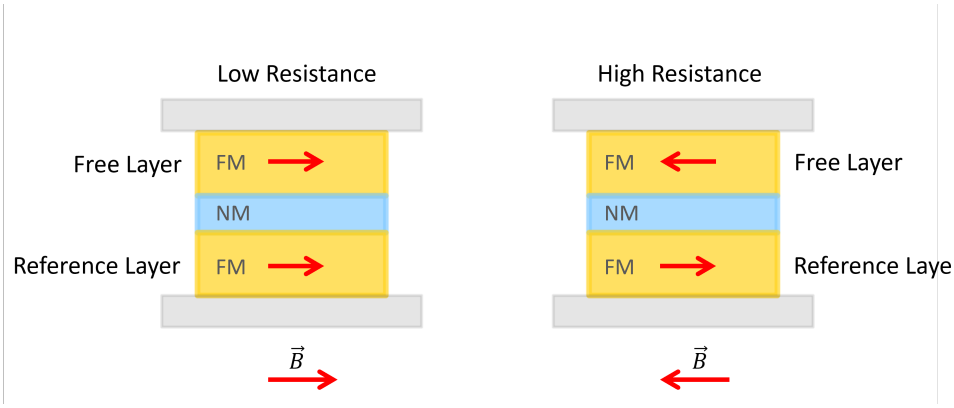

Figure 2.1: Structure of spin valve.

to the development of spin valves [22]. Spin valves are a type of magnetoresistive device that can detect and measure small magnetic fields. The structure of these devices consists of two or more magnetic layers separated by non-magnetic spacer material, the electrical resistance of which is dependent on the relative magnetization orientation of the magnetic layers shown in figure 2.1.

In particular, the field of spintronics received wide attention with the discovery that the electric current in a multilayer film, consisting of a sequence of thin magnetic layers separated by a thin non-magnetic layer, is strongly influenced by the relative orientation of the magnetization of the magnetic layers. Thus, it is important to understand the spin-dependent processes in magnetic multilayer structure.

When a magnetic field is applied to a spin valve, the magnetization of the layers align with the external field. As a consequence, the multilayer resistance drops. In the absence of a magnetic field, the magnetization directions are not parallel and the multilayer resistance is large.

In applications, the direction of magnetization in one ferromagnetic layer is usually fixed, and the direction of magnetization in the other layer is determined by the external field. Spin valves can be designed in such a way that they operate between two states: maximum resistance when the magnetizations of two ferromagnetic layers are antiparallel and minimum resistance when they are parallel. When the spacer is metallic, this phenomenon is known as giant magnetoresistance (GMR) [23]. In general, the resistance of a GMR structure with a relative angle between the two layers, θ, is given by:

$$R(\theta) = R_P + (R_{AP} - R_P)cos\theta \tag{2.1}$$

The GMR effect's origin refers to the spin-dependent scattering at the interfaces between ferromagnetic and metal layers. The difference in resistance between the maximum and minimum values can be as high as a few 10's of percent, which is significantly more than the anisotropic magnetoresistance ($\sim 1\%$) in metals, which is the reason for its name, "Giant Magnetoresistance."

With technological advancements, much effort has been put into improving the sensitivity of GMR-based applications, which has led to the development of a new type of spin valve based on the tunneling magnetoresistance (TMR) effect: Magnetic Tunnel Junctions (MTJs). The magnetic structure of a TMR element is nearly the same as that of a GMR element. However, in a TMR element, the metallic spacer is replaced by an insulator barrier, and currents flow perpendicular to the film surface, whereas in a GMR element, currents can flow either in-plane or perpendicular to the film surface. The subsequent sections provide further information on MTJs and the TMR effect.

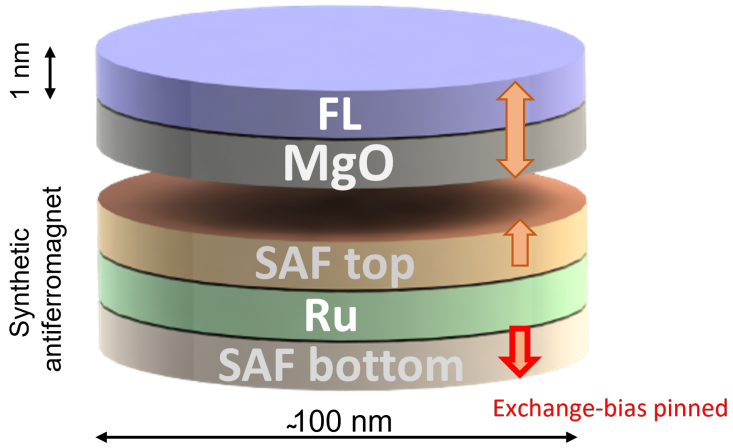

Figure 2.2: Structures of a magnetic tunnel junction nanopillar.

2.3 Nanoscale magnetic tunnel junctions (MTJs)

The nonmagnetic metallic layer in a GMR structure can be replaced by an insulating layer. The insulating layer, which is typically made of MgO or aluminum oxide, acts as a tunnel barrier for electron transport and reduces interlayer coupling between two ferromagnetic layers. This structure, known as a magnetic tunnel junction (MTJ), is one of the most fundamental and important spin-based devices. One of the ferromagnetic layers in the MTJ is known as the "free" layer because its magnetization is sufficiently decoupled from the other magnetic layers and can be easily changed by applying an external magnetic field, whereas the other has a "fixed" or "pinned" magnetic orientation. Figure 2.2 depicts the structure of an MTJ.

One way to pin the pinned layer is to provide a unidirectional anisotropy via an exchange bias interaction with an adjacent antiferromagnetic layer, which pins the ferromagnetic (FM) layer into a predefined direction as long as the external field does not exceed

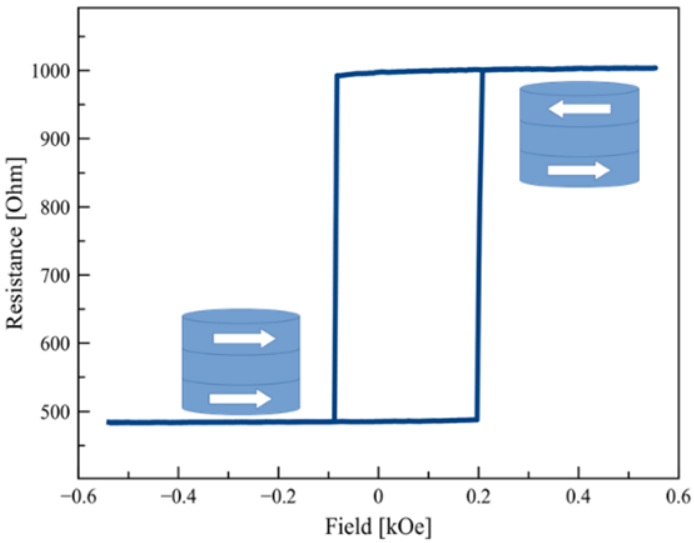

Figure 2.3: Tunneling magetoresistance of MTJ. When the magnetization of the FM layers is parallel, the majority spin electrons are transmitted more easily than the minority spin electrons, resulting in a low-resistance state. When the magnetization of the layers is antiparallel, the majority of spin electrons are blocked, resulting in a higher resistance state.

the pinning strength. By introducing two more layers, that constitute a Ruderman-Kittel-Kasuya-Yosida (RKKY) coupled [24] "synthetic antiferromagnet" (SAF), the dipole field between FM layers can be compensated.

2.3.1 Tunneling magnetoresistance (TMR)

MTJs are of particular interest to us due to a magnetotransport phenomenon known as Tunneling Magnetoresistance (TMR). TMR is a quantum mechanical effect that describes the dramatic change in resistance of an FM/insulator/FM metallic multilayer structure as the relative orientation of two FM layers changes [25]. Figure 2.3 shows that

the resistance is lowest when the magnetization of the two ferromagnets is parallel and highest when it is antiparallel.

TMR originates from spin-dependent tunneling [22]. Electrons get polarized when they go through the first ferromagnetic layer. Because the barrier is so thin, electrons can tunnel through it. The spin of the electrons dictates the probability of them tunneling through the barrier. It follows, then, that tunneling of up and down spin electrons is two distinct processes. When two ferromagnetic films are magnetized in parallel, minorities tunnel to minorities and majorities tunnel to majorities without being strongly scattered. However, when the two films are magnetized antiparallel, the identities of the majority- and minority-spin electrons are reversed, allowing the majority spins of the first film to tunnel to the minority states of the second film and vice versa (figure 2.4).

TMR is explained by the Julliere model [26] under the assumption that the conductance for a specific spin orientation is proportional to the product of the effective densities of states of the two ferromagnetic electrodes:

$$G_P \propto \rho_{1\uparrow}\rho_{2\uparrow} + \rho_{1\downarrow}\rho_{2\downarrow} \tag{2.2}$$

$$G_{AP} \propto \rho_{1\uparrow}\rho_{2\downarrow} + \rho_{1\downarrow}\rho_{2\uparrow} \tag{2.3}$$

Where $\rho_{1\uparrow}$ and $\rho_{1\downarrow}$ ($\rho_{2\uparrow}$ and $\rho_{2\downarrow}$) are the density of states at the Fermi level of the majority and minority spins of the first (second) FM layer. By definition, the spin polarization P is

$$P = \frac{\rho_\uparrow - \rho_\downarrow}{\rho_\uparrow + \rho_\downarrow} \tag{2.4}$$

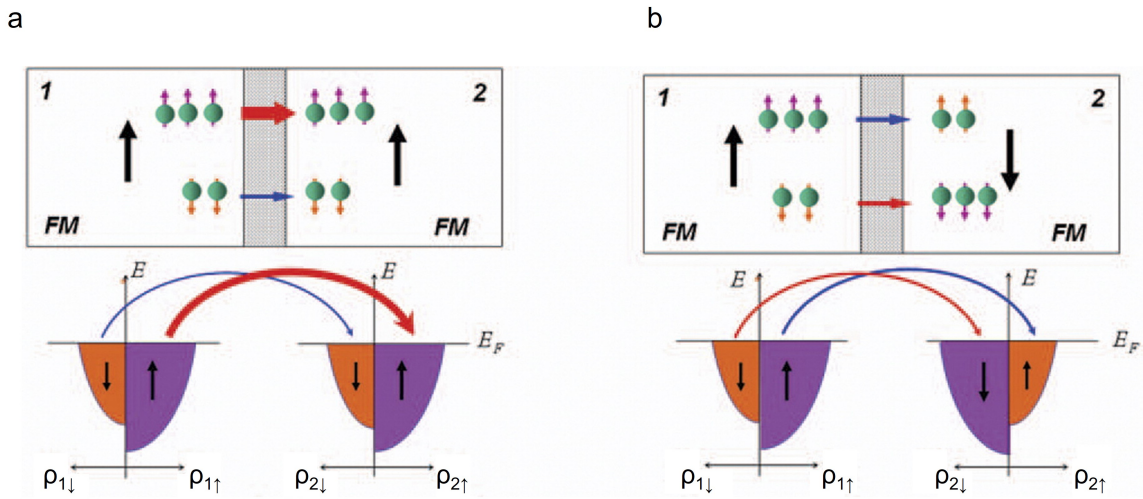

Figure 2.4: Spin-dependent tunneling across the tunnel barrier of two ferromagnets for (a) parallel and (b) antiparallel configurations. Adapted with permission from [27].

Therefore, the tunneling magnetoresistance ratio will be

$$TMR = \frac{\Delta R}{R} = \frac{R_{AP} - R_P}{R_P} = \frac{G_P - G_{AP}}{G_P} = \frac{2P_1P_2}{1 - P_1P_2} \tag{2.5}$$

where R_{AP} and R_P are the resistance of the multilayer film in antiparallel (AP) and parallel (P) configurations, respectively.

Nowadays, CoFeB/MgO/CoFeB junctions can achieve TMR values of 600% at room temperature [28], which is significantly higher than MR in the GMR-based devices. The increased sensitivity should enable MTJ read heads to either detect data stored in smaller bits or scan the same-sized bits more quickly, making them desirable for memory applications.

2.3.2 In-plane and out-of-plane systems

Magnetic anisotropy, which is represented by magnetic anisotropy energy, determines whether the magnetization direction within a ferromagnet film is confined to the plane or perpendicular to the plane. Magnetization prefers to align in the direction that minimizes energy, known as the "easy axis", and resists alignment in the direction that maximizes energy, known as the "hard axis" [24]. There are several contributions to magnetic anisotropy, including magnetocrystalline anisotropy, uniaxial anisotropy, shape anisotropy, exchange anisotropy, induced anisotropy, and perpendicular magnetic anisotropy.

Magnetocrystalline Anisotropy is the intrinsic cause of anisotropy. This occurs due to the coupling of the crystal lattice to the spins of the electrons (spin-orbit interaction). As a result, the crystal lattice of an object affects its preferred magnetization direction [24, 29, 30]. For example, the expression for energy in a cubic crystal is:

$$E_{mc} = K_1(\alpha_1^2\alpha_2^2 + \alpha_2^2\alpha_3^2 + \alpha_3^2\alpha_1^2) + k_2(\alpha_1^2\alpha_2^2\alpha_3^2) \tag{2.6}$$

where α_i are the direction cosines of the magnetization, and K_1 and K_2 are the first and second order anisotropy constants.

Shape Anisotropy: Demagnetization Field originates from magnetostatic energy. In magnetic materials, the surface magnetic charge distribution operates so as to oppose the internal magnetization, which is known as the demagnetization field [24]. In non-spherical materials where the demagnetizing factors are not the same in all directions, this results in at least one easy axis or easy plane. For example, in an ellipsoid, the demagnetizing

field will be smaller if the magnetization is along the long axis as opposed to one of the short axes. This produces an easy axis of magnetization along the long axis.

Exchange Anisotropy or **Exchange Bias** occurs when a ferromagnetic material is placed in close proximity to an antiferromagnetic material, leading to an exchange contribution to anisotropy energy and a shift in its hysteresis loop towards the antiferromagnetic layer [24]. This shift is due to a unidirectional anisotropy and is evidenced by a change in the coercivity and saturation magnetization of the ferromagnetic material, referred to as an exchange bias field. Exchange bias fields are advantageous in applications such as spin-valves and magnetic tunnel junctions where their properties allow for the stabilization and pinning of the reference layer's magnetization.

Induced Anisotropy happens when an easy direction of magnetization is made by applying stress or by depositing or annealing a disordered alloy in a magnetic field [24].

Perpendicular Magnetic anisotropy (PMA) is dominant when the ferromagnetic film becomes thiner and the role of surface becomes significant [24, 31]. A film's magnetization prefers to be in-plane as a result of the demagnetization field. At an interface, however, an electron orbital may significantly deform toward the interface. As a result of this deformation, the spin-orbit interaction is significantly amplified, producing a large effective magnetic field when the magnetization is along the deformation (perpendicular-to-interface). The energy density of perpendicular magnetic anisotropy (PMA) is:

$$E_{PMA} = -K_{\perp} cos^2(\theta) \tag{2.7}$$

where $K_\perp$ is the PMA constant and can be positive or negative depending on the interface. This surface anisotropy decreases with film thickness as 1/d.

2.4 Magnetization dynamics

The dynamics of magnetization in a magnetic medium is generally described by the Landau-Lifshitz (LL) equation [32, 33]. This differential equation produces solutions describing the precessional motion of magnetization. It has been introduced as:

$$\frac{d\mathbf{M}}{dt} = -\gamma \mathbf{M} \times \mathbf{H_{eff}} - \lambda \mathbf{M} \times (\mathbf{M} \times \mathbf{H_{eff}}) \tag{2.8}$$

where γ is the absolute value of the gyromagnetic ratio [34] defined as $\gamma = |\frac{ge}{2m_e c}|$, and $\mathbf{H_{eff}}$ is the total effective field including the applied field ($\mathbf{H_{applied}}$) and the anisotropy field ($\mathbf{H_{anis}}$). λ is a phenomenological damping parameter which is equal to the inverse relaxation time, $\lambda = \frac{1}{\tau} \sim \alpha \frac{\gamma}{M_s}$, where α is the Gilbert damping factor and and M_s is the saturation magnetization. In 1995 Gilbert described magnetization dynamics by using the dimensionless damping parameter (α) within the Landau-Lifshitz-Gilbert equation:

$$\frac{d\mathbf{M}}{dt} = -\gamma \mathbf{M} \times \mathbf{H_{eff}} + \frac{\alpha}{M} \mathbf{M} \times \frac{d\mathbf{M}}{dt} \tag{2.9}$$

The first term on the right represents the precessional torque (τ_H) as illustrated in figure 2.5. It describes that a free magnetization subject to an effective magnetic field will precess about that field. The second term is the non-conservative damping torque

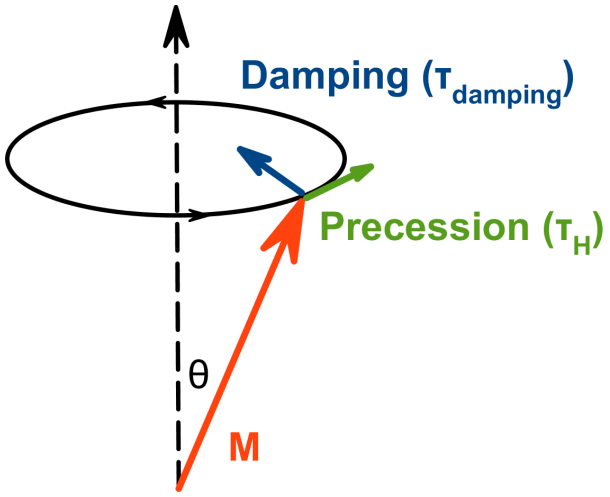

Figure 2.5: Direction of torques presented in the magnetic system.

($\tau_{damping}$) which characterizes the energy dissipation and, without any excitation, tends to align magnetization with the effective field direction.

2.5 Spin-transfer torque

The magnetization of the ferromagnetic layers influences the transport property of the spin-polarized electrons (as discussed in the TMR effect). Spin-polarized electrons, on the other hand, can exert torque on ferromagnets via angular momentum transfer. This "spin transfer torque" effect was first predicted by Slonczewski [35] and Berger [36] in 1996. This torque can be strong enough to reverse the magnetization of a nanomagnet or excite the persistent procession of the magnetic moment. The spin transfer effect provides an efficient way to manipulate the magnetic moment of a nanoscale magnet, which not only

generates much interest in its technological applications but also enables novel studies of magnetic dynamics.

The spin transfer effect, as depicted in figure 2.6, can be realized as a spin-polarized electron enters a ferromagnet whose magnetization is in a direction non-collinear to the electron spin. Consider a randomly spin oriented electron passing through a ferromagnet (FM_1); the ferromagnet polarizes the electron's spin, so the direction of spin moment $\mathbf{p}$, is the same as FM_1. The spin-polarized current passes through the nonmagnetic spacer layer, retaining its polarization as it enters the second ferromagnetic layer FM_2, where it is subjected to the local exchange field along the magnetization of FM_2 ($\mathbf{m_2}$) and become repolarized along $\mathbf{m_2}$. The net change in the spin-polarization of electrons results the net change of spin moment of the current, $\mathbf{\Delta p} = \mathbf{p_{out}} - \mathbf{p_{in}}$. Due to the conservation of angular momentum, the ferromagnet must absorb this component, the net change of current moment $\mathbf{\Delta p}$ gives rise the spin torque $\sim \tau_{\mathbf{st}}$ in the opposite direction ($\tau_{\mathbf{st}} = -\Delta\mathbf{p}$), and in this way, the spin torque reorient magnetization of FM_2.

The maximum angular momentum one electron can transfer is $\hbar/2$ which seems to be a small value. However, for a small enough magnet, we can provide a sufficient amount of current in order to produce a strong enough torque to reverse its magnetization direction. The quantitative effect of spin torque can be described as follows:

$$\tau_{ST} = \gamma(\eta \frac{\hbar}{2e} \frac{J}{M_s t_{FM}})\mathbf{M} \times (\mathbf{M} \times \mathbf{M_{RL}}) \tag{2.10}$$

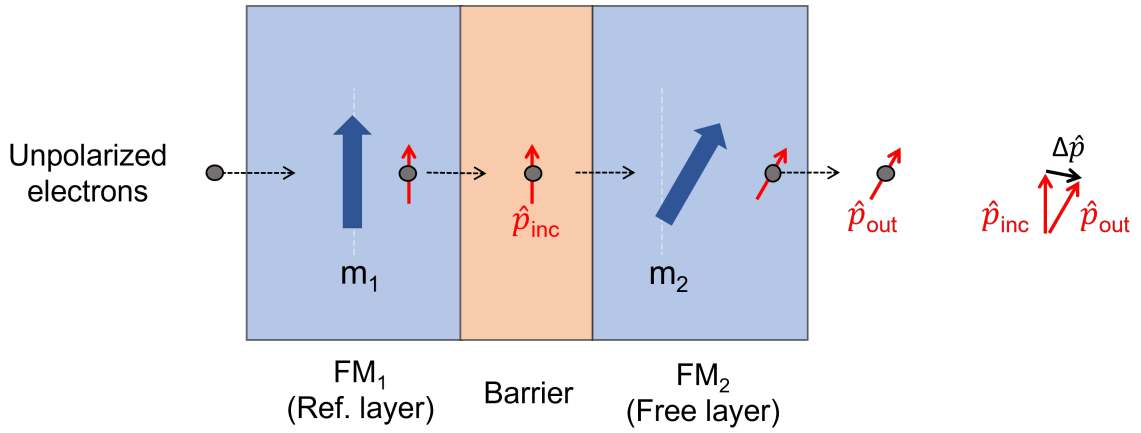

Figure 2.6: Illustration of the transfer of angular momentum when a spin polarized electron passes through a non-collinear ferromagnet.

Where $e = |e|$ is the electron charge, η is the spin torque efficiency, and $\mathbf{M_{RL}}$ refers to unit vector for the magnetization of reference layer, which induces spin polarization to the tunnel current that applies spin torque onto the unit vector for the magnetization of free layer $\mathbf{M}$. $\hbar$ is the reduced Planck constant, $J = I_{dc}/A_{FM}$ is the DC electrical density which flows through the free layer with a cross-sectional area of A_{FM} and a thickness of t_{FM}, M_s is the saturation magnetization of the free layer. Comparing Eqn. (2.10) with figure 2.6, M_{RL} and M corresponds to m_1 and m_2 respectively.

The magnetization dynamics under spin-torque can be described by LLG equation, see Eqn. (2.9), with an additional spin-torque term (τ_{ST}):

$$\frac{d\mathbf{M}}{dt} = -\gamma \mathbf{M} \times \mathbf{H_{eff}} + \alpha \mathbf{M} \times \frac{d\mathbf{M}}{dt} + \gamma(\eta \frac{\hbar}{2e} \frac{J}{M_s t_{FM}}) \mathbf{M} \times (\mathbf{M} \times \mathbf{M_{RL}}) \tag{2.11}$$

The Eqn. (2.10) is also called damping-like torque [37] because the term (τ_{ST}) directly modifies the damping torque (τ_d) in the LLG equation. For spin polarizations collinear

with the magentization direction, depending on the sign of the current, spin torque points either toward or away from the fixed layer moment or effective field.

2.6 Spin torque driven auto-oscillations

Spin torque auto-oscillators (STOs) are devices that use spin currents to generate persistent oscillations in the magnetization of a ferromagnetic material in the absence of a high-frequency external drive. Injecting the spin polarization current into the system causes the magnetization to precess around the effective field axis, resulting in the magnetization oscillating in a steady state [38].

In order to understand the influence of spin torque on magnetization dynamics, consider the damping and spin-torque terms in the LLG equation, Eqn. (2.11):

$$\tau_{\mathbf{d}} \sim -\mathbf{M} \times (\mathbf{M} \times \mathbf{H_{eff}}) \tag{2.12}$$

$$\tau_{\mathbf{ST}} \sim J\mathbf{M} \times (\mathbf{M} \times \mathbf{M_{RL}}) \tag{2.13}$$

The damping torque ($\tau_{\mathbf{d}}$) which characterizes the energy dissipation, leads the magnetization toward the equilibrium position, so that without any excitation the magnetization will relax back to the equilibrium. On the other hand, spin torque term ($\tau_{\mathbf{ST}}$), depending on the direction of electron flow (J), can act as damping or anti-damping torque, if the spin polarization (or its component) is collinear with the equilibrium magnetization of the oscillating layer.

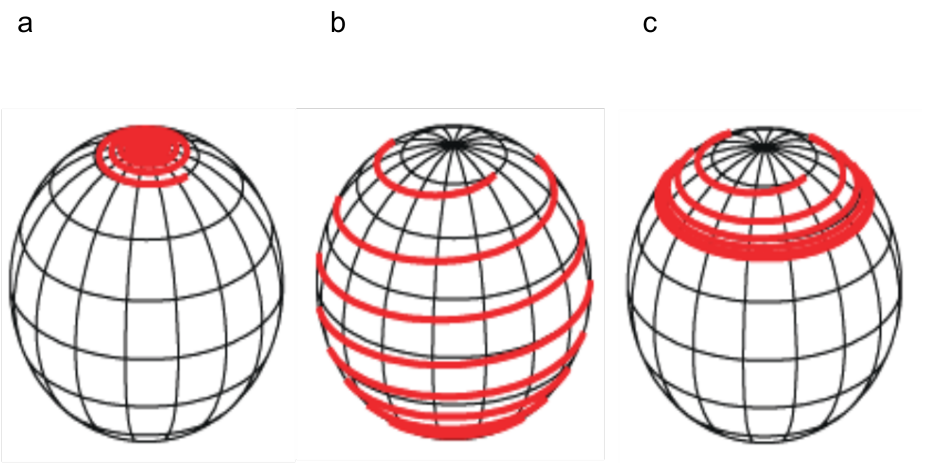

Figure 2.7: Configuration of spin-torque (a) acting like damping torque (b) triggering switching at high anti-damping current (c) causing auto-oscillation at critical current (J_c), Adapted with permission from [37].

In general, the magnetic dynamics excited by spin transfer torque can be categorized into three types: damping, switching, and persistent precession, as depicted in figure 2.7.

When the spin torque is in the same direction as the damping torque, it enhances the relaxation of the magnetization. When spin torque points away from the fixed layer's equilibrium state, it helps to destabilize the magnetization so that the magnetic moment of the free layer goes into a precession around the equilibrium axes. At low currents, the damping is only partially compensated, and therefore the magnetization, once tilted away from its equilibrium orientation, will precess back to its equilibrium direction, but at a smaller dissipation rate (figure 2.7 (a)).

When the current is large enough, the amplitude of the free layer precession grows until it reaches the energy barrier at around 90°. Once that happens, the damping torque

switches direction, orienting itself towards the other local energy minimum, and so a full reversal of the magnetization happens (figure 2.7 (b)).

In a third scenario, at a critical current (J_c), these two terms become equal, so magnetization undergoes a steady-state precession (figure 2.7 (c)), [16, 37]. It is worth noting that when there is no effective damping, the precession angle will continuously increase. However, nonlinear damping, which is naturally present in magnetic systems, acts as a stabilizing force and restricts the precession cone angle.

2.7 Nonlinear aspects of spin dynamics

The magnetic system is an intrinsically nonlinear system, and various nonlinear phenomena can be observed, especially at high levels of excitation. The threshold of nonlinearities can be easily reached, which makes the magnetic system a desirable model for studying nonlinear magnetodynamic phenomena. Nonlinearities remarkably affect the propagation characteristics of spin waves and give rise to a number of spectacular phenomena, such as the formation of solitons [39, 40] and the Suhl instability [41, 42] of the uniform precession of magnetization.

To understand nonlinearities, we must first understand magnon processes, which involve magnon interactions resulting in the creation, annihilation, and scattering of magnons. These interactions can facilitate the transfer of energy and angular momentum within magnetic systems, thereby influencing the damping behavior of the magnetic systems. Within a magnonic system, these magnon processes can generally be categorized into two distinct categories:

1. Multimagnon mode excitation [6] in the system couples to each other (magnon-magnon interaction) and redistributes energy among the magnon modes. These processes are intrinsic, can alter the response of a nanoscale spin-wave system significantly, and play a major role in magnetic dissipation [20].

2. Magnons couple to other parts of their physical environment: electrons [43], ionic impurities [44], and the lattice (spin-lattice interaction) [45]. The original magnons are eventually converted into phonons, either directly or indirectly.

In this work, we are investigating the first case, the magnon-magnon interaction and its nonlinear effect within nanomagnets, and aim to identify the source and explore how these interactions reshape the magnetization dynamics.

The interactions between magnons in magnetically ordered materials have been extensively studied theoretically [41]. In the absence of nonlinear effects (e.g. in extended films at low excitation), magnetic dissipation simply follows Gilbert damping and typically increases linearly with respect to the resonant frequency, as depicted in figure 2.8 (a). However, more complicated nonlinear cases are also possible, such as two-magnon scattering and Suhl instabilities. In extended ferromagnets, nonlinear interactions generally couple each spin wave eigenmode to a continuum of other modes [41] via energy- and momentum-conserving multi-magnon scattering. This kinematically allowed scattering limits the achievable amplitude of spin wave modes and leads to a broadening of the spin wave resonance [41].

In nanoscale ferromagnets, geometric confinement discretizes the spin wave spectrum, and thereby magnon-magnon scattering processes are not allowed kinetically. This

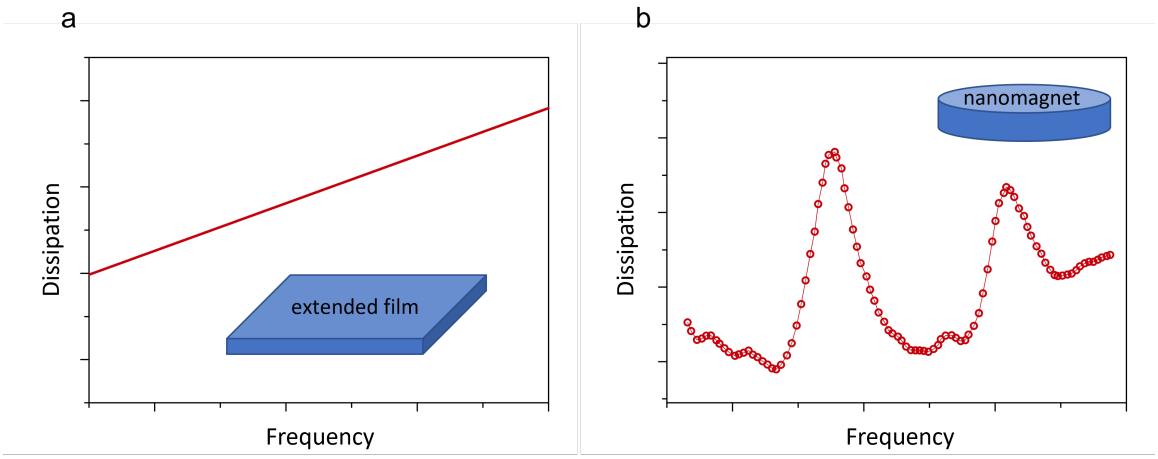

Figure 2.8: Spectral linewidth of a spin wave mode as a function of precessional frequency (a) In extended systems, spin waves' coupling increases the dissipation linearly. (b) In nanomagnets, discrete magnon modes interact with each other, increasing the magnetic damping nonlinearly.

suppression of nonlinear scattering enables the persistent excitation of spin waves with very large amplitudes [46], as observed in nanomagnet-based spin torque oscillators. Tunability of the spin wave spectrum by an external magnetic field, however, can lead to a restoration of the energy-conserving scattering [47]. The incidence and presence of magnon scattering within the nanomagnets have a strong nonlinear effect on magnetic dissipation and enhance the damping of the nanomagnet considerably, as depicted in figure 2.8 (b) [20, 48].

2.8 Three-magnon scattering

Resonant degenerate three magnon scattering and its giant nonlinear effect on magnetic dissipation has been studied before by Dr. Barsukov [20, 48]. This is fundamental background information that is imperative for my investigations into other forms of nonlinear magnon processes, such as non-degenerate three magnon scattering and degenerate four

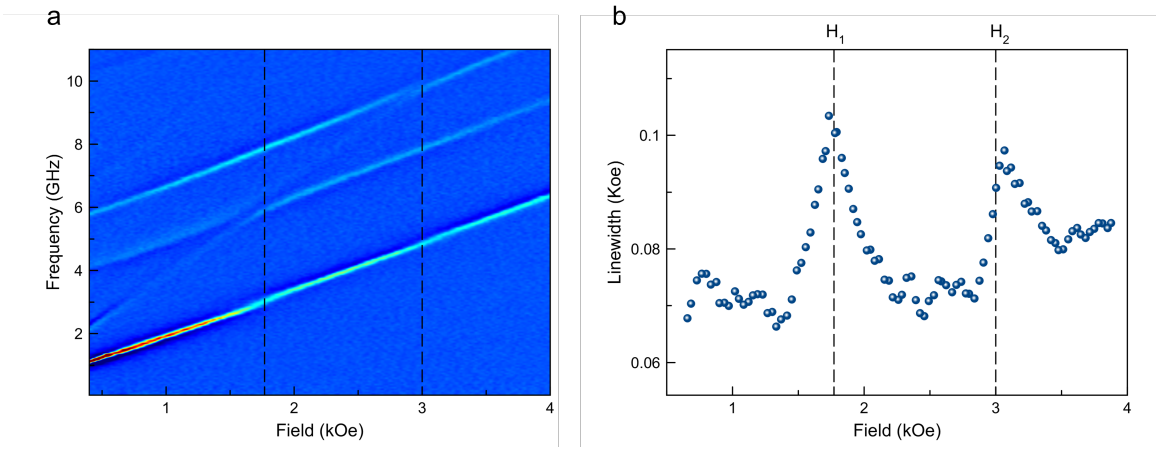

Figure 2.9: Spin wave eigenmodes of an out-of-plane MTJ device are measured as a function of magnetic field applied along easy axis. (b) The spectral linewidth of the lowest spin wave mode as a function of out-of-plane magnetic field. Linewidth is strongly enhanced in the three-magnon scattering regime at H_1 and H_2.

magnon scattering. The latter processes are analyzed both experimentally and theoretically in comprehensive detail in Chapter 4.

Three magnon scattering has been studied before in our lab [20, 48], and it has been shown that this kind of interaction has a major contribution to the magnetic dissipation. Implementing MTJs as a sample platform, the discrete magnon spectrum of zero-dimensional magnets is investigated, and the inherent inter-magnon processes are identified.

In figure 2.9, it is experimentally shown that the dissipation increases strongly at the specific fields where three magnon scattering is present. The frequency ratio of two modes at fields H_1 and H_2 is $f_i : f_j = 1 : 2$, which represents the energy is conserved at these specific fields and three magnon scattering is allowed kinetically. At these points, H_1 and H_2, two magnons of the lower-frequency mode $|i\rangle$ can confluence into one magnon of the higher mode $|j\rangle$, resulting in a degenerate three magnon (3m) process.

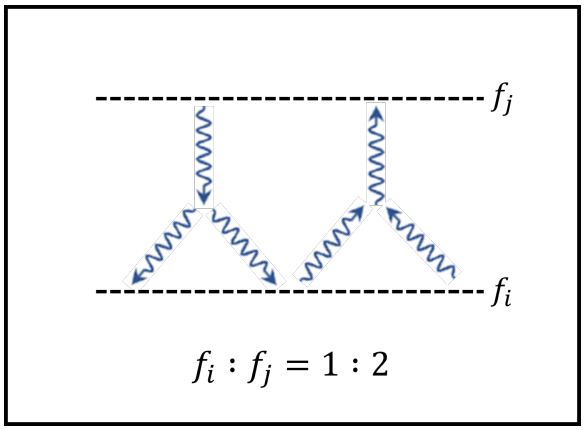

Figure 2.10: Schematic of three magnon confluence in which two magnons of a lower mode transmuted into a higher-order magnon mode or vice versa.

While manipulation of magnetization by spin torque is a key functionality of today's spintronics, the study [20, 48] shows that the nonlinearity corresponding to three magnon scattering significantly influences the reaction of the nanomagnet to spin torque. Antidamping spin-torque, which generally reduces the dissipation in nanomagnets, can enhance the damping in the presence of three magnon scattering [20, 48]. When the system is far from the three magnon regime, the antidamping spin-torque decreases dissipation as expected. However, in the three magnon regime, the nanomagnet's response to spin torque is redefined and inverted completely.

Furthermore, it is discussed that increasing antidamping spin-torque in the three magnon regime transforms a single-peak resonance lineshape into a split-peak lineshape with a local minimum at the resonance frequency $f = f_0$ [20, 48]. The data in figure 2.11 show that the unique split-peak lineshape in the resonance is only observed when (i) the energy conservation permits the three-magnon scattering of the quasi-uniform mode and (ii) The mode's amplitude is sufficiently large, verifying that the observed phenomenon is

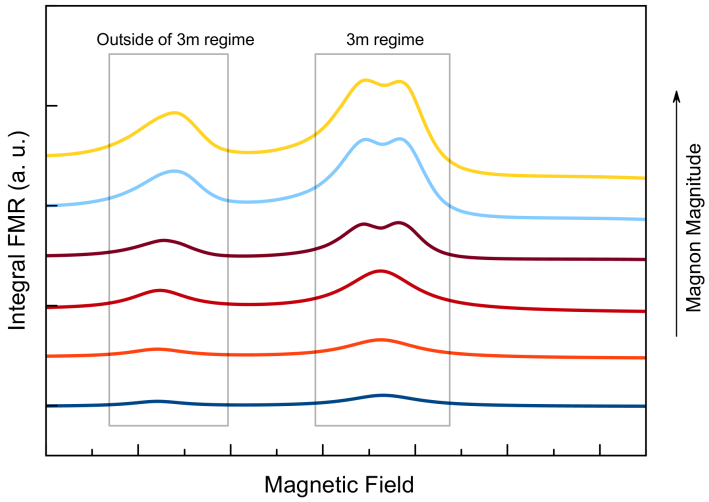

Figure 2.11: The normal spectral lineshape of spin wave resonance for various DC bias current values far from the magnon scattering regime versus anomalous spectral lineshape of the spin wave in the three magnon regime.

nonlinear and resonant in the frequencies of two modes engaging in three-magnon scattering [20, 48].

The theory to describe the nonlinear spin wave resonance in the nanoscale ferromagnet has been established in [20]. Consider a Hamiltonian that explicitly takes into account the nonlinear scattering between the quasi-uniform mode $|0\rangle$ and a higher-order spin wave mode $|n\rangle$:

$$\begin{aligned} H &= \omega_0 a^\dagger a + \omega_n b^\dagger b && \text{Two spin-wave mode} \\ &+ \frac{\Psi_0}{2} a^\dagger a^\dagger a a + \frac{\Psi_n}{2} b^\dagger b^\dagger b b && \text{Intrinsic nonlinearity} \\ &+ (\psi_n a a b^\dagger + \psi_n^* a^\dagger a^\dagger b) && \text{Mode coupling} \\ &+ h[e^{(-i\omega t)} a^\dagger + e^{(i\omega t)} a] && \text{External drive} \end{aligned} \tag{2.14}$$

Where $\hbar \equiv 1$, and $a, a^\dagger, b, b^\dagger$ are the magnon creation and annihilation operators for the quasi-uniform mode $|0\rangle$ with frequency ω_0, and for the higher-order spin wave mode $|n\rangle$ with frequency ω_n respectively. The first two terms describe the two spin wave modes $|0\rangle$ and $|n\rangle$, the terms proportional to Ψ_0 and Ψ_n describe the intrinsic nonlinear frequency shifts [49] of the modes $|0\rangle$ and $|n\rangle$, and ψ_n is the coupling parameter for the annihilation of two $|0\rangle$ magnons and creation of one $|n\rangle$ magnon, as well as the inverse process. The last term describes the excitation of the quasi-uniform mode by an external microwave drive with the amplitude h and frequency ω.

Furthermore, the equations of motion describing the coupled dissipative dynamics of the quasi-uniform (a) and higher-order (b) spin wave modes are:

$$i\frac{da}{dt} = \frac{\partial H}{\partial a^\dagger} + \frac{\partial Q}{\partial(da^\dagger/dt)} \tag{2.15}$$

$$i\frac{db}{dt} = \frac{\partial H}{\partial b^\dagger} + \frac{\partial Q}{\partial(db^\dagger/dt)} \tag{2.16}$$

Q is the dissipation function [50], given by

$$Q = \frac{da^\dagger}{dt}\frac{da}{dt}(\alpha_0 + \eta_0 a^\dagger a) + \frac{db^\dagger}{dt}\frac{db}{dt}(\alpha_n + \eta_n b^\dagger b) \tag{2.17}$$

where α and η are the intrinsic linear [50] and nonlinear damping parameters [51], respectively. It is shown that the equations 2.15 and 2.16 have a periodic solution $a = \bar{a}\exp(-i\omega t)$ and $b = \bar{b}\exp(-i2\omega t)$, where $\bar{a}$ and $\bar{b}$ are the complex spin wave mode amplitudes [20]. These equations can be solved numerically and the calculated $|\bar{a}|^2(\omega)$ function can be directly compared to the measured ST-FMR resonance lineshape.

To understand the mechanisms of nonlinear spin wave resonance quantitatively, we simplify equations and assume that the intrinsic nonlinearities Ψ_n and η_n of higher order mode $|n\rangle$ are negligible. This assumption allows us to reduce the equation of motion for the quasi-uniform mode amplitude $|\bar{a}|$ to the standard equation for a single-mode damped driven oscillator, where the resonance frequency is replaced by an effective resonance frequency [20]:

$$\omega_0^{eff} = \omega_0 + [\Psi_0 + \frac{2 \mid \psi_n \mid^2 (2\omega - \omega_n)}{(2\omega - \omega_n)^2 + (2\alpha_n\omega)^2}] \mid \bar{a} \mid^2 \tag{2.18}$$

From here, we see that there is a nonlinear shift in the frequency of the quasi-uniform mode, which arises from resonant three-magnon scattering. Further, we realize a constant damping parameter α_0 is replaced by an effective frequency-dependent nonlinear damping parameter [20]:

$$\alpha_0^{eff} = \alpha_0 + [\eta_0 + \frac{4 \mid \psi_n \mid^2 \alpha_n}{(2\omega - \omega_n)^2 + (2\alpha_n\omega)^2}] \mid \bar{a} \mid^2 \tag{2.19}$$

The last term shows that the nonlinear damping by three magnon scattering is enhanced resonantly near the resonant frequency $\omega_n/2$.

Chapter 3

Development of Experimental Methods

In this chapter, I address the experimental techniques we utilize in our laboratory to examine nanomagnets, specifically MTJs. Initially, I will describe the device packaging and sample preparation procedures used for coplanar waveguide-based measurements. Then, I will outline the experimental methods, setups, and configurations employed to assess and analyze the magnetic properties and magnetization dynamics in nanomagnets, along with the data obtained from each experiment.

3.1 Packaging of nanoscale magnetic tunnel junctions

To measure and study the magnetization dynamics in MTJs, we mount them on a coplanar waveguide (CPW) board. A CPW is widely used for microwave integrated circuit

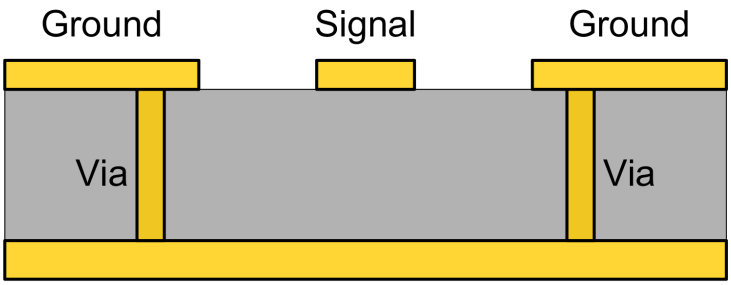

Figure 3.1: Coplanar waveguide consist of ground-signal-ground (GSG) planes. The bottom ground plane is separated from the top GSG layer by a dielectric substrate. Conducting bridges called vias connect the upper and lower ground planes.

design [52] at frequencies ranging from several hundred megahertz to tens of gigahertz. It consists of a conductor strip in the middle (the signal line), and two separate ground planes are located on either side of the center conductor. All these lie in the same plane on a dielectric substrate. There is also a bottom ground plate connected to the top ground planes through conducting bridges called vias. The impedance of CPW is 50Ω. Figure 3.2 depicts a sample wirebonded to the coplanar waveguide and ready for microwave spectroscopy measurements.

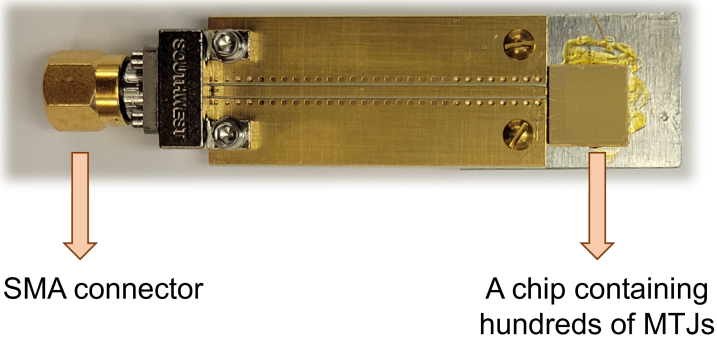

Figure 3.2: (a) A wavwguide and a chip containing MTJ devices. One MTJ is wire bonded to the CPW in order to be measured.

3.2 Magnetotransport measurement

We use magnetotransport measurement techniques to measure tunnel magnetoresistance hysteresis within multilayer MTJs. These measurements rely on the TMR effect described in the previous chapter. To measure magnetic hysteresis, we apply a DC electric current to the MTJ from a low-noise DC source. By sweeping the magnetic field along the easy-axis, we can controllably switch the magnetization direction of the free layer. The voltage across the ferromagnetic layers is detected using a nanovoltmeter. Figure 3.3 (a) demonstrates the hysteresis around the zero field and the minimum and maximum resistances in parallel and antiparallel states.

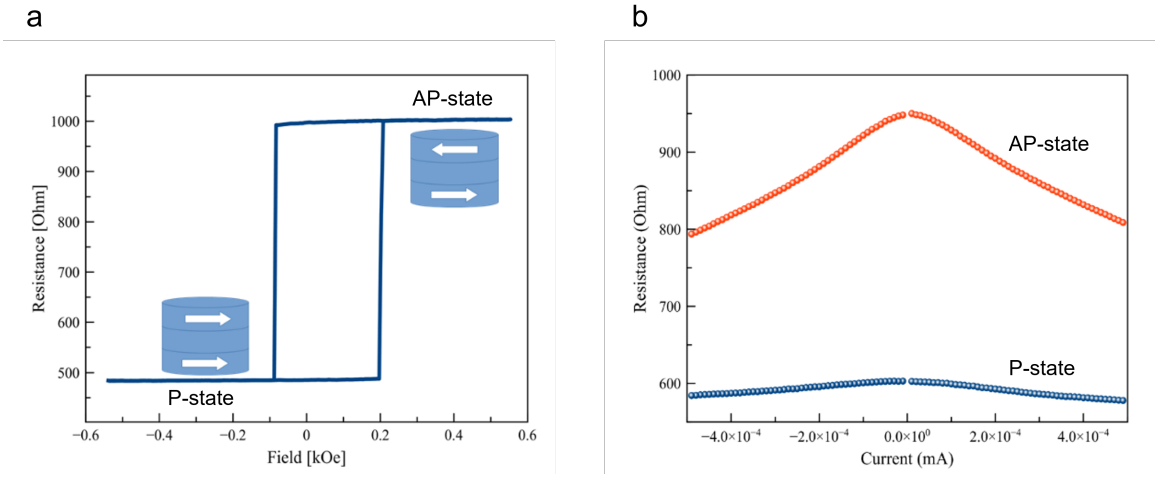

Figure 3.3: (a) Magnetic hysteresis of MTJ. Tunneling magnetoresistance (TMR) results in a higher resistance in the antiparallel state (AP) than the resistance of the MTJ in the parallel state (P). (b) Resistance of MTJ as a function of current in parallel and antiparallel states.

In addition, the resistance of the MTJ can be measured as a function of the applied DC current in both P and AP states. Due to thermal fluctuations and spin-torque effects, the resistance decreases when the current increases in both polarities, as depicted in figure

3.3 (b). At some critical current, spin torque switching will occur, causing a change in the device's resistance from p-state to AP state or vice versa. High currents can damage and destroy the device, so the figure only shows the measurements at low currents.

3.3 Microwave emission spectroscopy

Unpolarized electrons passing through the fixed layer become polarized. The polarized current transfers the spin angular momentum to the free layer and excites the free layer's magnetization. In fact, spin transfer torque is an important factor in controlling the magnetization state or driving a stable magnetization precession in the nanomagnet. It generates a continuous microwave signal by first exciting spin precession and then converting it to an electrical signal through microwave frequency resistance oscillations (magnetoresistance effect).

We have built a microwave emission spectroscopy station in our lab to detect emitted microwave signals due to precissional motion of magnetization in our nanomagnets. We utilize a spectrum analyzer, which is shown in figure 3.4 (b), to detect magnetization oscillations.

The emitted microwave signals are tiny (as low as a few femtowatts), and they need to be preamplified before being sent to the spectrum analyzer. This amplification happens in two steps: first by employing an ultra-low-noise microwave amplifier, such as that shown in figure 3.4 (c), and second, inside the spectrum analyzer. The filters and mixers on the spectrum analyzer are adjusted to pick up on a single frequency. The signal is modulated using field modulation and then routed to the lock-in amplifier. This technique allows us

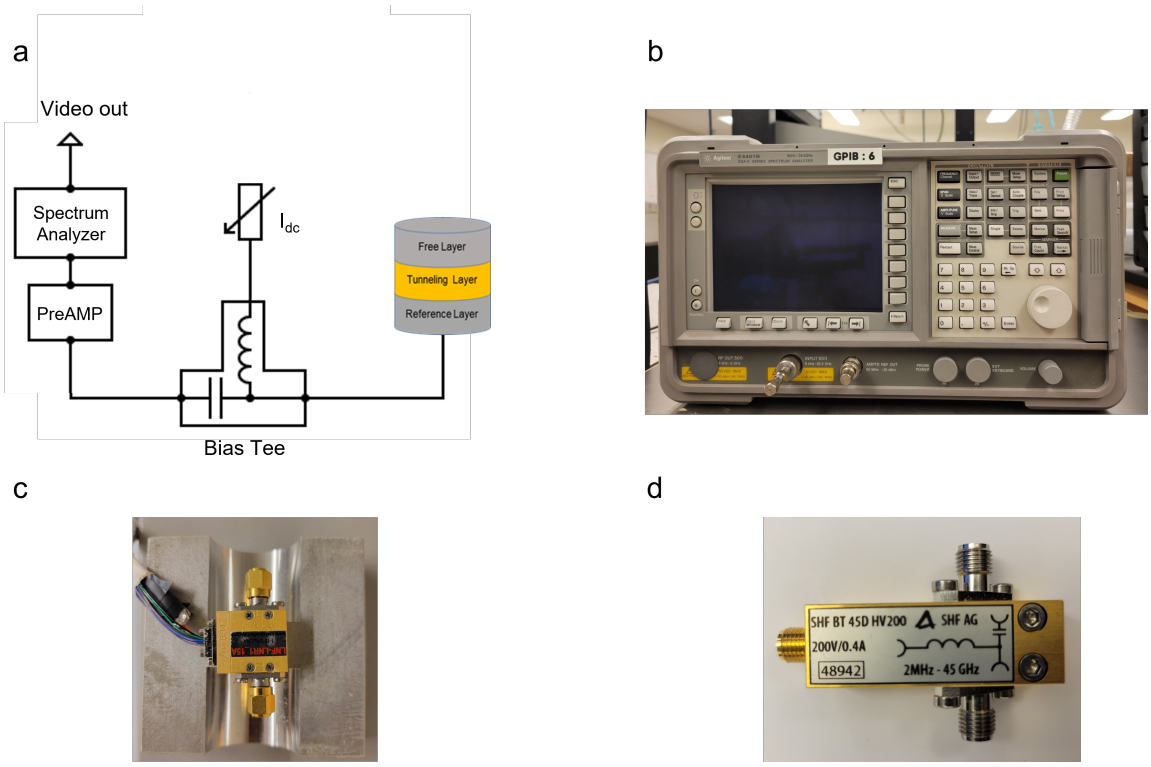

Figure 3.4: (a) Schematic of microwave emission spectroscopy (b) E4407B ESA-E Spectrum Analyzer, operating range: 9 kHz to 26.5 GHz. (c) Ultra-low-noise RF amplifier, model LNF-LNR1, operating range: 1–15 GHz. (d) The SHF BT 45D bias tee offers the ability to apply or detect DC current in a bias RF circuit operating in the range of 2 MHz to 45 GHz.

to detect spectral peaks at the frequency of spin torque oscillations under the conditions of a DC bias and the external magnetic field.

Now we know the scenario of magnetization dynamics induced by spin transfer torque from a DC current. These types of dynamics require the application of a large current exceeding the critical threshold to completely suppress the Gilbert damping of the nanomagnet so that instability occurs. When the applied DC current is below the threshold, the spin transfer torque is not strong enough to excite magnetization dynamics, and the nanomagnet will stay in the stationary state, taking only minor effects from the thermal

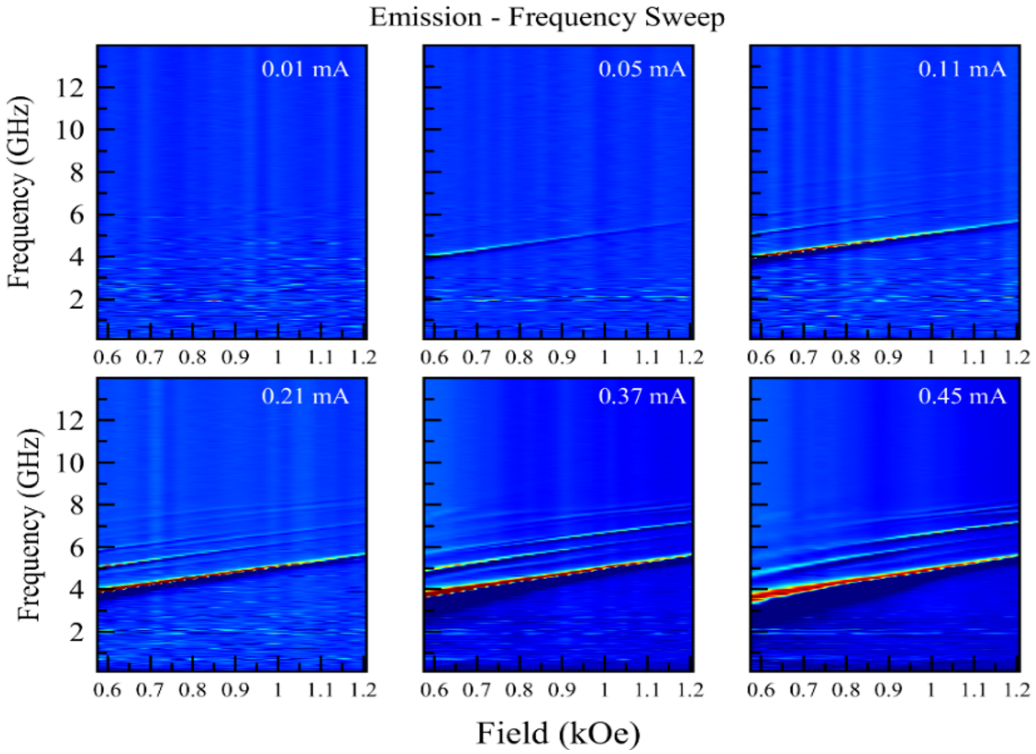

Figure 3.5: Spin wave modes are performed through field-modulated microwave emission spectroscopy, utilizing varying levels of current. This results in an increase in the amplitude of the modes due to the enhancement of the spin torque effect brought about by the increased current.

and spin transfer torques. Figure 3.5 represents magnon modes inside the free layer of the MTJ. Larger currents, and so greater spin torque effects, excite and reinforce the magnon modes. The color plots are comprised of single spectra that are typically measured in the field domain. We can compare the amplitude of the microwave signal peak as a function of current. Figure 3.6 shows the amplitude of the lowest mode as a function of current. It reveals that there is an onset of magnetic auto-oscillations at a critical current (0.25 mA), and at very high current, the nonlinear effects appear and decrease the amplitudes of the oscillations.

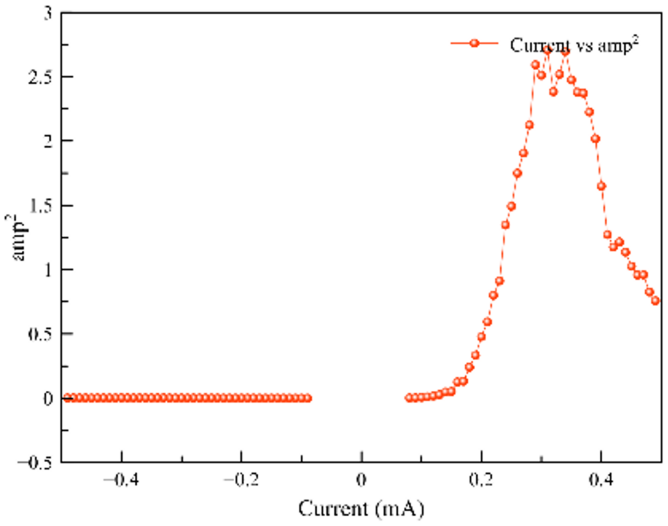

Figure 3.6: Amplitude of spin wave corresponds to the population of magnons. Greater current and so greater spin torque increases the population of magnons. A sudden onset of population of magnons occured at the critical current of 0.25 mA. Amplitude decreases again due to the nonlinearity of the system.

3.4 Spin-torque ferromagnetic resonance spectroscopy (ST-FMR)

In the microwave emission spectroscopy technique, it is necessary to apply a DC current that exceeds a critical threshold in order to fully suppress the Gilbert damping and excite magnetization dynamics. When the applied DC current falls below this threshold, the spin transfer torque is not sufficient to drive the nanomagnet out of its stationary thermally excited state, and its behavior is only minimally affected by the spin transfer torque. However, if a small oscillating current is applied, the alternating spin transfer torque and Oersted fields can drive the nanomagnet into a state of resonant precession when the frequency of the microwave current matches the intrinsic precession frequency of the nanomagnet [19, 53], which is dependent on the applied magnetic field.

Since this resonance typically occurs in the high radio-frequency range of 1-15 GHz, I will refer to this driving current as RF (radio-frequency) current as opposed to DC or AC current in the kHz range. This effect is linear in nature, at least at small RF current levels - precession will always occur, no matter how small the RF current is, and the amplitude of the precession will scale linearly with the RF current.

In ST-FMR, a microwave current (RF) can pass through the MTJ and its polarization direction will oscillate at the microwave frequency. This oscillation in polarization, together with Oersted fields, excite magnetization precession. The precessing magnetization of the MTJ, causes the resistance of the MTJ to oscillate [54]. These oscillations occur at the same frequency as the microwave current, which causes the current and the resistance oscillations to combine and create a rectified voltage [54]. This voltage is then detected at the lock-in.

The option of using a DC current source allows for the investigation of the effects of spin-torque while conducting the ST-FMR measurement. If a DC current is provided to the sample in ST-FMR, the resistance oscillation can create a non-zero time-average component, leading to a DC resistance variation that changes depending on the sweeping parameter, such as magnetic field. This signal is called photoresistance and it can also be detected at the lock-in. The amplitude of the resistance oscillation, changes in accordance with the variation in the cone angle of magnetization. The cone angle reaches its maximum value at the FMR resonance frequency, f_0, and diminishes to almost zero at other frequencies.

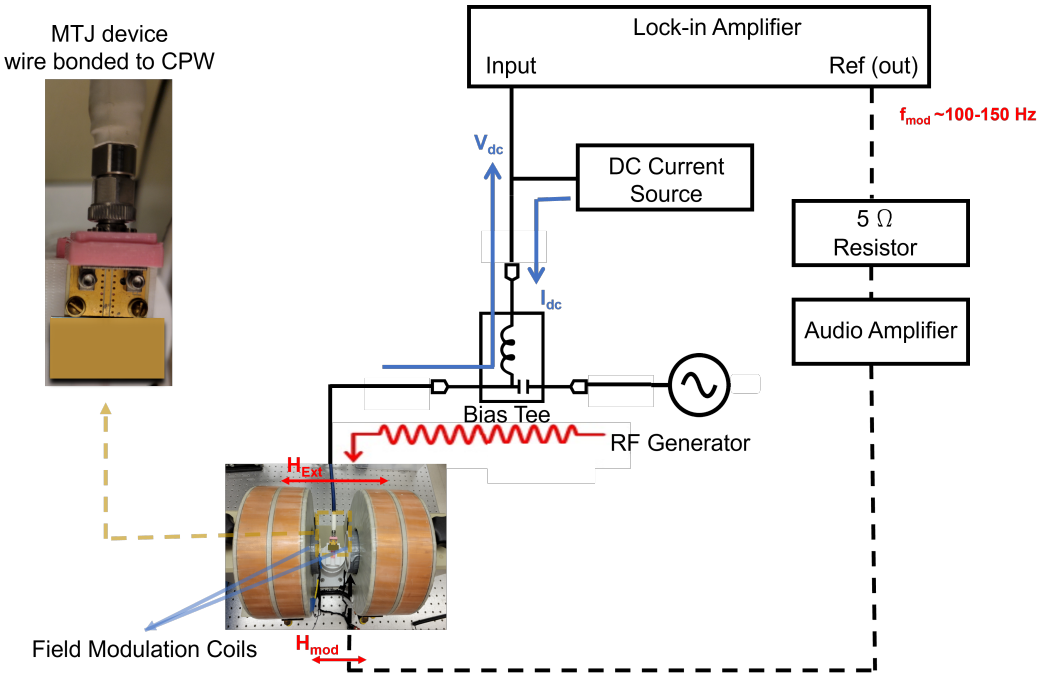

Figure 3.7: A schematic representation of the coplanar waveguide (CPW) based spin-torque ferromagnetic resonance (ST-FMR) setup is illustrated. A magnetic tunnel junction is positioned in proximity and wire-bonded to a CPW. The CPW board is designed to include a SMA connector, which is connected to the microwave generator and DC current source via the RF port of the bias-tee. The RF current, which is modulated at a frequency of $f_{mod} \sim 100 - 150$ Hz, is sent to the CPW, generating a driving microwave magnetic field, H_{RF}. The spin-polarized RF current excites magnetization dynamics through spin torque within the free layer and causes the resistance of the MTJ to oscillate at the resonance frequency through the tunneling magnetoresistance effect. The RF resistance of the MTJ is mixed with the microwave current to generate a DC rectified voltage, V_{mix}, which can be measured using a lock-in amplifier.

3.4.1 Experimental setup

The experimental apparatus for a CPW-based spin torque ferromagnetic ST-FMR measurement is depicted schematically in figure 3.7. The setup comprises a microwave generator, a bias-tee, a lock-in amplifier, and, optionally, a DC current source. The ST-FMR measurement is conducted by applying a quasi-static magnetic field to the sample. A continuous microwave signal, which is sent to the device transversely to the static field via

a CPW, is used to excite magnetization dynamics through spin torque within the free layer, thereby causing the resistance of the MTJ to oscillate at the resonance frequency through the tunneling magnetoresistance effect. The AC resistance of the MTJ is mixed with the AC microwave current to generate a DC rectified voltage, which can be measured using a lock-in amplifier. The option of using a DC current source allows for the investigation of the effects of spin-torque while conducting the ST-FMR measurement.

The ST-FMR signal is generally weak and is obscured by background noise. In order to discern the FMR signal, it must be modulated. A lock-in amplifier can be utilized to provide a modulation reference signal. In the subsequent sections, I shall expound on the various techniques that are implemented in our laboratory to modulate and detect the ST-FMR signal.

3.4.2 Pulse modulated measurements

In conventional ST-FMR measurements, the mixing of the current and resistance oscillations results in a direct voltage, V_{mix}, generated by the sample. The measurement of the ST-FMR spectrum, V_{mix}, yields a series of spectral peaks generated by spin waves that resonate within the MTJ. This method, known as rectification ST-FMR, is susceptible to frequency-dependent background signals due to non-linearities and impedance mismatches within the microwave circuit. To circumvent these obstacles, several techniques have been developed to provide high sensitivity information for any magnetic configuration of the MTJ. One such technique is pulse modulated ST-FMR, which can reduce background noise and facilitate the detection of small and weak FMR signals.

In pulse modulated ST-FMR measurements, a low-frequency square wave signal generator, such as the TTL output port of a lock-in amplifier, is connected to the pulse-trigger port of the microwave generator. This configuration enables the generation of microwave pulses at a few kHz. The lock-in amplifier receives the signal from the CPW, which contains information about the sample, and compares it to the signal from the microwave generator. This results in an on/off chopping of the microwave signal, which is collected by the lock-in amplifier at a higher sensitivity.

3.4.3 Field modulated measurements

Field modulated ST-FMR is another method to solve the problem of the parasitic backgrounds and obtain a reliable signal [55]. In this method, the external magnetic field is modulated by means of coils, which are composed of copper wire and located on the poles of the electromagnet. The lock-in amplifier generates a reference output voltage, V_{mod}, which is typically in the range of 0.4 - 1.2 V_{rms} and applies it to a sound amplifier, which converts the input AC voltage into an AC current, I_{mod}, typically in the range of 1 - 4 Amp. This AC current is then sent to the modulation coils, which produce an AC modulation field, H_{mod}, of a few Oersted which is collinear with the external field, H_{Ext}. The lock-in amplifier then measures the rectified voltage, V_{mix} [55], from the sample at the field modulation frequency, thus only detecting signals that depend on the magnetic field, and eliminating any non-magnetic background noise.

In the field modulated ST-FMR technique, care must be taken to ensure that the amplitude of the modulation field does not exceed the linewidth of the signal, as overmodulation may occur. This can result in an artificial increase in the linewidth of the signal or

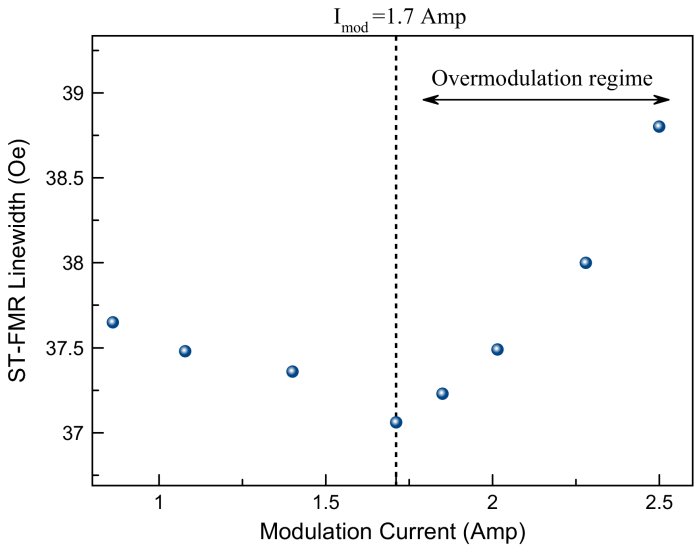

Figure 3.8: Overmodulation effect in ST-FMR linewidth from field-modulated ST-FMR measurements: for modulation currents I_{mod} greater than 1.7 Amp, the ST-FMR linewidth increases and the overmodulation effect becomes visible.

a decrease in its amplitude. In order to prevent overmodulation, a protocol is implemented in our laboratory to ensure that the amplitude of the modulation field remains within the appropriate range. The modulation field which is proportional to modulation voltage and so the modulation current, can be estimated as:

$$B_{mod} = (\frac{4}{5})^{3/2} \frac{\mu_0 N I_{mod}}{R} = c.I_{mod} \tag{3.1}$$

Where μ_0 is the permeability, R and N are the radius and the number of turns in each coil, and I is the modulation current through the coil. We can calibrate the modulation field by measuring and fitting the linewidth as a function of current (I_{mod}). The result represents the appropriate values for the modulation current.

As depicted in figure 3.8, the linewidth increases approximately as a parabola as a function of the modulation field/current. However, at very low modulation fields, the signal-to-noise ratio may increase, resulting in an artificially increased linewidth as well. Thus, we typically adjust the modulation field to be at the minimum linewidth of figure 3.8. However, previously we adjust the parameters of our spectrometer such that the overmodulation-caused linewidth increase of this minimum is not larger than typically 3-5%.

3.4.4 Evaluation of spectra

The ST-FMR experiment can be carried out while sweeping either the field or the frequency. In this work, I implement field-domain measurements as the result spectra is more simple to evaluate. In fact, in the field-sweep field-modulated ST-FMR technique, the lock-in amplifier measures the response of the magnetic system as output voltage ($\tilde{V}_{mix} = H_{mod}.\frac{dV_{mix}}{dH}$) as a function of H, which is a linear combination of symmetric and anti-symmetric Lorentzian function and it can be described by the following equation [56]:

$$\begin{aligned}\tilde{V}_{mix} = H_{mod}\frac{dV_{mix}}{dH} =& H_{mod}[\frac{2V_a}{[(1+4\frac{(H_{ext}-H_r)}{2\Delta H})^2(2\Delta H)]} \\ &- \frac{8V_s(H_{ext}-H_r)}{[[(1+4(\frac{H_{ext}-H_r}{2\Delta H})^2)]^2(2\Delta H)^2]} \\ &- \frac{16V_a(H_{ext}-H_r)^2}{[[(1+4(\frac{H_{ext}-H_r}{2\Delta H})^2)]^2(2\Delta H)^3]}]\end{aligned} \tag{3.2}$$

Where H_{mod} is the amplitude of the modulation field, V_a and V_s are the symmetric and anti-symmetric Lorentzian amplitudes, H_{ext} the external magnetic field, H_r the resonant field of a ferromagnetic sample, and ΔH is the half-width at half maximum (HWHM). It

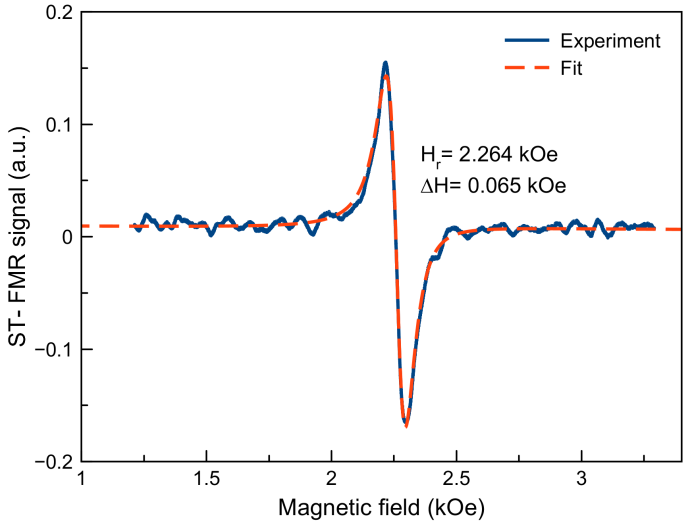

Figure 3.9: Example of field-modulated ST-FMR spectrum of MTJ measured at 4 GHz in the field domain.

must be regarded that both symmetric and anti-symmetric Lorentzians need to be fitted using the same resonance field and linewidth..

3.4.5 FMR linewidth and magnetic damping contribution

The FMR linewidth is associated with the magnetic damping in a material, which serves as an indicator of the energy loss that takes place within the magnetic system. The Gilbert damping mechanism is often the primary contributor to dissipation in magnetic systems. However, it is also possible for other nonlinear magnetic relaxation mechanisms to be present in the same system. In general, FMR linewidth correlated to Gilbert damping (α) can be described as:

$$\Delta H = \Delta H_0 + \alpha \frac{2\pi f}{\gamma} \tag{3.3}$$

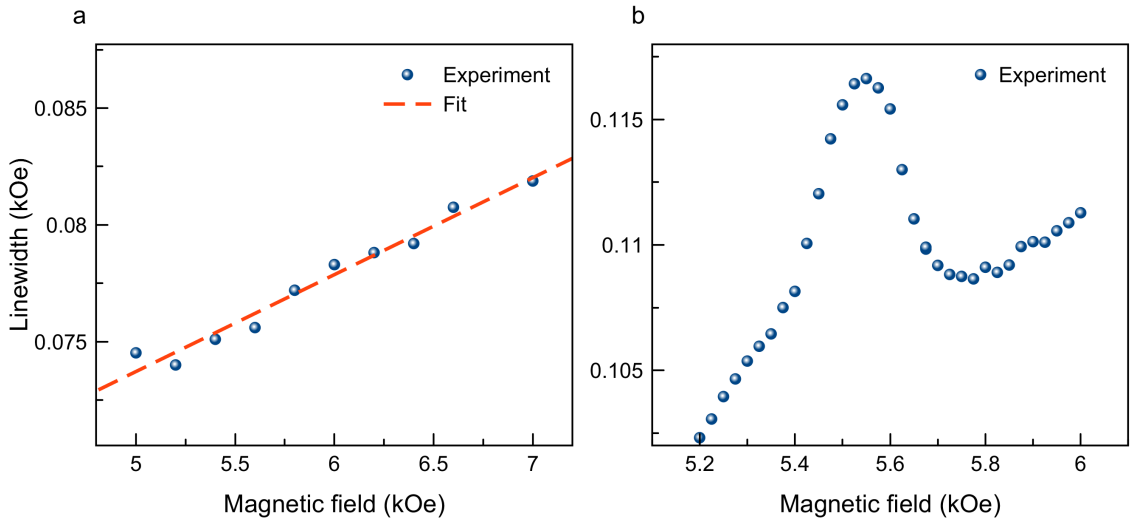

Figure 3.10: (a) A demonstration of field-modulated ST-FMR spectral linewidth in the linear regime for MTJ. (b) A noticeable enhancement of the line width is observed as a result of nonlinearities.

The first term in the equation represents the broadening of the line, which arises from the inhomogeneity within the sample. As the inhomogeneity of the sample approaches zero, the line broadening will also approach zero. This equation is applicable as long as nonlinear processes are not present, and the line width displays linear behavior. However, nonlinear phenomena can significantly impact and complicate the line width behavior. In the fourth chapter, a comprehensive theory is introduced to explain the FMR line width in the presence of nonlinearities.

3.5 Noise Spectroscopy

Internally generated electric noise can have a detrimental effect on the performance of devices utilizing magnon-based spintronics. Analysis of noise not only aids in identifying ways to eliminate disturbances, but also plays a crucial role in comprehending the electronic

and magnetic properties of magnetic systems. Furthermore, by understanding the origins of electric and magnetic noise within magnetic systems, it is possible to improve device design with a minimal noise level and increase the signal-to-noise ratio.

MTJ devices are promising candidates for high sensitivity and stability magnetic field sensing applications. Investigation of noise can lead to the development of MTJ sensors with a lower noise floor and improved detectivity. Different mechanisms can give rise to noise sources in MTJs, the most common being thermal (Johnson) noise, shot noise, 1/f noise, and random telegraph noise (RTN). Shot noise is a white noise that arises from the discrete nature of electric charge, while Johnson noise is generated by the motion of free electrons in a resistance due to temperature. Random telegraph noise is caused by sudden step-like transitions between two or more discrete voltages or current levels, and 1/f noise is a low-frequency noise for which the noise power spectral density is inversely proportional to the frequency of the signal.

In general, at low frequencies, noise sources can be categorized as frequency dependent or frequency independent. The frequency-independent component of the noise floor is typically generated by thermal noise and shot noise, while the low-frequency range is dominated by 1/f noise or, in some cases, random telegraph noise (RTN) [57]. Internal and external factors can influence the noise spectrum of a magnetic tunnel junction, such as the size of the junction, thickness of the free layer, defects, temperature, magnetic field, and bias voltage, among others. In the next two sections, I will explain the two different noise spectroscopy techniques - frequency domain and time domain - that are employed in our studies to investigate the noise performance of MTJs.

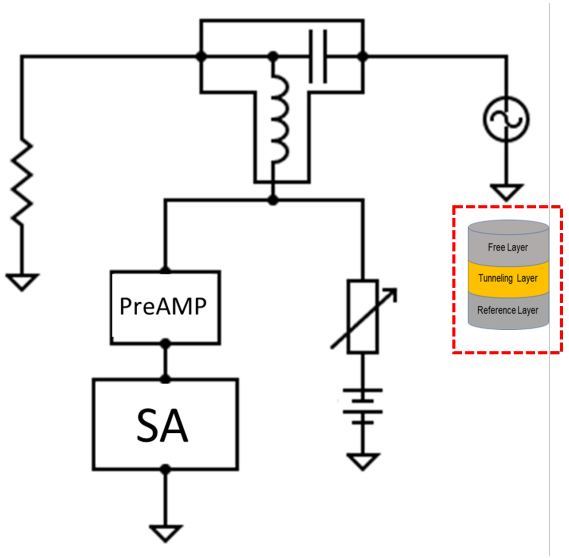

Figure 3.11: Schematic of noise spectroscopy measurement in frequency domain. In time domain measurements, the preamplifier and the spectrum analyze are replaced by an oscilloscope.

3.5.1 Frequency domain measurements

In order to conduct frequency-domain measurements, we utilize a low frequency spectrum analyzer to examine the noise level of MTJs. The schematic diagram for the noise measurement setup is depicted in figure 3.11 (b). The combination of static magnetic field, DC and RF signals induce electric current and spin waves, which subsequently results in the generation of electric noise. The sample is situated within a cryostat, as indicated by the red dotted line in the diagram. The voltage signals across the MTJ are amplified and subsequently fed into the spectrum analyzer. An example of noise spectra of an MTJ in the frequency domain, both in and out of resonance states, is presented in figure 3.12 (a).

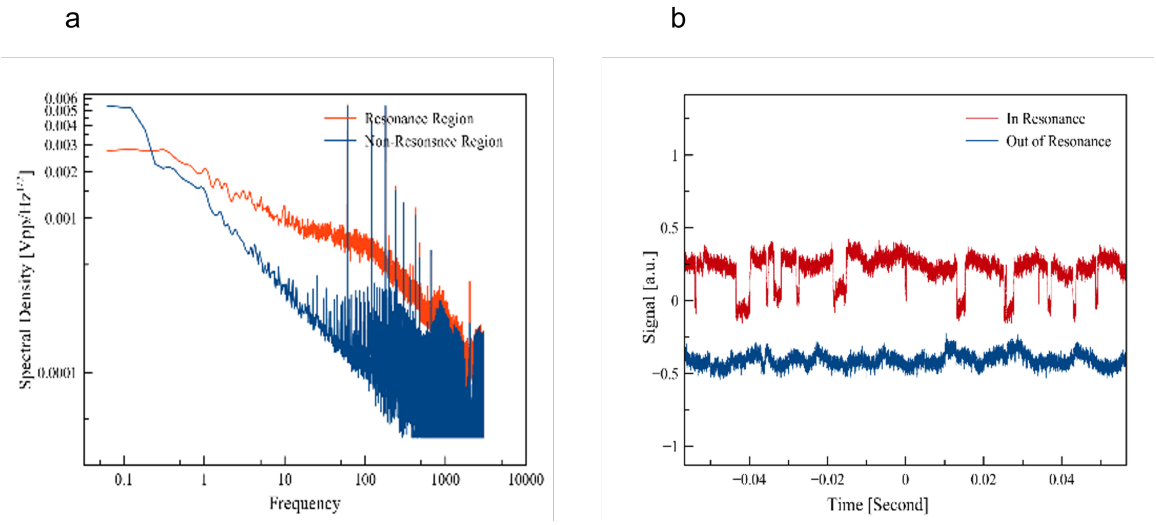

Figure 3.12: A representation of the noise spectra of a magnetic tunnel junction is provided for (a) frequency domain and (b) time domain measurements.

3.5.2 Time domain measurements

In order to assess the noise as a function of time, we have incorporated an oscilloscope into our experimental setup, as opposed to utilizing a spectrum analyzer. The oscilloscope plots the changing amplitude of the signal on the horizontal axis, which corresponds to time. The examination of electric noise in both the time and frequency domains offers a distinct understanding of the signal that may not be discernible through examination in only one domain. Figure 3.12 (b) provides an illustration of the noise spectra of a MTJ in the time domain, while in both the resonant and non-resonant states.

3.6 Cryogenic measurements

The temperature of a system plays a crucial role in determining its magnetic properties and can also affect the precision of measurements by causing thermal fluctuations.

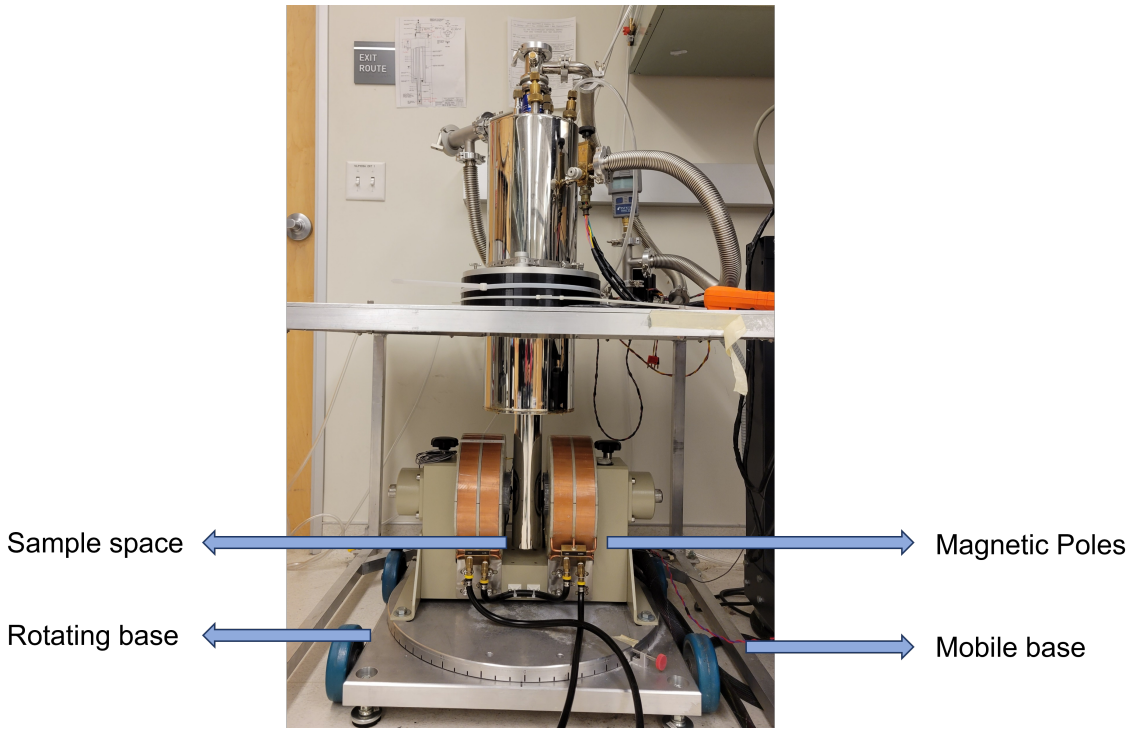

Figure 3.13: Cryostat model 8CN, the sample space is placed between the electromagnet poles. The rotating base provides the opportunity for angle-dependent measurements.

To mitigate these effects, low temperature measurements can be conducted using cryogenic techniques, which allow for temperatures as low as a few Kelvin.

In our laboratory, we utilize a helium flow cryostat, specifically the Model 8CN variable temperature cryostat from Cryo Industries of America, Inc., for measurements within a temperature range of 1.4 K to 30 K. This device is composed of three main sections: the sample compartment, where samples are held under low pressure conditions, a helium chamber, and a liquid nitrogen chamber for shielding. There is a capillary valve that allows us to control the flow of helium or nitrogen vapor between the He and sample spaces. Additionally, there are escape valves in place to release vapor into the laboratory environment.

A depiction of the cryostat on a mobile base within our lab can be seen in figure 3.13. The position of the sample space is adjusted to be between the magnetic poles. The cryostat also features a rotating base for conducting measurements at various angles. The system is connected to a vacuum pump and a nitrogen gas tank for the purposes of venting and pumping, which is regulated by a series of valves. A temperature sensor is positioned near the sample location.

In order to perform measurements, it is necessary to first stabilize the temperature by cooling the cryostat to its lowest temperature through adjustments to the capillary valve. The system can then be heated by flowing warmer helium vapor through the sample space, and a temperature sensor is used to monitor the temperature at all times.

Chapter 4

Interplay of Spin Torque and Nonlinearity

The theoretical content of this chapter is developed in collaboration with Boris Ivanov.

4.1 Introduction

The use of nanomagnets has been demonstrated to be a vital component in current technology, particularly in the field of spintronics. Ongoing research and development efforts are focused on utilizing nanomagnets for a variety of applications, including spin-torque memory, magnetic field sensors, microwave oscillators, detectors, and neuromorphic networks, among others. To fully understand and predict the behavior of nanomagnets, as well as to advance these technologies, it is essential to study the dynamics [58] and mechanisms of magnetization that lead to energy dissipation within magnetic systems. Within

this context, magnon-magnon processes are of paramount importance [7, 20], as they are responsible for the redistribution of energy between magnon modes [15] and constitute a major channel of dissipation in nanomagnets.

The term "Magnon scattering" refers to the process by which the energy and momentum of a magnon (a quanta of spin wave excitation) is transferred to another magnon.In nanoscale ferromagnets, the confinement imposed by their small size results in the formation of standing spin waves and the discretization of the spin wave spectrum. This discretization [46] generally weakens multi-magnon relaxation processes. As a result, the lifetime and amplitude of the main excitation mode are significantly enhanced. However, in the discrete spectrum of a nanomagnet, resonant processes are possible and lead to rather surprising magnetization dynamics.

In this study, we aim to investigate the relationship between nonlinearities and spin torque in nanoscale magnetic systems. In recent years, spin torque has been widely used as a reliable and controllable tool for manipulating magnetization [10, 11, 13, 14, 28] and has become a crucial component in modern spintronics. It is essential to understand the relationship between spin torque and nonlinearities and how they influence nanoscale magnetic systems. We demonstrate that the nonlinearities generated by magnon-magnon interactions substantially alter the behavior of the nanomagnet when exposed to spin torque [20]. We provide evidence of how these magnon processes can redefine and even reverse the response of nanomagnets to spin torque. We delve into the underlying mechanisms of this counterintuitive interaction between nonlinearity and spin torque, which has the potential to impact the operation of magnetic memory and oscillators.

4.2 Experimental procedure and Results

To investigate magnon interactions experimentally, we utilize out-of-plane magnetic tunnel junctions (MTJs) with elliptical layers of dimensions 100 nm x 150 nm in cross-section and 1 nm in thickness. Each MTJ consists of a ferromagnetic free layer (FL), a MgO tunneling barrier, and a synthetic antiferromagnet (SAF) positioned beneath the barrier, which is composed of two ferromagnets that are antiferromagnetically coupled through RKKY interaction via a Ru buffer layer. All ferromagnetic layers in the MTJs consist of CoFeB compounds. As the FL and SAF layers in the MTJs are magneto-dynamically decoupled, low energy magnon modes are localized in the FL. We use the FL as a zero-dimensional nanomagnet to study the magnon spectra that form at GHz frequencies and are discrete due to geometrical confinement.

We examine the FL excitations in various MTJs and observe the presence of non-linear damping resulting from multimagnon processes in all cases. The dominant resonant magnon processes under investigation include degenerate three-magnon (3M) scattering, degenerate four-magnon (4M) scattering, and non-degenerate three-magnon (3M) scattering. To clearly demonstrate these different forms of magnon-magnon processes, we have selected three MTJ devices and focus on the field region that clearly showcases the specific type of magnon process under examination.

To study the magnon spectra of the ferromagnetic free layer (FL) in each MTJ, we employ field-modulated ST-FMR technique. Figure 4.1 illustrates the magnon spectra for three different MTJ devices. In each case, we numerically label the magnon modes in

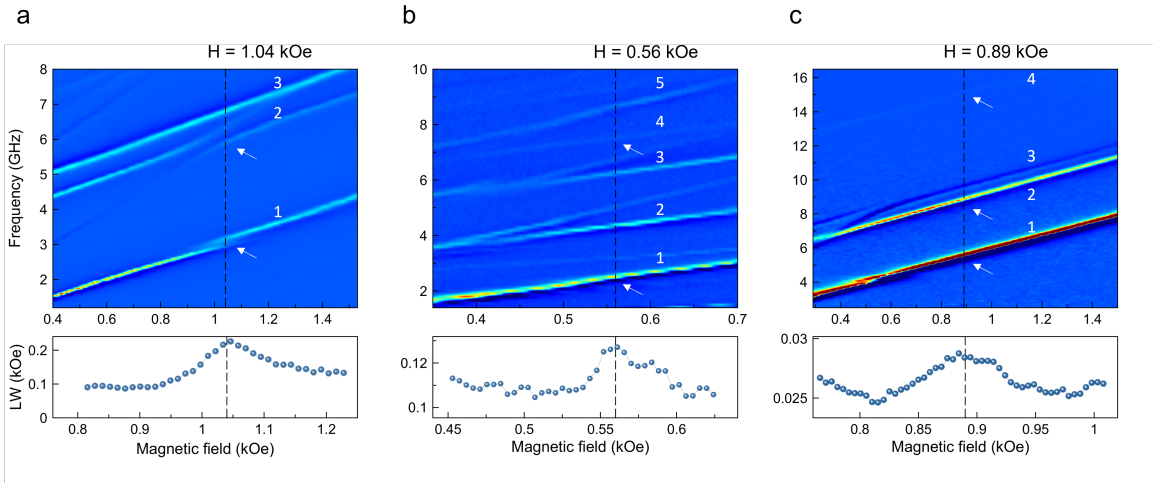

Figure 4.1: ST-FMR spectra of magnon modes in three MTJ devices are measured as a function of magnetic field. The mode damping is evaluated using the spectral linewidth of mode $|1\rangle$. An enhancement in linewidth is observed near the characteristic fields, which is attributed to (a) degenerate 3M scattering, (b) degenerate 4M scattering, and (c) non-degenerate 3M scattering, respectively.

ascending order. We use the linewidth of mode $|1\rangle$ to evaluate the mode damping for each device. The data is presented only for the field range that is relevant to the study.

Figure 4.1 (a) corresponds to the first MTJ and displays three spin-wave eigenmodes. The linewidth of mode $|1\rangle$ reveals that at a specific magnetic field value, $H = 1.04\ kOe$ ($f = 3.05\ GHz$), the linewidth and thus the mode's dissipation are increased. The broadening of mode $|1\rangle$ in the ST-FMR spectra measurement confirms this phenomenon. This field corresponds to the point where the second harmonic of mode $|1\rangle$ crosses mode $|2\rangle$ and an anti-crossing occurs. By comparing the frequencies of modes $|1\rangle$ and $|2\rangle$, we determine that the frequency ratio of the two modes is nearly $f_1 : f_2 = 1 : 2$, which indicates that at this particular field, energy conservation is satisfied and two magnons of the lower-frequency mode $|1\rangle$ can converge into one magnon of the higher mode $|2\rangle$. This constitutes a degenerate 3M process.

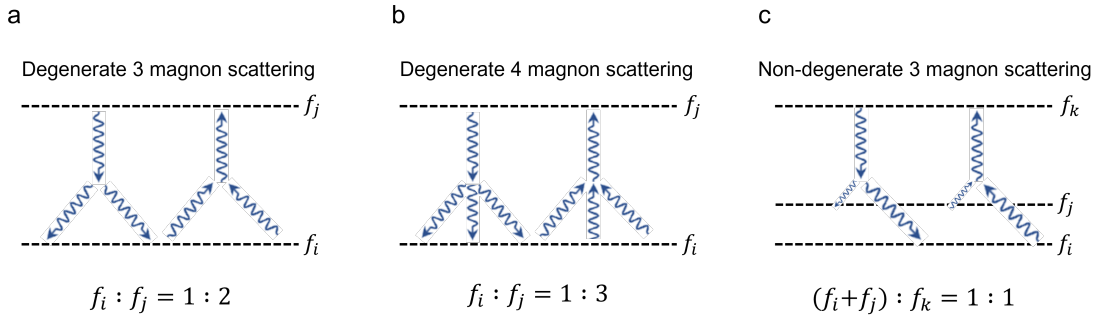

Figure 4.2: Schematic of different types of magnon-magnon interactions

Next, we investigate the ST-FMR spectra and linewidth of mode $|1\rangle$ for the second MTJ, as depicted in figure 4.1 (b). The linewidth exhibits a peak at the characteristic field, $H = 0.56\ kOe$ ($f = 2.52\ GHz$). At this field, the third harmonic of mode $|1\rangle$ intersects with mode $|4\rangle$. The frequency ratio of $f_1 : f_4 = 1 : 3$ allows for three magnons of mode $|1\rangle$ to convert into one magnon of mode $|4\rangle$, resulting in the occurrence of the 4M process due to conservation of energy. The linewidth increases as a result of resonant degenerate four-magnon scattering at this field.

Finally, as illustrated in figure 4.1 (c), the spin wave eigenmodes for the last MTJ device were measured. The results shows the presence of five linear modes. The linewidth of mode $|1\rangle$ displays a peak at a characteristic field of $H = 0.89\ kOe$ ($f = 5.52\ GHz$), where a frequency ratio of $f_1 + f_2 : f_4 = 1 : 1$ is observed. This ratio, in accordance with the principle of energy conservation, suggests that it is possible for one magnon in mode $|1\rangle$ and one in mode $|2\rangle$ to transform into a higher-order magnon in mode $|4\rangle$. As a result, the linewidth increases due to resonant non-degenerate three-magnon scattering.

As nonlinear phenomena, magnon scattering processes become more pronounced at higher levels of excitation. These excitations can be increased through two methods:

the application of an antidamping spin torque or the enhancement of the microwave drive applied to the magnetic tunnel junction.

We try the first approach to enhance nonlinear response: we subject each device to a DC bias current, which resulted in a nominal antidamping spin-torque. The results of this approach are presented in figure 4.3 for the cases of (a) degenerate 3M scattering, (b) degenerate 4M scattering, and (c) non-degenerate 3M scattering. However, the antidamping spin-torque, which is typically expected to result in a reduction in linewidth [59], instead, led to a broadening of the resonance for mode $|1\rangle$ at the characteristic fields for each MTJ and an increase in dissipation near the multi-magnon regimes [20]. As the antidamping spin-torque was increased, the peaks arising from magnon-magnon processes became more prominent, making this counterintuitive effect more discernible.

We also attempt to use the other approach: we increase nonlinearities by enhancing the power of the microwaves. The results, as shown in figures 4.3 (d), (e), and (f) for degenerate 3M and 4M and also non-degenerate 3M magnon scattering, respectively, are consistent with the results obtained from the first approach.

Upon examination of the magnitude of linewidth increase for various magnon processes, it is clear that degenerate three-magnon scattering is a far greater effect than degenerate four-magnon and non-degenerate three-magnon scattering. These latter processes, while weaker, are discernible in sufficiently nonlinear systems. They can exert a non-negligible impact on magnetic damping and, therefore, the energy efficiency of spin-torque applications.

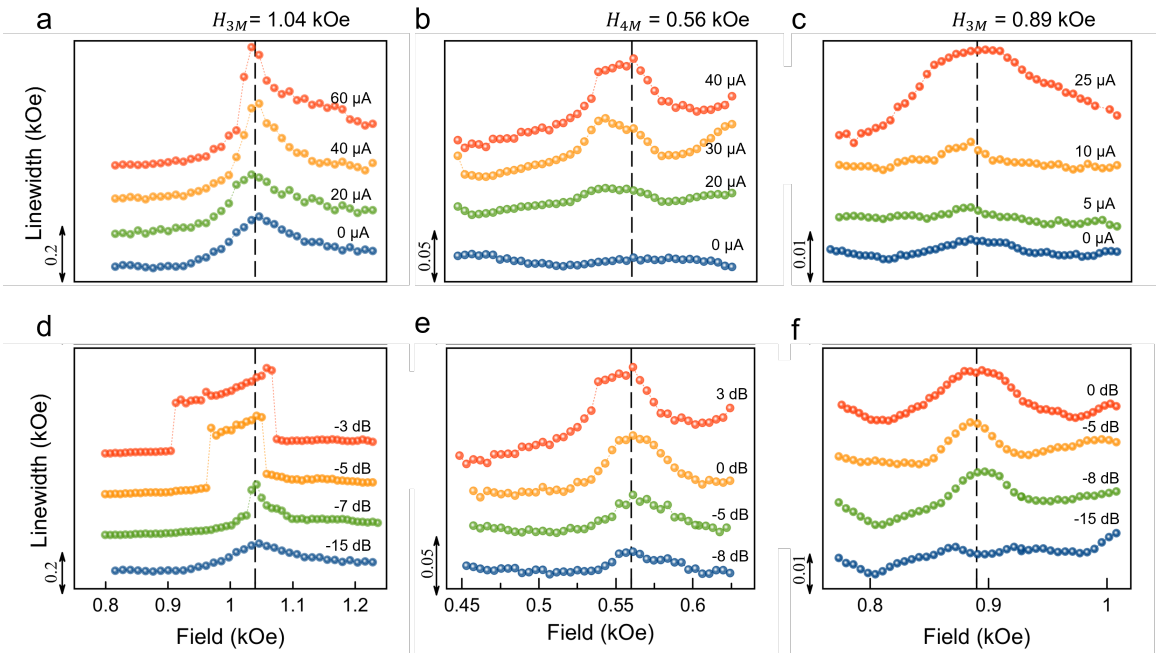

Figure 4.3: The linewidth of mode $|1\rangle$ is measured as a function of the magnetic field for different values of the applied DC current (anti-damping spin torque) and microwave power. As the DC current and microwave power are increased, it is observed that the linewidth of mode $|1\rangle$ broaden, indicating an increase in dissipation within the system. This effect is particularly pronounced in the regimes of (a, d) degenerate 3M scattering, (b, e) degenerate 4M scattering, and (c, f) non-degenerate 3M scattering, where the peaks resulting from magnon-magnon processes become more prominent. This unexpected outcome highlights the complexity and nonlinearity of these processes and the necessity for further research to fully comprehend their underlying mechanisms.

4.3 Theory

In bulk ferromagnets, spin waves possessing a continuum spectrum can interact nonlinearly with one another through the fulfillment of energy and momentum conservation principles [41]. In contrast, geometric confinement in nanoscale ferromagnets leads to discretization of spin waves, resulting in a lack of frequency degeneracy between the primary excitation mode and higher spin-wave modes. This discretization also results in reduced magnetic damping and weakening of multi-magnon relaxation processes [60, 61].

As a consequence, the lifetime and amplitude of the primary excitation mode are significantly increased, thereby intensifying all nonlinear processes involving this mode. In the present study, we conduct experimental investigations to determine the dominant nonlinear contributors within nanomagnets:

1. Degenerate three-magnon (3M) scattering
2. Degenerate four-magnon (4M) scattering
3. Non-degenerate three-magnon (3M) scattering

In this study, we investigate nonlinear processes at high excitation levels, achieved through the application of either antidamping spin-torque or high microwave power, in which the modes actively participate at a higher rate. Our experimental data indicates the presence of a nonlinear frequency shift. Furthermore, we observe an inverted response of the nanomagnet to spin torque. We attribute this counterintuitive phenomenon to a nonlinear multimagnon confluence process in which multiple magnons of lower modes merge into a single magnon of a higher mode. In collaboration with Prof. Boris Ivanov, we have developed a theoretical framework to explain nonlinear spin wave resonance and nonlinear damping in nanomagnets.

4.3.1 Degenerate three-magnon scattering: $a + a \longrightarrow b$

When the ratio of frequencies between two modes is approximately $f_i : f_j = 1 : 2$, two magnons of the lower-frequency mode $|i\rangle$ can merge into one magnon of the higher mode $|j\rangle$. This process constitutes a degenerate three-magnon (3M) interaction.

The nonlinear three-magnon scattering has been previously studied in our laboratory [20], where it has been experimentally and theoretically established that the magnetic damping of spin wave modes in nanoscale ferromagnets possesses a strong nonlinear component of resonant character. It has been demonstrated that nonlinearity exerts a significant impact on the response of the nanomagnet to spin torque, with antidamping spin torque enhancing damping in the scattering regime. In section 2.8, a concise description of degenerate 3M scattering and its significant nonlinear damping effect is provided. Additional information can be obtained from [20, 48].

4.3.2 Degenerate four-magnon scattering: $a + a + a \longrightarrow b$

When the ratio of frequencies between two modes is approximately $f_i : f_j = 1 : 3$, it is possible for three magnons of the lower frequency mode $|i\rangle$ to merge into one magnon of the higher frequency mode $|j\rangle$. This process is known as "degenerate four-magnon scattering." In our study, we experimentally investigate the role of degenerate 4M process in the nonlinearity of spin waves in nanomagnets. To explain this giant nonlinear damping effect, we begin by utilizing a Hamiltonian that effectively includes the nonlinear scattering between the two modes $|0\rangle$ and $|n\rangle$ with operators a and b respectively:

$$\begin{aligned} H &= \omega_0 a^\dagger a + \omega_n b^\dagger b && \text{Two spin-wave modes} \\ &+ \frac{1}{2}\Psi_0 a^\dagger a^\dagger a a + \frac{1}{2}\Psi_n b^\dagger b^\dagger b b + \Psi a^\dagger a b^\dagger b && \text{Intrinsic nonlinearity} \\ &+ (\psi^* b^\dagger a a a + \psi b a^\dagger a^\dagger a^\dagger) && \text{Mode coupling} \\ &+ h(e^{-i\omega t} a^\dagger + e^{i\omega t} a) && \text{External drive} \end{aligned} \tag{4.1}$$

Where $\hbar \equiv 1$. As outlined in the equation provided, the first two terms depict the descriptions of two spin-wave modes. The terms that are proportional to Ψ_0, Ψ_n and Ψ represent the intrinsic nonlinear shifts of the modes. The term that is proportional to the coupling parameter (ψ) represents the process in which three $|0\rangle$ magnons are annihilated and one $|n\rangle$ magnon is created, as well as the inverse process. The last two terms pertain to the excitation of the mode $|0\rangle$ by an external drive.

We further take into account the dissipation function Q, Eqn. (2.17) defined in section 2.8, and solve the Hamiltonian equations of motion, Eqn. (2.15) and Eqn. (2.16). Considering the periodic solution $a = \bar{a}\exp(-i\omega t)$ and $b = \bar{b}\exp(-i3\omega t)$, where $\bar{a}$ and $\bar{b}$ are the complex spin wave mode amplitudes, Eqn (2.13) and (2.14) can be simplified to two nonlinear algebraic equations for absolute values of the spin wave mode amplitudes $|\bar{a}|$ and $|\bar{b}|$ which can be solved numerically. As the ST-FMR signal is directly related to $|\bar{a}|$, we can compare the calculated $|\bar{a}|(\omega)$ to the observed ST-FMR resonance lineshape.

To better understand the unexpected increase of nonlinear damping by antidamping spin-torque and resonance peak splitting of spin wave in 4M scattering regime qualitatively, we simplify the problem and assume the intrinsic nonlinearities for mode $|n\rangle$ are negligible ($\Psi_n = 0$ and $\eta_n = 0$). By doing so, the equation of motion for the mode amplitude $|\bar{a}|$ is reduced to a standard equation for a single-mode damped driven oscillator, where a constant damping parameter α_0 is replaced by an effective frequency-dependent nonlinear damping parameter α_0^{eff}:

$$\alpha_0^{eff} = \alpha_0 + \eta_0 \mid \bar{a} \mid^2 + \frac{9\alpha_n \mid \psi \mid^2}{(3\omega - \omega_n)^2 + (3\alpha_n\omega)^2} \mid \bar{a} \mid^4 \tag{4.2}$$

and the resonance frequency of mode $|0\rangle$ is replaced by an an effective resonance frequency ω_0^{eff}:

$$\omega_0^{eff} = \omega_0 + \Psi_0 \mid \bar{a} \mid^2 + \frac{3 \mid \psi \mid^2 (3\omega - \omega_n)}{(3\omega - \omega_n)^2 + (3\alpha_n\omega)^2} \mid \bar{a} \mid^4 \tag{4.3}$$

Equation 4.2 shows that the damping parameter of mode $|0\rangle$ becomes a resonant function of the drive frequency ω with a maximum at one third of higher order mode $|n\rangle$, $(\omega = \frac{1}{3}\omega_n)$. This effective damping is also inversely proportional to damping parameter α_n of the higher-order mode $|n\rangle$. When α_n is sufficiently small, the damping of the quasi-uniform mode is significantly increased at $\omega = \frac{1}{3}\omega_n$, which causes the amplitude of the mode $|0\rangle$ to diminish at drive frequency.

Equation 4.3 shows mode $|0\rangle$ has a nonlinear frequency shift which presents a resonant behavior with respect to drive frequency. This equation is antisymmetric as a function of $(3\omega - \omega_n)$ meaning that when $\omega < \frac{1}{3}\omega_n$, nonlinear shift is negative causing a fold-over toward lower frequencies, and when $\omega > \frac{1}{3}\omega_n$, nonlinear shift is positive causing a fold-over toward higher frequencies. The bidirectional fold-over effect causes the amplitude of resonance to exhibit a local minimum at $\omega - \frac{1}{3}\omega_n$, which resembles a peak splitting. This effect is proportional to the mode amplitude $|\bar{a}|$ and becomes visible when the amplitude is large enough. In contrast to the degenerate 3M process, peak splitting is a very weak effect in the 4M process and is only visible at very high excitations. Unfortunately, in our experiment, we were unable to reach this point as high AC/DC currents often caused dielectric breakdown of the MgO barrier.

4.3.3 Non-degenerate three-magnon process: $a_1 + a_2 \longrightarrow b$

We also investigate resonant non-degenerate three-magnon scattering. When the frequency ratio of two modes is nearly $f_i + f_j : f_k = 1 : 1$, two different magnon modes $|i\rangle$ and $|j\rangle$ with lower but different frequencies, combine to create a higher-order magnon mode, $|k\rangle$. The Hamiltonian describing three magnon modes interacting with each other can be written as:

$$\begin{aligned} H = {} & \omega_1 a_1^\dagger a_1 + \omega_2 a_2^\dagger a_2 + \omega_n b^\dagger b && \text{Three spin-wave modes} \\ & + (\psi a_1 a_2 b^\dagger + \psi^* a_1^\dagger a_2^\dagger b) && \text{Mode coupling} \\ & + h_1(a_1^\dagger e^{-i\omega t} + a_1 e^{i\omega t}) && \text{External drive of mode } |i\rangle \\ & + h_2(a_2^\dagger e^{-i\omega_2 t} + a_2 e^{+i\omega_2 t}) && \text{External drive of mode } |j\rangle \end{aligned} \tag{4.4}$$

where $\hbar \equiv 1$, a_1, a_2, and b are the magnon operators for the modes $|1\rangle$, $|2\rangle$ and $|n\rangle$ respectively. Unlike degenerate 3M and 4M processes, we relinquish the terms for the intrinsic nonlinearities in the equation and assume they are negligible. The terms proportional to ψ represent the mode coupling. The term proportional to h_1 describes the excitation of lowest-order mode $|i\rangle$ by an external ac drive with the amplitude h_1 and frequency ω, and the last term describes the excitation of mode $|j\rangle$ by a random force with the amplitude h_2 in such $\langle a_2\rangle_\tau = \langle a_2^\dagger\rangle = 0$, and $\langle a_2^\dagger a_2\rangle = n(\omega_2) \sim \frac{1}{e^{\frac{\omega_2}{\tau}} - 1}$.

We solve the equations of motion (2.15 and 2.16) for a_1 and b. Like degenerate 3M- and 4M processes, we consider a periodic solution for these equations, $a_1 = \bar{a}_1 exp(-i\omega t)$, $a_2 = \bar{a}_2 \exp(-i\omega_2 t + i\phi)$, and $b = \bar{b} \exp(-i(\omega + \omega_2)t + i\phi)$, where ϕ is a random phase in such $\langle e^{i\phi}\rangle = 0$. We also need to note that $\langle b\rangle = 0$. By doing so and repeating the steps to

reduce the equations of motion to the standard equation for a single-mode damped driven oscillator, we can calculate the nonlinear frequency of mode $|1\rangle$:

$$\omega_0^{eff} = \omega_1 + \frac{|\psi|^2.(\omega + \omega_2 - \omega_n)}{(\omega + \omega_2 - \omega_n)^2 + \alpha_n^2\omega_n^2}|\bar{a}_2|^2 \tag{4.5}$$

and the effective damping parameter:

$$\alpha_1^{eff} = \alpha_1 + \frac{\alpha_n|\psi|^2(\omega + \omega_2)}{(\omega + \omega_2 - \omega_n)^2 + \alpha_n^2\omega_n^2}|\bar{a}_2|^2 \tag{4.6}$$

Equation 4.5 clearly shows the nonlinear frequency shift attains an antisymmetric resonance term when $\omega+\omega_2 = \omega_n$, arises from the non-degenerate 3M scattering. The damping parameter acquire a term describing the resonant enhancement of nonlinear damping by non-degenerate 3M scattering near the resonance frequency $\omega_n - \omega_2$.

4.4 Conclusion

In conclusion, we have conducted a thorough investigation of the dissipation processes within nanomagnets. We have examined the nonlinearities that arise from resonant magnon processes and have found that these nonlinearities have a significant impact on the response of nanomagnets at high levels of excitation, such as when subjected to antidamping spin torque or high ac current. This response is vastly different from the characteristics of linear and nonlinear spin wave resonances. We have discovered that magnon-magnon processes can reverse the response to spin torque and increase the spectral linewidth and effective damping of the magnon mode when the mode undergoes multimagnon scatter-

ing upon spin torue. We have developed a theory that explains the nonlinear broadening of the spectral linewidth of magnon modes in nanomagnets and specifically addresses the Lorentzian contribution of these nonlinearities to dissipation.

Figure 4.4 illustrates the various magnon-magnon interactions that occur within the frequency range of a magnetic tunnel junction. The linewidth of the lowest magnon mode demonstrates a complex behavior, resulting in multiple Lorentzian contributions to dissipation. Through extensive measurements on a large number of devices, we have been able to identify and understand the correlation between these peaks and the various magnon processes. Our findings indicate that the most prevalent nonlinearity observed is degenerate three-magnon scattering, followed by degenerate four-magnon scattering and non-degenerate three-magnon scattering. Although higher-order processes also exist within the system, their significance diminishes and they are overshadowed by the more dominant processes. This research provides a more comprehensive understanding of the performance of spin-torque applications, and can aid in the development of advanced memory and oscillator technologies.

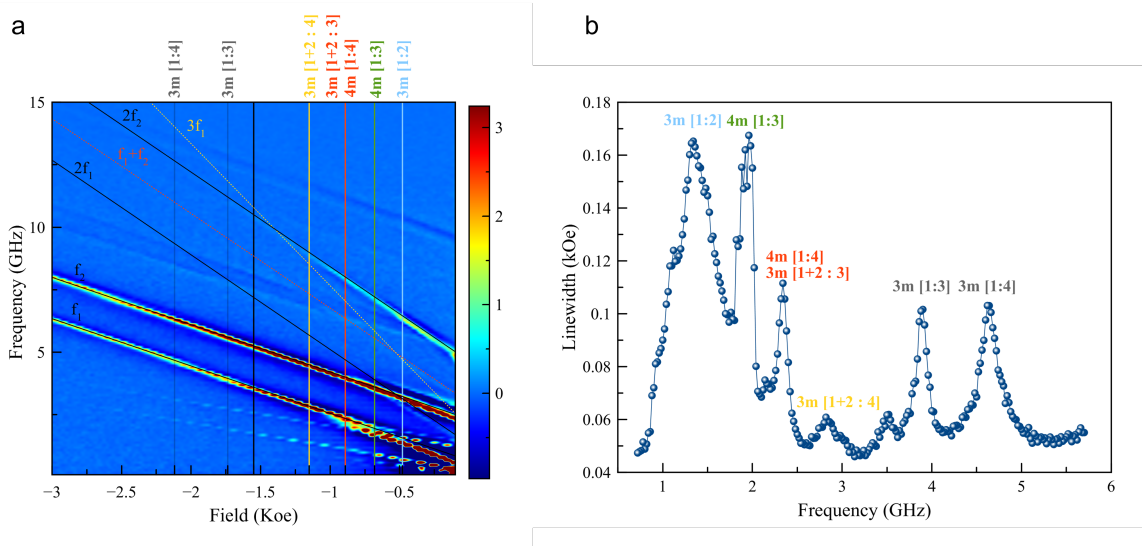

Figure 4.4: (a) The various types of magnon processes which are correlated to nonlinear effects in the linewidth of the lowest mode. (b) The linewidth of this mode represents multiple Lorentzian contributions to dissipation.

Chapter 5

Controlling Magnon Interaction by a Nanoscale Switch

The content of this chapter are adapted from my work originally published as ACS Appl. Mater. Interfaces 2021, 13, 17, 20288–20295. The theory is developed in collaboration with Roman Verba, Vasyl Tyberkevych, and Boris Ivanov.

5.1 Introduction

Many spintronic technologies are based on the idea of manipulating the magnetization of a nanoscale magnet by spin torque. Spin torque drives magnetic reversal in nonvolatile spin-torque memory [10, 11, 12, 13, 14] and auto-oscillations in spin-torque oscillators while competing with magnetic dissipation [15, 16, 17, 18]. Magnon scattering processes play a major role in this context. They lead to redistribution [62, 63] of energy among magnon modes and determine magnetization dynamics at large excitation levels

[49, 64, 65] which are of particular importance for spintronics applications [51, 66, 67]. In nanomagnets – the building blocks of the latter – the discrete magnon spectrum leads to unusual phenomena that are qualitatively different from those in bulk and thin films [68, 69, 70]. In particular, three-magnon scattering has been recently shown [20] to invert the response of a nanomagnet to spin-torque, thus impinging on the main working principle of many spintronics technologies.

Magnon scattering is also responsible for parametric pumping [71], soliton formation, phase locking, and other instrumental phenomena of magnetization dynamics [51, 66, 72]. Controlling magnon scattering processes [73] would allow for tuning the nonlinear response of nanomagnets employed in neuromorphic magnetic systems [2, 3, 4]. Moreover, it would provide a path for engineering coherent magnon coupling [74, 75, 76] in hybrid quantum information applications [77]. Functionalization of nanomagnets critically depends on our ability to control magnon interaction at the nanoscale, which has remained difficult to achieve [78, 79].

In this work, we demonstrate that magnon scattering in a nanomagnet can be efficiently controlled by an adjacent synthetic antiferromagnet that acts as a nanoscale switch. By triggering spin-flop transition in the synthetic antiferromagnet and by utilizing its nonuniform stray field, we achieve to toggle the degenerate three-magnon scattering in the nanomagnet.

In nanoscale ferromagnets, standing spin waves form due to geometrical confinement, the magnon spectrum at GHz frequencies is discrete. In this study, we consider a thin ferromagnetic nanodisk with elliptical cross-section as a model nanomagnet. Its spin

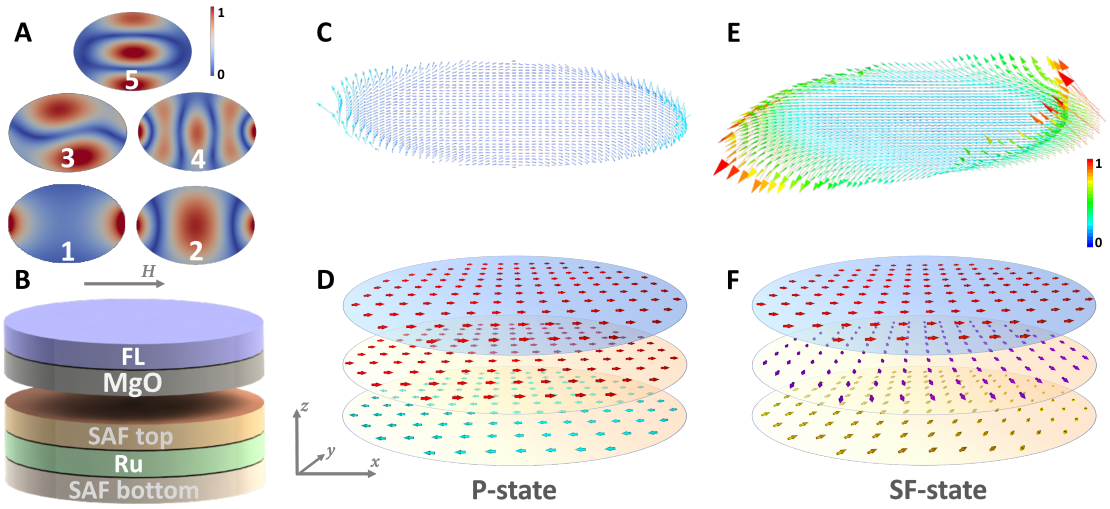

Figure 5.1: Micromagnetic simulation of the normalized magnetoresistance of the MTJ device. The hysteretic spin-flop at positive fields is qualitatively reproduced.

wave modes correspond to the normal modes [80] of a disk (figure 5.1A). We number the modes in ascending order of their frequency, starting with $|n = 1\rangle$ for the lowest frequency f_1 mode which has excitation maxima at the tips of the ellipse. With increasing mode number n, one and more excitation nodes appear within the disk plane. The frequency of the modes depends on magnetic field. When the frequency ratio of two modes is nearly $f_i : f_j = 1 : 2$, two magnons of the lower-frequency mode $|i\rangle$ can confluence into one magnon of the higher mode $|j\rangle$. This constitutes a degenerate three-magnon (3M) process which, due to its technological relevance [20, 67, 78], we shall focus on in what follows.

Besides the energy conservation requirement given by the frequency ratio, the 3M scattering is determined by the strength of interaction between the magnon modes involved in the process [20, 78, 81]. In nanomagnets possessing the symmetry of an orthogonal coordinate system (e.g., rectangular, circular, elliptical) [82] and with negligible magnetic

anisotropy, the number of 3M processes allowed by symmetry is greatly reduced, as recently shown in Refs. [78, 81, 83]. However, irregularities of demagnetization field at the nanomagnet's edges, as well as inevitable structural imperfections [10, 84], can diminish the symmetry restrictions and lead to a finite, albeit small, 3M magnon interaction. Application of a local nonuniform magnetic field to the nanomagnet has a similar symmetry-breaking effect, but it can result in a drastic increase of the magnon interaction, be done in a controlled manner and used as a tool to engineer magnon scattering. The applied field must exhibit nonuniformity at the length scales of the nanomagnet and therefore, itself, originate from a nanoscale source.

5.2 Experimental procedure and results

5.2.1 Synthetic antiferromagnet as a nonuniform magnetic field at nanoscle

To validate the proposed concept, we employ a magnetic tunnel junction nanopillar of elliptical layers with 150 nm×100 nm cross-section and ∼1–2 nm thickness, sketched in figure 5.1B and detailed in the Methods section. The device consists of a ferromagnetic free layer (FL), an MgO tunneling layer, and a synthetic antiferromagnet (SAF). The latter is composed of two ferromagnetic layers coupled by antiferromagnetic RKKY interaction [85, 86] through a Ru buffer layer. The bottom layer is exchange-biased along the major axis of the ellipse by an antiferromagnet. All ferromagnetic layers consist of CoFeB compounds, endued with easy-plane magnetic anisotropy [56]. Due to the shape anisotropy, the major axis of the ellipse is the magnetic easy-axis.

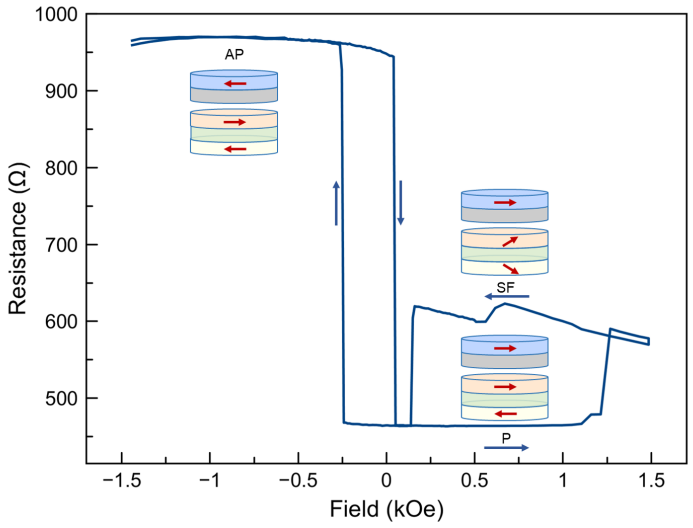

Figure 5.2: MTJ nanodevice resistance, as a function of field applied in the easy-axis, shows switching events between antiparallel (AP), parallel (P), and spin-flop (SF) state.

With magnetic field applied in the easy-axis, we measure the resistance of the device, which is governed by the tunneling magnetoresistance across the MgO layer [17, 55, 87]. As shown in figure 5.2, the resistance presents with a nearly rectangular hysteresis loop near zero field. At negative fields, the device is in the high-resistance, antiparallel (AP) state. By increasing the field to 0.04 kOe, the free layer switches by 180° and the device arrives in the low-resistance, parallel (P) state (figure 5.1D). With further increasing the field to 1.21 kOe, the SAF undergoes spin-flop transition [88] (figure 5.1F) and the device enters into the intermediate-resistance, spin-flop (SF) state. After reversing the direction of the field sweep, the device lingers in the SF-state until 0.16 kOe. Then the SAF layers align opposite to each other; this corresponds to the P-state of the device (figure 5.1D). By further sweeping the field backwards, the free-layer undergoes reversal of the zero-field loop, and the device arrives in the AP-state.

In the P-state (figure 5.1D), the stray field from the SAF at the position of the free layer (figure 5.1C) is small – the fields from the top and bottom layer of the SAF in MTJs are engineered to largely cancel each other [10, 12, 89]. Upon the spin-flop transition, however, the SAF's stray field increases and presents with a pronounced nonuniformity at nanoscale (compare figure 5.1C,E). We utilize the hysteretic behavior of the SAF to controllably switch this field. While we use external magnetic field to drive the spin-flop transition in this work, various nanoscale switches driven by other external stimuli such as spin current, electric field, strain, and temperature are generally possible.

5.2.2 Measuring magnon modes in P- and SF-states

To investigate the magnon spectra, we use field-modulated spin-torque ferromagnetic resonance (ST-FMR) [55]. The measurements are first carried out by sweeping the field from negative to positive values; the data is shown in figure 5.3A. Several excitations with nearly linear frequency-field relation are observed. Since the FL and SAF layers possess very different effective magnetic anisotropy energies (i.a. due to RKKY interaction and exchange bias – see Methods), their magnon modes are well separated in energy. As detailed in Refs. [55, 88], the modes shown in figure 5.3 correspond to standing spin wave modes which are localized in the free layer and have normal-mode [80] excitation profiles (figure 5.1A). At the positive field of 1.21 kOe, the device switches into the spin-flop state. The stray field from the SAF slightly affects the frequencies and the separation of the magnon modes. This effect suggests a small yet noticeable modification of the FL micromagnetic state and/or its magnon modes.

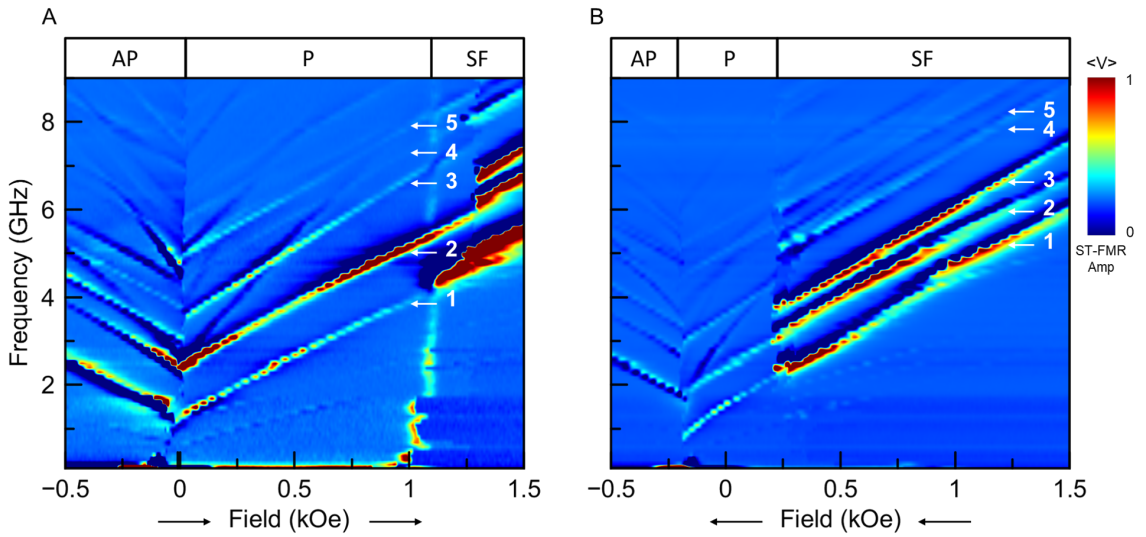

Figure 5.3: Spin-torque ferromagnetic resonance measurements carried of by sweeping the field from negative to positive values (A) and from positive to negative values (B). The magnon modes present with the same frequency-field slope (faint lines with doubled slope correspond to parasitic second-harmonic signals). The field regions of the parallel (P), antiparallel (AP), and spin-flop (SF) states are indicated; magnon modes are numbered. All measurements are carried out at room temperature.

We repeat the ST-FMR measurements – now sweeping the field from positive to negative values. The magnon spectrum shown in figure 5.3B is similar to the forward-sweep in figure 5.3A. However, the switching from spin-flop state to parallel state takes place at $\sim 0.2\,\mathrm{kOe}$. The SF-state occupies a larger field range. In what follows, we investigate magnon processes within the hysteretic field region of 0.2–1.2 kOe, where the device can be controllably brought in two distinct regimes of the P-state and SF-state.

The linewidth of a magnon mode represents its dissipation rate. We evaluate the linewidth of the main mode $|1\rangle$, shown in figure 5.4. In the spin-flop state, the linewidth presents with a peak at the characteristic field 0.35 kOe (2.65 GHz), for which we find the frequency ratio $f_1 : f_4 = 1 : 2$ for the modes $|1\rangle$ and $|4\rangle$. Here, two magnons of the mode

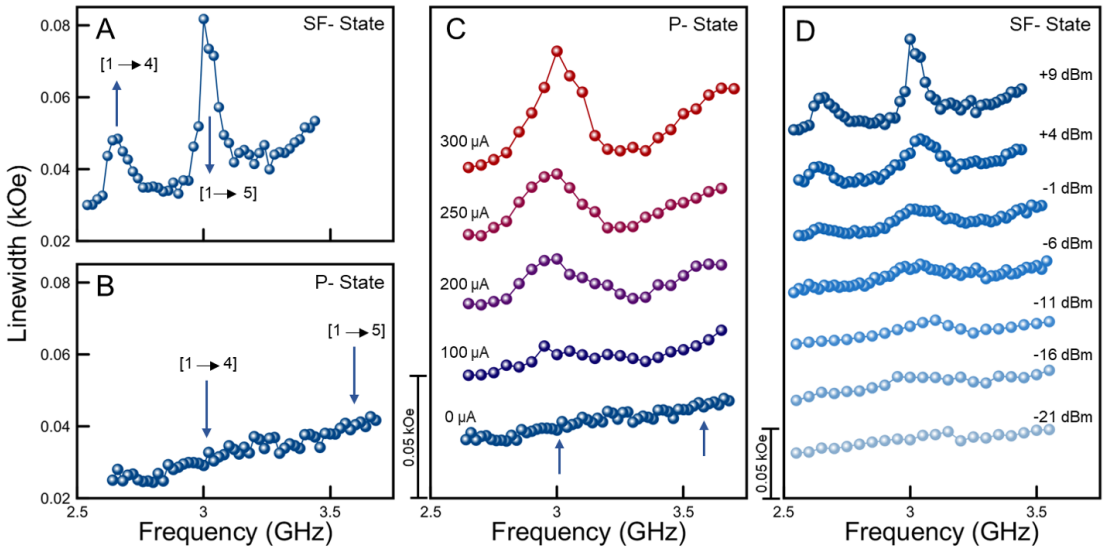

Figure 5.4: (A) In the spin-flop state, the linewidth of mode $|1\rangle$ exhibits two peaks due to the three-magnon processes. The labels $[i \to j]$ indicate positions for which the frequency ratio of the participating modes $f_i : f_j = 1 : 2$ is found. (B) In the parallel state, the three-magnon scattering rates are negligibly small; no peaks in the linewidth are observed. (C) However, with increasing dc bias current and the associated antidamping spin-torque, the three-magnon scattering rates in the parallel state are enhanced. (D) In the spin-flop state, at zero dc bias, the linewidth peaks fade away with decreasing microwave power.

$|1\rangle$ confluence into one magnon of the mode $|4\rangle$, constituting a degenerate three-magnon process that we label as $[1 \to 4]$. At another characteristic field of 0.5 kOe (3 GHz), a peak that corresponds to the $[1 \to 5]$ process is observed. These peaks represent an increased dissipation rate due to the 3M process that is resonant in the frequency detuning $2f_i - f_j$ of the participating modes, as derived in Ref. [20]. The frequency detuning becomes zero and the dissipation peaks at the characteristic 3M fields.

Now, we evaluate the linewidth in the parallel state, as shown in figure 5.4B. The frequency ratios $f_1 : f_4 = 1 : 2$ and $f_1 : f_5 = 1 : 2$ are maintained at slightly shifted fields 0.6 kOe (3 GHz) and 0.8 kOe (3.6 GHz) and allow for the same $[1 \to 4]$ and $[1 \to 5]$ processes.

However, the linewidth does not exhibit peaks at the characteristic fields. Since the 3M process is a nonlinear phenomenon that becomes more prominent as larger excitations, we increase the microwave power. However, even at high excitation levels leading to device destruction, the 3M peaks of the linewidth cannot be realized.

To make sure that the $[1 \rightarrow 4]$ and $[1 \rightarrow 5]$ processes are present in the P-state but just small in magnitude (scattering rate), we subject the device to dc bias current that results in a nominal antidamping spin-torque. The anti-damping spin-torque leads to linewidth reduction (115 MHz/mA) at field values far away from the characteristic three-magnon fields, where the 3M process is virtually inactive. In the 3M regime near the characteristic fields, on the other hand, the effect of the antidamping spin torques is inverted. With increasing antidamping spin torque, the effective susceptibility of both modes, $|i\rangle$ and $|j\rangle$, increases. As detailed in Ref. [20], the modes begin to participate in the 3M process at a higher rate. While the intrinsic dissipation continues to be reduced by the antidamping spin torque, the nonlinear effect of the 3M process dominates and increases the total dissipation. As shown in figure 5.4C, at the characteristic 3M fields, we in fact find that the effective dissipation increases in response to the anti-damping spin-torque and presents with two peaks. This inversion of the spin-torque effect is inherent to the resonant 3M process [20] and confirms that they are indeed present in both parallel and spin-flop state. In the P-state, however, the 3M scattering rate is negligibly small (unless enhanced by spin-torque).

5.3 Theory

The obtained result validates the proposed concept of controlling magnon interaction via symmetry-breaking local magnetic field. To assess magnon interaction, normalized vector field of the static magnetization $\vec{\mu}(\vec{r})$ and dynamic magnetization of individual magnon modes $\vec{s}(\vec{r})$ must be considered. The magnetic Hamiltonian term, that describes the confluence of two $|i\rangle$ magnons into one $|j\rangle$ magnon (as well as the inverse process), is $H^{(3)} = \psi_{ij} a_i a_i a_j^* + \psi_{ij}^* a_i^* a_i^* a_j$, with a being the mode amplitude [20]. Using the vector Hamiltonian approach [58, 81], the magnon interaction coefficient ψ_{ij} can be written as

$$\psi_{ij} \sim \int 2\left(\vec{s}_i \cdot \vec{s}_j^*\right) \vec{\mu} \cdot \hat{N} \cdot \vec{s}_i + \left(\vec{s}_i \cdot \vec{s}_i\right) \vec{\mu} \cdot \hat{N} \cdot \vec{s}_j^* \, \mathrm{d}^3 r \tag{5.1}$$

The interaction is largely related to dipolar coupling between the magnons, and the operator $\hat{N}$ can be written in the integral form

$$\hat{N} = \int \hat{G}(\vec{r}, \vec{r}') \, \mathrm{d}^3 r' \tag{5.2}$$

with the magnetostatic Green's function kernel having components $\hat{G}_{\alpha\beta'}(\vec{r}, \vec{r}') = -\frac{1}{4\pi} \partial_\alpha \partial_{\beta'} |\vec{r} - \vec{r}'|^{-1}$. The diagonal components of the integral kernel are symmetric in space, while off-diagonal ones are antisymmetric. With the FL magnetized along the x-axis, only N_{xy} contributes to the 3M scattering. As a consequence of the spatial antisymmetry of this component, 3M confluence from mode $|1\rangle$ into laterally totally antisymmetric modes should have a sizeable scattering rate, while confluence into symmetric modes is prohibited

[78, 81, 83]. Since the modes $|4\rangle$ and $|5\rangle$ are almost but not perfectly symmetric, their small scattering rate in the parallel state is consistent with the theoretical picture.

In general, application of the SAF's stray field in the SF-state has a manifold effect on the 3M scattering. First, the static magnetization can tilt away from the easy-axis (high-symmetry) direction, which allows the diagonal components (N_{xx} and N_{yy}) to contribute to the magnon interaction and to lift the symmetry restrictions for the magnon modes. This effect can be further amplified by the reduced symmetry of the static magnetization vector field. In particular, while maintaining the central symmetry $\vec{\mu}(\vec{r}) = \vec{\mu}(-\vec{r})$, it can lose axial symmetry, e.g. $\vec{\mu}(x, y) = \vec{\mu}(-x, y)$. Second, the SAF's stray field with nonuniformity at nanoscale can directly break magnon modes' symmetry and blend their symmetric or antisymmetric character [90, 91].

Our micromagnetic simulations [92] show a very small change to the FL static magnetization vector field upon application of the SAF's stray field. The tilt of the magnetization is negligible, the variation of the vector field at the edges of the FL disk is small ($\langle 1 - \mu_x \rangle_{\mathrm{P}} = 13 \cdot 10^{-4}$ and $\langle 1 - \mu_x \rangle_{\mathrm{SF}} = 18 \cdot 10^{-4}$ in figure 5.1F). Modification of the mode separation in figure 5.3, however, indicates that this small change of the micromagnetic state and the presence of the nonuniform stray field from the SAF are sufficient to affect the mode structure. The micromagnetic simulations on the rather complex multilayer structure of the MTJ device do not allow for a reliable quantitative consideration of the mode structure for the calculation of mode interaction ψ. Yet, we can assess the resulting effect experimentally.

Generally, the 3M scattering rate depends [20] on the product $g \cdot \psi$ of magnon excitation level g and interaction ψ between the magnon modes that participate in the 3M process. We carry out microwave power dependent measurements at zero dc bias current. With decreasing power p in the spin-flop state (figure 5.4D), the linewidth peak fades away. It takes over 30 dB of power reduction for the linewidth peak to subside and for the 3M scattering rate to reach the value of the parallel state. We estimate an enhancement of the $g \cdot \psi$ product between parallel and spin-flop state of $(g_{\mathrm{SF}} \cdot \psi_{\mathrm{SF}}) : (g_{\mathrm{P}} \cdot \psi_{\mathrm{P}}) > 35$.

The spin waves in the MTJ nanodevice are excited by microwave Oersted fields and high-frequency spin-torques [93, 94]. The excitation level g is thus not just a function of the microwave power, $g \propto \sqrt{p}$, but also increases with the effective angle ϕ between magnetic moments of the free layer and the SAF top layer [95]. To account for that, we assess the amplitude of the ST-FMR signal in the parallel and spin-flop state. The measurements are carried out as a function of the microwave power at field values outside of the three-magnon regime and result in the ratio of ST-FMR amplitudes in the spin-flop and parallel state of $A_{\mathrm{SF}} : A_{\mathrm{P}} \approx 35$.

The amplitude of the ST-FMR signal is generally a function of the magnon excitation level g and the sensitivity of the voltage signal to magnetization oscillations. The latter is composed of photovoltage and photoresistance. In the calibration measurements, no dc current is used, thus there is no contribution from the photoresistance. The photovoltage is a function of the angle ϕ between the free layer and the top SAF layer. The ST-FMR amplitude can be therefore written as $A \propto g \cdot \sin \phi$.

For the spin-flop state, the angle can be extracted from the magnetoresistance measurements (Fig. 2) as $\phi_{\mathrm{SF}} = 64°$. In the parallel state, the angle ϕ_{P} can strictly speaking not be treated as zero. The angle assumes a small but finite effective value due to non-uniformity of the magnetization and small misalignment of the magnetic field with respect to the easy-axis. Based on micromagnetic simulations and the precision of the sample alignment, we find this angle to be below one degree. However, based on our estimations across multiple samples, for the following calculation, we use the most generous upper limit of $\phi_{\mathrm{P}} < 4°$. By means of this calibration, we find the excitation level in the spin-flop state to be only slightly larger than in the parallel state:

$$\frac{g_{\mathrm{SF}}}{g_{\mathrm{P}}} = \frac{A_{\mathrm{SF}}}{A_{\mathrm{P}}} \cdot \frac{\sin \phi_{\mathrm{P}}}{\sin \phi_{\mathrm{SF}}} < 2.7 \tag{5.3}$$

This conservative estimation reveals the ratio of the mode interaction in the spin-flop and parallel state to be at least $\psi_{\mathrm{SF}} : \psi_{\mathrm{P}} > 13$. Such large difference in magnon coupling leads to the qualitatively different behavior observed in figure 5.4A,B. Even at moderately large excitation levels, the modified magnon coupling results in a 200% increase of the effective damping, marking distinct dissipation states of the SF an P states (figure 5.4A,B,D).

5.4 Conclusion

In conclusion, we achieve a controlled toggling of the magnon interaction by at least one order of magnitude. By means of a magnetic field that is nonuniform at the nanoscale, the symmetry restrictions for magnon scattering processes are diminished and the scattering rate is modified. While further theoretical and experimental studies are

called upon to elucidate the quantitative connection between the magnon scattering, the micromagnetic state of the nanomagnet, and the symmetry of the stray field, this work demonstrates engineering of magnon interaction in a magnet of nanoscale size. We generate the local field by exploiting hysteretic spin-flop transition of a synthetic antiferromagnet. Other nanodevices based on spin-torque, thermal, and voltage-driven switching are envisioned. The distinct dissipative states, that result from modified magnon interaction, add functionality to spin-torque applications such as spin-torque memory [10, 11, 12, 13, 14], spin-torque oscillators [15, 16, 17, 18], microwave detectors [67], and spin wave based logic [6]. In the emerging paradigm of magnetic neuromorphic networks [2, 3, 4], nonlinear response of magnetic neurons plays a central role. Magnon scattering processes [78] offer a route to achieving such nonliniearity, which can be tuned by controlled magnon interaction as developed in this work. Furthermore, magnon processes have the potential to provide nonlinear capabilities to spin-based hybrid quantum systems, for which efficient control of magnon interaction is a prerequisite and allows for engineering coherent magnon coupling.

5.5 Methodes

MTJ devices and micromagnetic simulations. The devices were fabricated on thermally oxidized Si wafers. Using magnetron sputtering, the following layer stack was deposited: (15)PtMn antiferromagnetic layer, (2.3)$Co_{70}Fe_{30}$ SAF bottom layer, (0.85)Ru RKKY-layer, (2.4)$Co_{40}Fe_{40}B_{20}$ SAF top layer, (1)MgO tunneling layer, (1.8)$Co_{20}Fe_{60}B_{20}$ free layer. The numbers in parenthesis indicate the thickness of the layers in nanometers. The layer stack was seeded and capped by (5)Ta layers and electric leads. The devices were

defined using electron-beam lithography and etched using ion milling to an elliptical pillars (with lateral dimensions of 150 nm×100 nm for the device shown here). The devices were subject to thermal annealing at 300°C for 2 h in magnetic field applied along the major axis of the ellipse. The annealing procedure defined the exchange bias field of the SAF bottom layer to point along the $-x$ direction.

Micromagnetic simulations were carried out using MuMax code [92]. The magnetization of the layers was set to values obtained from magnetometry carried out on film-level control samples: FL – 1630 emu/cm^3, SAF top – 1400 emu/cm^3, SAF bottom – 1900 emu/cm^3. The volume exchange interaction was set to 13 pJ/m, the RKKY exchange interaction between the SAF top and SAF bottom layers was set to -5 fJ/m. The SAF bottom layer is exchange-biased by the PtMn antiferromagnet, which was modelled via a unidirectional anisotropy field of -0.045 T along x-axis, and by a uniaxial anisotropy of 60×10^3 J/m^3.

Because of the different magnetization values, as well as additional contributions of RKKY interaction and exchange bias to the effective magnetic anisotropy, the magnetic anisotropy energies of the FL and the SAF layers are very different. The magnon modes of the free layer and the SAF layers are thus well separated in energy. The observed effects were confirmed not to originate from magnon-magnon interaction of the free layer and the SAF layers. The three-magnon model was validated experimentally on multiple MTJ devices with positive and negative perpendicular anisotropies and various magnetic configurations of the SAF [20, 55].

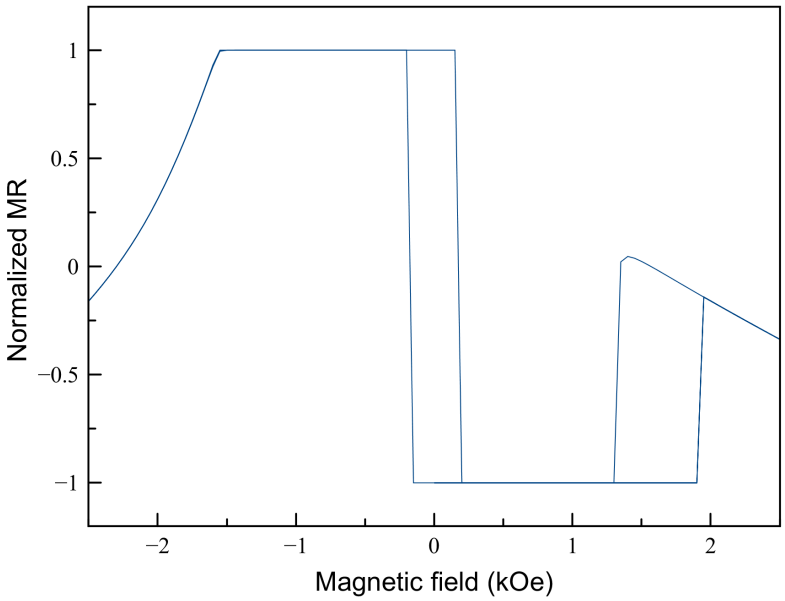

Figure 5.5: Micromagnetic simulation of the normalized magnetoresistance of the MTJ device. The hysteretic spin-flop at positive fields is qualitatively reproduced.

Because of the incommensurability of the nominal thicknesses and the simulation cell size of 1 nm×1 nm×1 nm, the magnetization in the simulation was scaled by the ratio of the nominal and simulated thickness. This discrepancy leads to implicit inaccuracy of the effective shape anisotropy and the interplay of the Zeeman effect and the RKKY interaction. The simulated switching fields, shown in figure 5.5, can therefore not exactly match the experimental values. The RKKY interaction value and the unidirectional anisotropy field (exchange bias) at the SAF bottom layer were manually adjusted until the simulated switching behavior qualitatively resembled the experimental data in figure 5.2. Considering the inaccuracies due to meshing and a simplified magnetic anisotropy model, the behavior is reproduced remarkably well. The static magnetization direction was then implemented into ANSYS finite-element simulation to calculate the stray field of the SAF at the position

of the FL, shown in figure 5.1. Again, while we cannot reliably calculate the absolute value of the stray field, its relative magnitude in the P- and SF-state and the nonuniformity can be assessed.

After simulating the switching behavior, a sinc-timed pulse of magnetic field was applied to the device. To excite spin wave modes of various spatial symmetries, the pulse was polarized in the out-of-plane direction, had a lateral Gauss shape with $\sim$20 nm width, and was centered asymmetrically in one of the ellipse quadrants. The decay of magnetization was Fourier-transformed to cell-specific frequency-domain amplitudes which are shown in figure 5.1. By evaluating the phase of the Fourier transform, we find that the mode $|1\rangle$ has phase-symmetric excitation maxima. All higher-order modes present with a 180° phase jump across each excitation node.

Chapter 6

Spin-Flip Switching of a Nanoscale Synthetic Antiferromagnet by Excitation of Individual Spin-wave Modes

The micromagnetic simulation of this work was done in collaboration with Roman Verba.

6.1 Introduction

In recent years, much attention has been given to a type of multilayer stack composed of thin layers of both magnetic and nonmagnetic materials. These combinations of

materials can result in unique properties due to surface and interface effects, making them useful for various applications. Of particular interest are synthetic antiferromagnets (SAF) within these multilayer magnetic systems, as they show promise for the development of FM-based spintronics that mimic antiferromagnet functionality.

SAF consist of two or more ferromagnetic layers separated by a non-magnetic metal spacer. These layers experience Ruderman-Kittel-Kasuya-Yosida (RKKY) interaction [24, 96], which causes them to align in an antiparallel fashion. This creates an artificial antiferromagnet [97], which has several advantages over traditional crystal antiferromagnets or ferromagnets. The primary benefit of SAFs is their higher thermal stability [98, 99] compared to conventional ferromagnetic materials, making them suitable for use in high temperature applications. Additionally, SAFs reduce the net magnetic moment of the material and have higher energy efficiency, resulting in lower power consumption and improved device performance. They are also compatible with current device fabrication processes and require minimal additional processing.

Several studies have been conducted to examine the interlayer coupling in synthetic antiferromagnetic (SAF) layers [100, 101, 102, 103] and the factors that lead to transitions between parallel (P) and antiparallel (AP) states in the multilayer structure of SAFs. For instance, spin-orbit torque (SOT) has been used to achieve deterministic switching of perpendicular SAFs [104, 105, 106], while a large external magnetic field is typically required to break symmetry. Additionally, field-free SOT-induced magnetization switching by adjusting the domain wall configuration between Bloch and Néel types has been reported [107]. It has also been demonstrated that the Neel vector of antiferromagnetically aligned SAFs

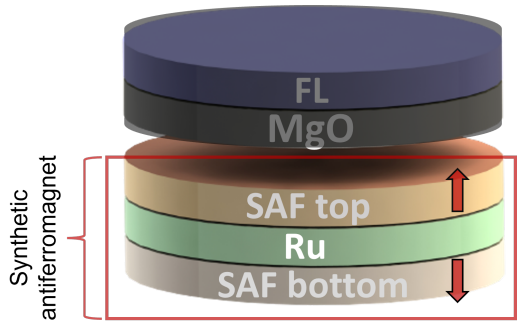

Figure 6.1: A trilayer synthetic antiferromagnet incorporated into an MTJ nanodevice.

can be switched by microwave pulses [107]. Here, we investigate the spin-flip switching of SAFs, which relies on SAF-resonant microwave pulses.

6.2 Experimental procedure and results

In this investigation, we analyze the spin-flip switching of synthetic antiferromagnetic (SAF) incorporated into a magnetic tunnel junction. MTJs are a key technology in spintronics and we use them as a sample platform to study SAF. We implement a perpendicular MTJ consisting of elliptical layers with perpendicular anisotropy. Each MTJ is composed of a ferromagnetic-free layer (FL), a MgO tunneling barrier, and a synthetic antiferromagnet with a Ru buffer layer. The SAF bottom is fixed by another antiferromagnetic layer through exchange-bias. All ferromagnetic layers are composed of CoFeB compounds.

A trilayer synthetic antiferromagnet is integrated into a magnetic tunnel junction nanodevice. The device's resistance is determined through a measurement of magnetoresistance, which is influenced by the tunneling magnetoresistance across the MgO layer, which involves the magnetization direction of the SAF top layer. An out-of-plane external mag-

netic field is applied to the device along the easy axis. By applying a sweeping field from positive to negative values, the device initially enters the parallel (P) state, as shown in the upper panel of figure 6.2 (a). The magnetic tunnel junction then exhibits a nearly rectangular hysteresis loop near zero field, which represents the expected magnetic reversal of the ferromagnetic-free layer (FL). At negative fields, the device switches to the antiparallel (AP) high-resistance state. The magnetic state diagram of FL, SAF top and bottom is illustrated in both P and AP states. The field is then reversed, from negative to positive, causing the free layer to rotate by 180° and the device to return to the low-resistance, parallel (P) state, as shown in the bottom panel of figure 6.2(a).

In order to examine the magnon spectra at the parallel (P) and antiparallel (AP) states, we utilize field-modulated spin-torque ferromagnetic resonance (ST-FMR) technique. With an out-of-plane magnetic field applied along the easy-axis, two distinct groups of modes are observed as shown in figure 6.2 (b). The first group, characterized by a V-shaped frequency-field dispersion, corresponds to the modes located in the free layer. The second group, composed of two modes with different slopes in the negative field region, is related to the modes present in the synthetic antiferromagnet (SAF).

We repeat the measurements but this time, a relatively large microwave pulse at the frequency of the SAF mode is applied. While measuring the magnetoresistance of the device from positive to negative field, at high negative fields, we observe that the device switches and the resistance abruptly drops to the parallel state, as shown in the top panel of figure 6.2 (c), but the free layer and SAF top are both pointing down. As the field is sweeped backward from negative to positive values, we see a small anomaly and an

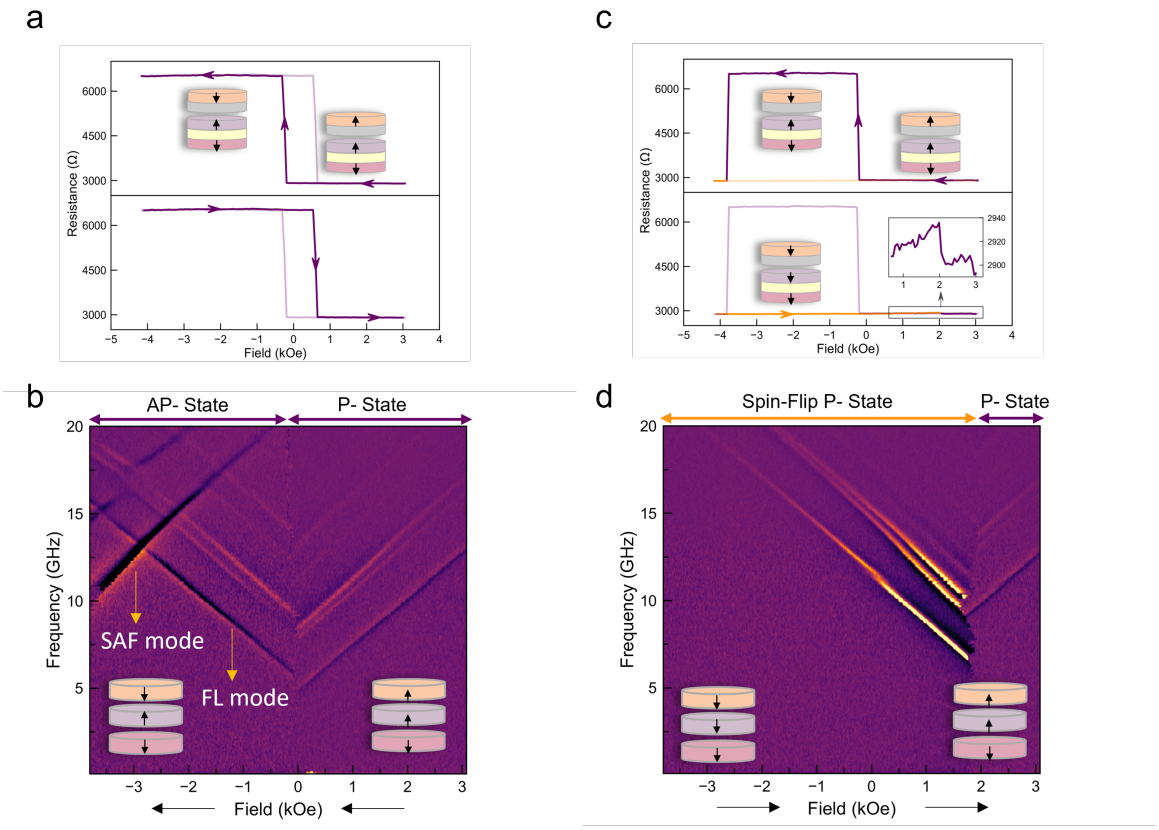

Figure 6.2: (a) Switching of the free layer between the parallel (P) and antiparallel (AP) states (b) Magnon modes originating from free layers and SAF in P- and AP-states. (c) Switching of the free layer and SAF top between normal parallel and spin-flip parallel states (d) Magnon modes originated from free layer and SAF in normal P- and spin-flip P-states.

additional switching at 2 kOe, the bottom panel of figure 6.2 (c). This indicates that the mutual orientation of the SAF top and free layer remains parallel, requiring both the SAF and free layer to switch, thus returning the device to its normal P-state.

We examine the magnon spectra as the external magnetic field is swept from negative to positive values. Notably, we observe the absence of SAF modes in this process. This can be attributed to the fact that the SAF is now in a spin-flip (SF) state, as opposed to the antiparallel (AP) state, resulting in the absence of the AP-state modes. As the field is increased to 2 kOe, only the left branch of the V-shaped modes can be observed in

the free layer (FL). Despite the fact that the FL is still pointing downward, these modes have shifted in response to the applied field. Further increases in the field result in the anomaly to occur at the field of 2 kOe and the device returning to its normal parallel (P) state. The magnon modes of FL reappear which is identical to the initial measurement. Our observations suggest that by applying a microwave pulse, the device can be switched in such a way that the SAF top layer flips from an upward to a downward orientation, a process referred to as spin-flip (SF) switching.

In order to investigate the nature of the switching process, we conduct experiments utilizing a train of pulses. These are RF pulses at the frequency of SAF mode. Additionally, DC current can be applied optionally via a DC current source. The number of pulses or duration required for the SAF to switch from the AP state to SF state is measured and the switching probability is determined by repeating the experiment multiple times. The top panel of figure 6.3 (b) illustrates the distribution of the data. In this particular instance, 180 pulses are applied to the device and the number of pulses required for switching is recorded. Upon repeating the measurement and recording the number of pulses required for switching in each case, it is observed that the data exhibited a log-normal distribution. In this example, it is determined that the most likely number of pulses required for switching is approximately 60, with a maximum of 80 pulses.

To further analyze the data, we integrated it to obtain the cumulative probability density of switching after a given period of time. The integral of the log-normal distribution is the error function, which is rather complex for further phenomenological evaluation. As an alternative, we fit the data with a straight line, from which we are able to determine

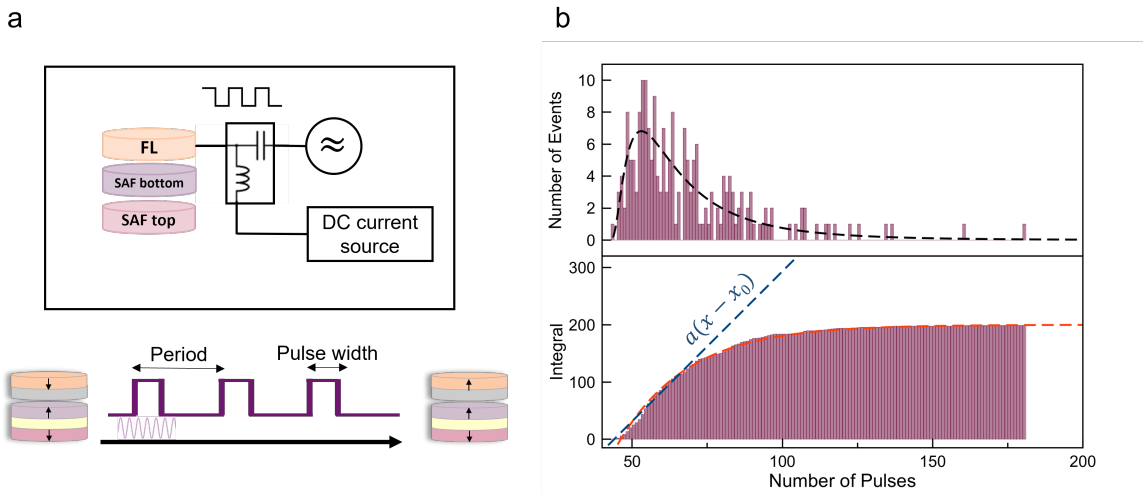

Figure 6.3: (a) Schematic of the measurement: AC and DC sources allow us to examine the probability of switching for variables such as pulse width, microwave power, and spin torque. (b) The probability density function for spin-flip switching of SAF is represented as a log normal distribution in the upper panel. The bottom panel depicts the integral of the probability density function, which is modeled with both the error function (red line) and linear fit (blue line).

two components: the delay (x_0), indicating the amount of time required for the device to switch, and the linear growth rate (a), representing the rate at which the switching probability approaches one.

We can investigate how two parameters, delay and growth rate, are affected by experimental variables such as pulse duration, microwave power, and current. We keep all of the parameters the same and carry out the experiment multiple times with varying pulse periods. As shown in figure 6.4 (a), we note that the delay increases linearly with the period, while the growth rate decreases proportionally to 1/period. Additionally, we investigate the delay and growth rate at various microwave powers. The first thing we notice when we increase the power is that the delay remains unchanged. However, it is evident that the growth rate increases with power, as shown in figure 6.4 (b). Comparing how delay

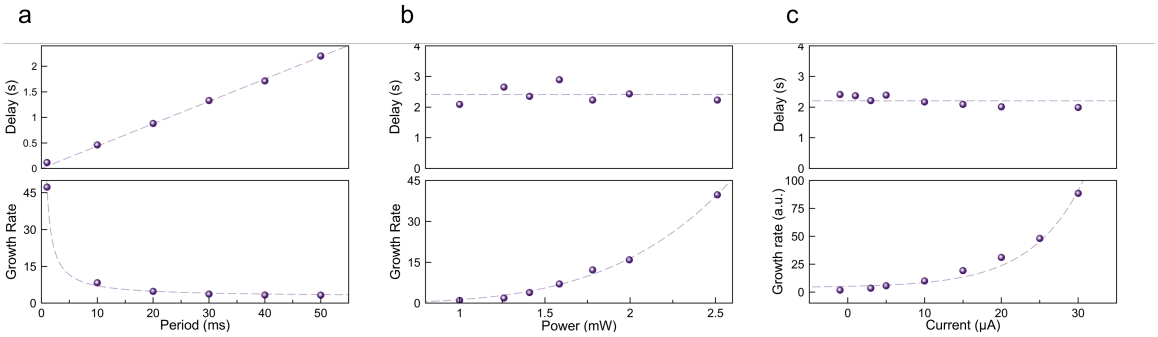

Figure 6.4: The effect of various factors on SAF switching probability: (a) delay increases linearly with period, and growth rate is proportional to frequency. (b) Pulse power has no effect on delay, but it does increase growth rate. (c) While spin current has little impact on delay, antidamping spin current facilitates switching.

is affected by pulse period and microwave power reveals that it is not just the amount of energy deposited into the system but also the frequency at which energy is deposited. This is the signature of a thermal wave. We conclude that not only does microwave-assisted switching play a role, but so does the thermal wave effect. This indicates that we likely have thermal spin torque that allows us to switch the device due to the accumulation of heat within it.

In addition to studying the impact of thermal spin torque on switching, we also aim to investigate the effect of regular spin torque. To achieve this, we apply a DC current, proportional to the spin torque. Our results, as depicted in figure 6.4 (c), indicate that the delay is not significantly affected. There may be a slight decrease, but it is negligible. However, when we apply an antidamping spin current relative to the SAF top (positive current), we observe a significant increase in the growth rate. On the other hand, when we apply a damping torque spin current (negative current), switching is prevented altogether.

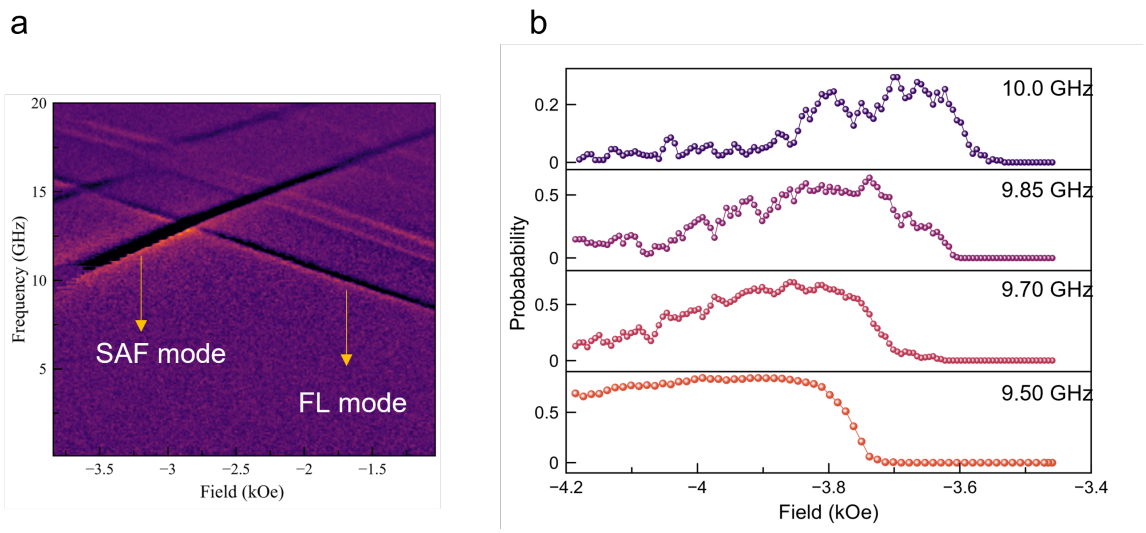

Figure 6.5: (a) Excitation of SAF modes with frequencies below FL magnons at high fields. (b) Fine structure in the frequency-field distribution of switching.

To this point, we have discussed the data collected at the lowest SAF mode frequency. However, upon examining the frequency-field dependence of switching probability, we discover that the switching probability displays a fine structure that is reproducible, as shown in figure 6.5 (b). We theorize that this intricate structure is related to the other standing spin waves in SAF that we have been unable to observe using ST-FMR. These modes may be more likely to be localized in the SAF bottom rather than the SAF top, or they may be unobservable due to symmetry. Despite their invisibility, the probability exhibits this fine structure, which is likely linked to additional spin wave modes in SAF.

6.3 Discussion

The frequency-field dependence of switching probability results in a reproducible fine structure, which leads us to consider the possibility of the existence of additional stand-

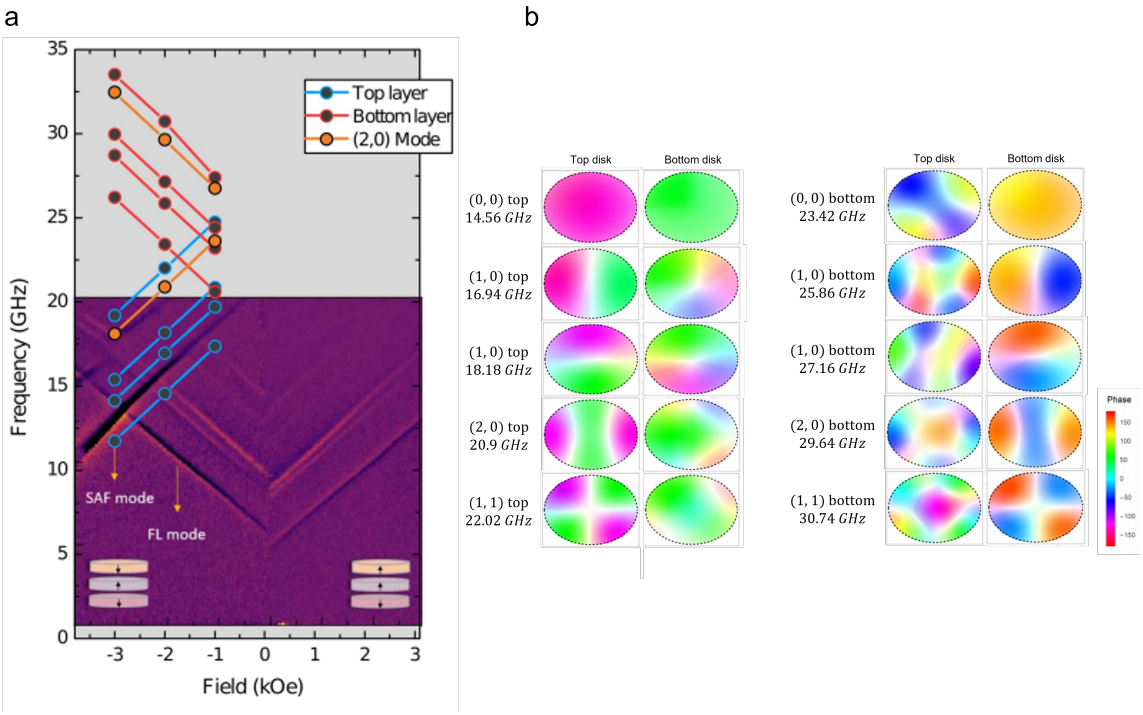

Figure 6.6: (a) Micromagnetic simulations show higher-order SAF spin-waves. For both the top and bottom SAF layers, there are four modes: (0,0), (0,1), (1,0), and (1,1). (1,1). We found the scarcely perceptible mode (2,0) using a certain excitation. (b) Mode profiles of SAF top and bottom measured at -2 kOe.

ing spin waves located in SAF that are not visible in experiments. To test this theory, we use micromagnetic simulation to compute the f(H) of SAF spin wave modes. The results, as shown in figure 6.6, confirm the presence of these standing waves. We observe four modes for both the top and bottom SAF layers: (0,0), (0,1), (1,0), and (1,1). Mode (2,0) is barely visible and was discovered using a specific excitation, but it is present in general cases. With uniform RF field excitation, (0,0) and weak (2,0) modes are observed. It appears that these modes are those observed in experimental spectra. RF Oersted fields excite modes (1,0) and (0,1), while (1,1) modes are not excited by these sources of excitation.

6.4 Conclusions

In conclusion, we have demonstrated magnetic switching of nanoscale Synthetic Anti-Ferromagnetic structures embedded in magnetic tunnel junction nanopillars. We have demonstrated that SAF spin-flip switching can be achieved through the application of microwave resonance pulses, and fine-tuned through the use of spin current. Our findings suggest that thermal spin current also contributes to the switching process. Our study reveals that the SAF structure switches not only at the lowest-order mode of spin waves, but also at higher-order modes. This expands the capabilities of current spintronic devices, offering potential new avenues for development.

Chapter 7

Anomalous Noise in Magnetic Tunnel Junctions and Magneto-Structural Transitions of Oxides

This chapter's material was carried out in collaboration with David Nelson.

7.1 Introduction

Noise is one of the most significant impediments to the performance of MTJs, which can significantly impair their functionality. Thus, it is crucial to comprehend and study the noise sources inside MTJ-based technologies, not only to identify solutions to

minimize noise disturbances but also to get a deeper understanding of the electric and magnetic properties of MTJs.

The numerous proposed applications for MTJs require operation in the low-frequency region, where noise predominates in the form of 1/f (pink) noise and random telegraph noise [108]. This noise is generally classified as Lorentzian noise. Both magnetic and electrical causes of Lorentzian noise in MTJs have been explored extensively. Magnetic Lorentzian noise is associated with domain fluctuations caused by pinning on defect sites [109, 110, 111] and edge roughness of the MTJ, while electrical noise is attributed to inhomogeneous tunneling caused by defects in the tunneling barrier and interfaces (charge trapping) [110, 112].

Noise in MTJs has been experimentally researched. It was discovered that the characteristics of Lorentzian noise in MTJs are substantial sample-to-sample variation and a nonlinear dependence on bias current [112, 113, 114, 115], external field [109, 110, 113, 114, 115] temperature [110, 112], annealing, geometry, composition [115], fabrication process, and sample history [110, 112].

Despite extensive research on Lorentzian noise in magnetic tunnel junctions (MTJs), the majority of studies have focused on the microscale. Only a limited number of investigations have addressed the phenomenon at the nanoscale. The defects in the tunneling barrier and at the interfaces play a critical role in random telegraph noise (RTN) and must be understood in order to reduce noise in MTJs. Previous research on microscale MTJs has demonstrated that temperature-dependent performance is a significant indicator of the quality of the MTJs [116, 117].

In sub-micron magnetic tunnel junctions (MTJs), where single defects play a significant role in noise, temperature-dependent random telegraph noise (RTN) may provide crucial insights into the quality of the barrier and interfaces, as well as the type of electrical Lorentzian noise. This study reports on temperature-dependent measurements of low-frequency noise and resistance on a variety of nanoscale MTJs, which demonstrate rapid changes in resistance at specific temperature ranges. These measurements were conducted over a range of temperatures. The variations in resistance were found to be associated with significant amounts of RTN that exhibit an Arrhenius law dependence on temperature.

Our results enable us to measure the energy of several active fluctuators throughout the temperature range. The prevalence of noise between devices suggests that the noise source is a material effect, and the specific temperature dependency suggests that charge trapping or phase transitions may be potential explanations.

7.2 Experimental procedure and results

Magnetic tunnel junction nanodevices serve as the subject of our experimental investigation. The devices consist of a $Co_{20}Fe_{60}B_{20}$-based free layer (FL) with a thickness of 1.8 nm, a 0.85 nm thick MgO tunneling barrier, and a $Co_{40}Fe_{40}B_{20}$ reference layer with a thickness of 2.4 nm (RL). 5 nm of Ta is used to cap the free layer. The reference layer is followed by layers of 0.85 nm Ru, 2.3 nm $Co_{70}Fe_{30}$ (BL), and 15 nm antiferromagnetic PtMn. The devices are fabricated in the shape of ellipses with a minor axis between 45 nm and 70 nm and a major axis between 90 nm and 170 nm. They were annealed at 300° C for two hours while a 10 kOe field was applied along the ellipse's principal axis.

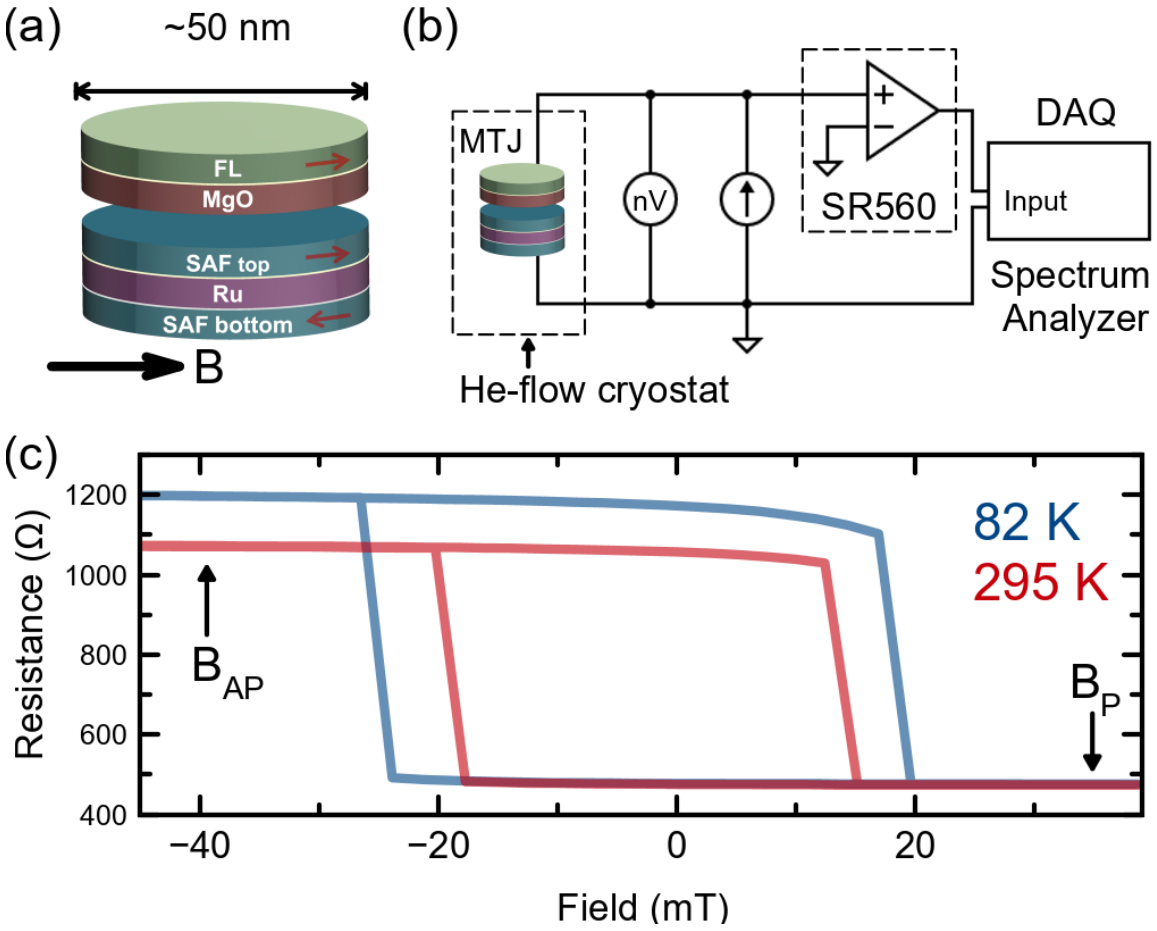

Figure 7.1: (a) Fundamental structure of magnetic multilayer MTJ (b) Effective circuit diagram of low-noise measurement apparatus: the MTJ is placed in a He-flow cryostat (dashed line) and biased by an external current source. A nanovolt meter is utilized to measure resistance. For time- and frequency-dependent data acquisition, a preamplified signal is employed. (c) Hysteresis of an average MTJ at 82K (blue) and 295K (orange) (red).

The magnetic layers of the MTJ exhibit magnetic anisotropy in the easy plane. Additionally, they possess easy-axis (ellipse major axis) anisotropy within the film plane, due to their elliptical shape. The RL and the BL are interlinked antiferromagnetically through RKKY interaction, forming a synthetic antiferromagnet. The BL layer has an exchange bias toward the PtMn layer that is aligned in the direction of the major axis of the ellipse.

7.2.1 Resistance and noise anomalies

Figure 7.1 (c) illustrates the resistance of the MTJ as a function of the in-plane magnetic field applied along the easy-axis. As anticipated for the easy-axis magnetization reversal of the free layer, the resistance is predominantly influenced by tunneling magnetoresistance, displaying a nearly square-shaped hysteresis loop. The low-resistance state corresponds to the parallel alignment of the free layer (FL) and reference layer (RL), whereas the high-resistance state corresponds to the antiparallel alignment. As the temperature drops, the coercive field and tunneling magnetoresistance ratio (TMR) both increase. The data is indicative of MTJs with easy-axis FL and steady synthetic antiferromagnet (SAF).

In the following study, we examine the resistance and noise characteristics of the MTJ devices as a function of temperature. For each device, a constant magnetic field is applied in the parallel state, which exceeds the coercive field. This ensures that the MTJ is in a well-defined, single-domain magnetic state.

The temperature-dependent resistance of a MTJ during discrete heating is depicted in figure 7.2 (a). This resistance was measured in the antiparallel state, with a 0.4 kOe external field and a 50 uA dc current applied as a bias. The MTJ resistance is observed

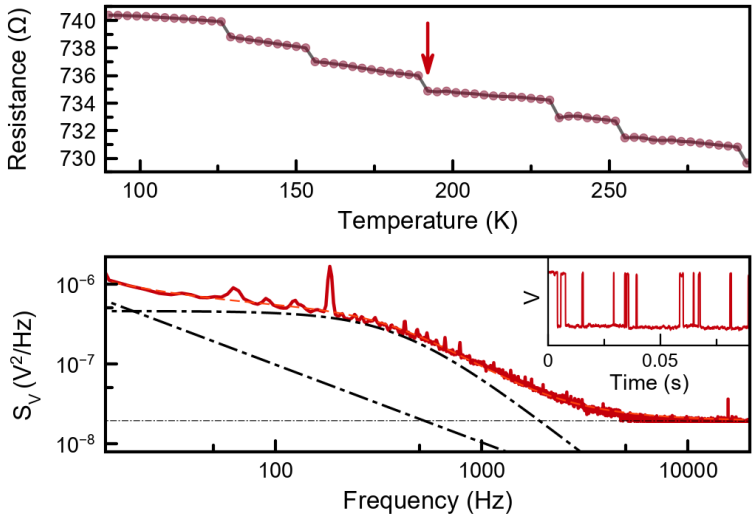

Figure 7.2: (Top) The resistance of an MTJ prepared in the parallel state is plotted against temperature, indicating resistance stages. (Bottom) Spectral density of the noise signal sampled between 185K and 205K resistance steps, as indicated by red and blue arrows. The spectrum in red shows a hump-like feature that is absent in the blue plot. Dashed lines are deconvolutions of the red plot into white, 1/f, and Lorentzian contributions. The side panel displays a time-domain red spectrum signal. The presence of step-like characteristics confirms that the origin of the Lorentzian in the red spectrum is, in fact, random telegraph noise.

to decrease as the temperature increases, and it exhibits periodic, step-like discontinuities of approximately 1 Ohm. Similar step-like patterns were observed in the resistance versus temperature graphs of the same MTJ measured in the parallel state.

To eliminate the possibility of systematic error, the measurements were also performed on a 50 Ohm resistor under the same bias conditions, with no indication of systematic artifacts found. An analysis of the hysteresis suggests that the bias field was significantly greater than the saturation field, hence it is unlikely that these step-like patterns had a magnetic origin.

To further investigate the resistance anomalies, we employ low-frequency noise spectroscopy in conjunction with a low-frequency spectrum analyzer and time-dependent

transport data. Figure 7.2 (b) illustrates a spectral density map recorded following a resistance step, as indicated in figure 7.2 (a). A distinct "hump" in the spectrum is indicative of Lorentzian-type noise. The time-domain trace of the voltage signal shows random telegraph noise (RTN), which means it switches between two voltage levels in a stochastic manner. We can see that RTN is present both before and after sudden changes in resistance during heating and cooling. To investigate the relationship between RTN, resistance, and temperature in different devices, we use a faster measurement method where a data acquisition system (DAQ) samples time-domain measurements and calculates spectra during post-processing.

7.2.2 Effects of temperature sweep rate

Figure 7.3 displays the temperature-dependent resistance of two MTJs undergoing continuous temperature cycling at different rates. As previously noted, both MTJs exhibit unusual resistance steps [118] as the temperature increases. The red curve in the upper panel represents the resistance state of an MTJ subjected to an average heating rate of 5.0 K/min. The resistance initially fluctuates between two states as the temperature rises, eventually settling into a high-resistance state around 100 K. When the resistance state becomes unstable and shifts to a low-resistance state, which is the state that the device remains in for the duration of the experiment, large fluctuations are observed once again at a temperature of approximately 170 K.

At a heating rate of 0.5 K/min (blue curve), the resistance of the same device experiences a period of intense variations starting at 100 K and then again, to a lesser extent, at 180 K. The size of the variations in resistance recorded at 100 K while operating at 0.5 K/min is similar to the resistance step observed when operating at 5 K/min; this

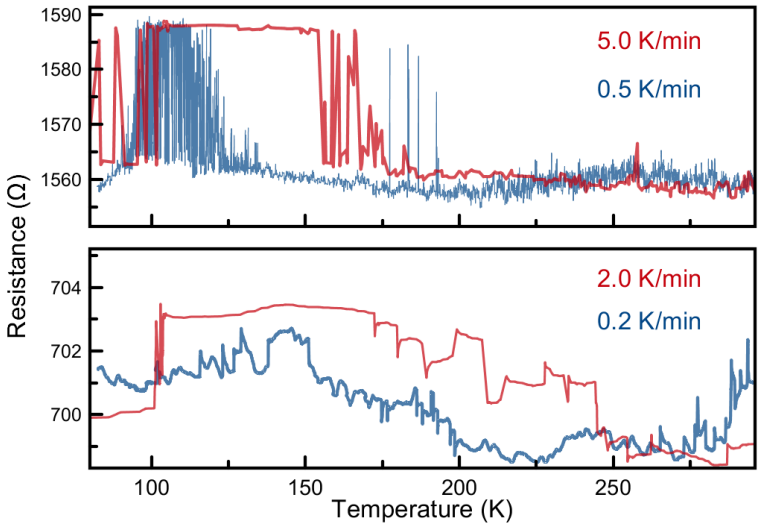

Figure 7.3: Resistance in temperature of two devices measured at two different heating rates shows different kinds of resistance anomalies, both reproducible. The top device shows a correlation between large and rapid two-level resistance fluctuations and heat rate. The bottom device shows discontinuous steps at 100K and after 160K.

is a phenomenon that can be qualitatively replicated. Time-domain measurements reveal that the fluctuation rate of the slower measurement is significantly higher than that of the quicker measurement, implying that slower heating is correlated with an increase in resistance fluctuations.

7.2.3 Correlation of resistance and noise anomalies

Figure 7.4 (a) depicts the resistance versus temperature curve seen in figure 7.3(a) at 5 K/min between the temperatures of 120 K and 185 K. Figure 7.4 (b) presents the time-domain resistance sampled at various temperatures along the curve. It also displays histogram inserts to highlight the status of the resistance during the course of the measurement. As can be seen in the 143K insert, we are capable of recognizing a DC offset in the time domain when operating at low temperatures and observing a smooth resistance.

However, when the temperature rises above 150 K, the time-domain begins to exhibit a prolonged RTN dwell time, favoring a high resistance state, as seen in the 152 K insert. The RTN exhibits an increasing preference for the low resistance state as the temperature rises, and as the temperature reaches 175K, the lower resistance state emerges as the one that is most favorable.

The observations show that the resistance changes closely resemble the RTN in temperature, and the same behavior is observed under slower heating at a similar temperature (RTN corresponding to resistance fluctuations), although the high resistance state is never sustained.

These observations suggest that the RTN is produced by discrete resistance fluctuations that occur reproducibly within a particular temperature zone. Moreover, the substantial dependence of these fluctuations on temperature suggests that the MTJ resistance state is likely metastable and that thermal energy triggers switching between two metastable states, which in turn leads to resistance fluctuations.

The majority of the MTJs that were studied showed temperature-dependent RTN that was correlated with changes in resistance. However, not all devices displayed consistent shifts in resistance. Some devices had substantial RTN and exhibited top and bottom resistance states.

Figure 7.3 (b) illustrates the resistance versus temperature plot for a different device when exposed to two different heating rates. It shows stepwise changes in resistance between 150K and 275K. Since the time-domain trace of this device showed a more complex

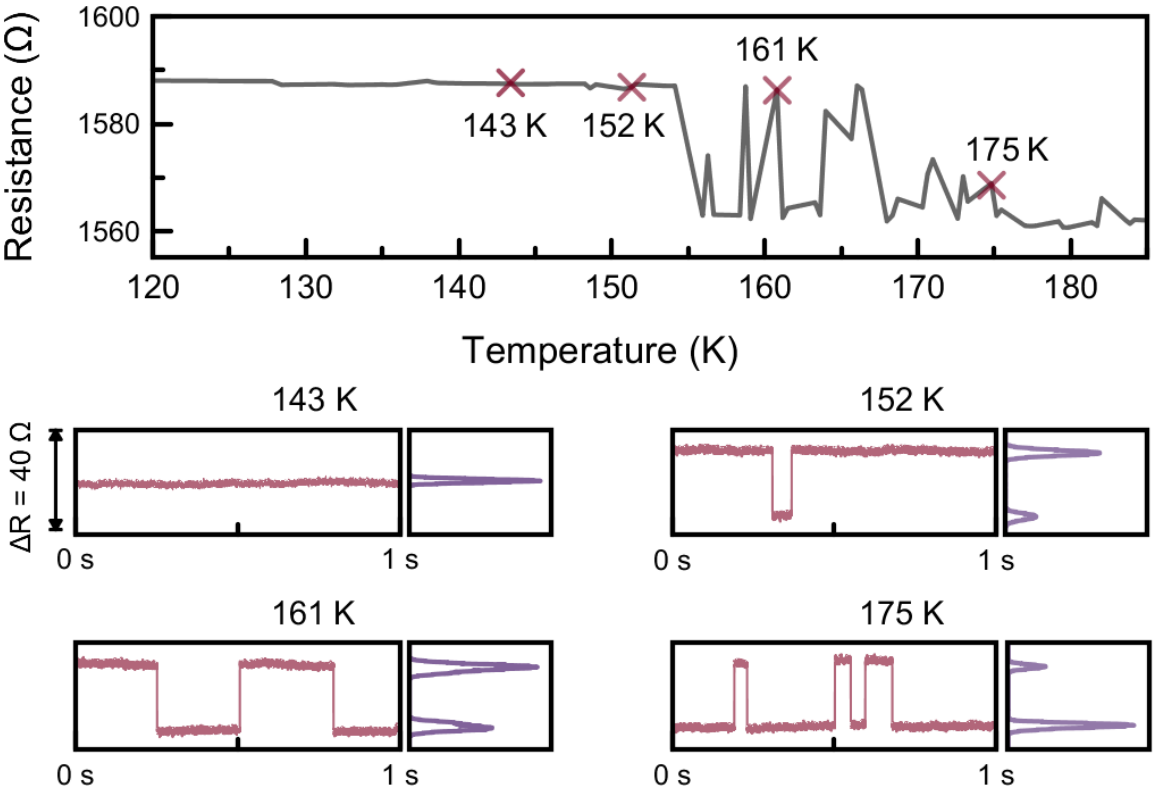

Figure 7.4: (Top panel) Resistance vs. temperature of a device as a function of increasing temperature at constant field and current: (Bottom panel) Time-domain signals sampled at 143K, 152K, 161K, and 175K are plotted below. Panel demonstrates that RTNs with increasing frequency characteristics suggest resistance instabilities.

dependence on temperature than the earlier studied device, Fourier transforms of the time domain were used to analyze the noise.

The inverse relationship between the heating rate and the fluctuation rate remains consistent, even though the stepwise changes in resistance have been observed. Unlike the previous device, the resistance steps in this case are much less pronounced and less rapid. Furthermore, the connection between the fluctuations in resistance and the noise in the time domain is not fully comprehended.

Figure 7.5 depicts the resistance condition of an MTJ. As the device is heated, the resistance demonstrates minor increments at 105K and from 174K to ambient temperature, which are associated with RTN. We observe at least four unique Lorentzian patterns in the frequency domain that match the reported RTN in the time domain.

Figure 7.5 shows the Lorentzian components of the noise, characterized by amplitude and f_{char}. At the start of the measurement at 80K, we observe a Lorentzian with $f_{char} \sim 3$ kHz that quickly decreases in frequency as we begin the heating cycle. At around 100K, a second Lorentzian (L2) with a low dwell time correlates to substantial variations in resistance that quickly stabilize within 4K of heating. With increasing temperature, f_{char} of L2 exponentially increases until at about 174 K, when low frequency RTN appears and a third Lorentzian (L3) is seen in frequency concurrently with L2, shown in the middle panel. Soon after the appearance of the second fluctuator, the resistance state undergoes a discontinuous step-down followed by a brief period of relaxation into an intermediate state. Unlike in the device we talked about before, the RTN in time is too small to account for the steps in resistance. As the heating continues, we see that the resistance steps show both set-ups (seen at 200K) as well as step-downs. The fluctuation rate of L3 increases exponentially in temperature until it merges with the background by 240K, an intriguing insight into the nature of the observed fluctuators. At 243K, a fourth fluctuator (L4) is observed in frequency and follows a similar trend as the other flucuators, merging into the background by 275K. Lorentzians L2-L4 emerge as low-frequency RTNs that undergo a rapid increase in fluctuation rate with increasing temperature.

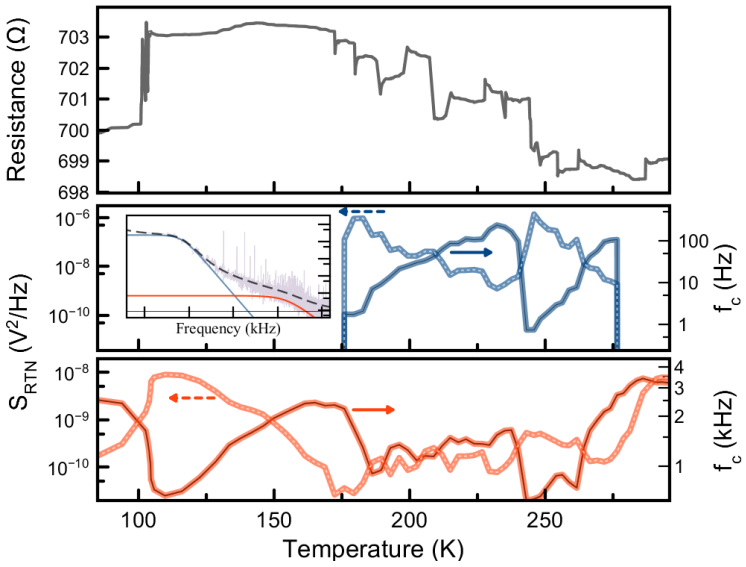

Figure 7.5: Spectral density amplitude (orange) and characteristic frequency (blue) of Lorentzian components of the frequency spectrum is plotted against increasing temperature. At various temperatures, a second, very low frequency Lorentzian emerges, with parameters plotted in top panel. Plot is grey is a the temperature dependent resistance of the device.

We believe this is an indication that the observed flucuators share a common thermal dependence in their relaxation mechanisms that can be modeled by the Arrhenius equation $f = f_0 \exp(\Delta E/K_B T)$. Plotting the $\ln(f_{char})$ as a function of $1/K_B T$, we find that the slopes of the characteristic frequency in temperature of the observed Lorentzians follow a linear trend. In addition, we find that the flucuator activation temperature is proportional to the slope of $\ln(f_{char})$ vs $1/K_B T$. Based on these two findings, we can conclude that the observed fluctuators conform to the Arrhenius equation, providing evidence that the fluctuators are switching between meta-stable states and that the energy barrier of the fluctuator is given by the slope of $\ln(f_{char})$. It is likely that L1 too follows this trend; however, we do not have the low temperature data to support this claim.

7.3 Discussion

As the presence of a strong magnetic field eliminates the possibility of a magnetic origin for the metastability, we have directed our investigation towards the electrical response of the noise. Bias-dependent measurements were performed at room temperature, revealing that beyond a certain threshold current, RTN is observable. This level is similar to what has been previously reported in much larger MTJs. This phenomenon has been attributed to the trapping of charges in the tunneling barrier [119, 120] and is a potential explanation for the thermally induced metastability that we find. It is a well-established fact that the build-up of charges in the vicinity of defect sites reduces the probability of tunneling locally. In situations where the thermal energy is comparable to the energy of the charge barrier, the release and recapture of electrons from these defect sites can lead to metastable fluctuations in tunneling that resemble Lorentzian noise.

Other phenomena besides charge trapping can explain the Lorentzian noise we observe. A recent study [118] shows that temperature-dependent resistance changes in CoFeB/MgO MTJs and thin films can be explained by the phase transitions of defects and impurities at the metal-oxide interface. These imperfections can be nanoscopic defects of a variety of metal oxides that are a residue of the manufacturing process and can remain even after annealing has taken place. These oxides, such as F_2O_3, F_3O_4 and CoO, can exhibit temperature-dependent magnetocrystalline phase transitions that drastically change the electric and magnetic properties of the material, even within nanoscale crystals [121, 122].

In addition, studies have shown that dramatic changes in noise also occurs across phases and even during the phase transition itself [123]. As the defects that are expected

to exist within our MTJs are likely to be on the scale of only a few tens of molecules, the structural phase transitions will take place in a different manner. Barry et. al. has shown that atomic clusters exhibit a phenomenon related to phase transitions known as structural isomerization in which meta-stable transition between phases can occur independent of temperature. It has been shown that atomic cluster undergo phase switching, distinct from phase transition, at a rate determined by the energy difference between phase states.

Moreover, highly dense atomic cluster show temperature independent energy barrier between phases and are believed to undergo switching in accordance with the Arrhenius law. As an atomic cluster switches from one phase to the other, the electric and magnetic properties of the noise are likely to change as well. The diverse time scales of the Lorentzian noise is a distinct signatures of both small and large defect in our device. This indicates that relatively simple temperature dependent measurement can be used to resolve the energy barrier generated by charge traps and even estimate the number of charge traps in a device, an important metric for characterizing the quality of MTJs.

7.4 Conclusions

In conclusion, we investigated noise and resistance measurements in nanoscale CoFeB-based MTJ nanopillars as a function of temperature. We discovered relationships between resistance anomalies with step-like patterns and random telegraph noise. Due to the fact that the bias field was significantly greater than the saturation field, this indicates that the origin of these stair-like patterns was not magnetic. According to our findings, this noise is the result of Iron-Cobalt-Oxide nanoclusters undergoing magneto-structural phase

transitions at the interface between the free layer and tunneling layer. We also investigated the effects of sweep rate and discovered that the resistance fluctuation rate of the slower measurement is significantly higher than that of the faster measurement, indicating that slower heating correlates with a rise in resistance fluctuations.

Chapter 8

Conclusion

In this dissertation, I have focused on the nonlinear magnetization dynamics in zero-dimensional magnets. Resonant nonlinear magnon-magnon scattering processes as a critical factor for magnetic damping are investigated. When compared to bulk ferromagnets, confinement discretizes the spin wave spectrum and reduces multimagnon scattering rate in nanomagnets, resulting in unique nonlinear magnon interactions and excitation processes. The predominant resonant nonlinear processes, including degenerate and non-degenerate three magnon scattering and resonant four magnon scattering, are experimentally observed in magnetic tunnel junctions, demonstrating these processes can alter the response of a nanomagnet to an antidamping spin-torque in an unexpected way, where antidamping torque can actually increase the damping.

Additionally, I have studied the engineering of magnon interactions in nanoscale magnets through the application of a stray field that is nonuniform at the nanoscale. The local field is generated by exploiting the hysteretic spin-flop transition of a synthetic antifer-

romagnet. By utilizing this method, I have successfully controlled the toggling of magnon interactions by at least one order of magnitude, allowing for better control over dissipation in spin-torque applications. Further studies are necessary to understand the quantitative connection between the magnon scattering, the micromagnetic state of the nanomagnet, and the symmetry of the stray field.

Furthermore, I have investigated the spin flip switching of a nanoscale synthetic antiferromagnetic incorporated in magnetic tunnel junction nanopillars by sending SAF-resonant microwave pulses. The goal was to understand the tunability of this phenomenon using spin-polarized current. The results showed that while antidamping spin torque increases the switching probability, damping spin torque stops it. Delay indicates that there is a contribution to the switching from thermal spin current. The observations also revealed that the SAF not only switches at the lowest order of magnon modes, but it is also affected by higher order modes. The results highlight the importance of understanding the interplay between spin-polarized current, damping and thermal effects, and magnon modes in the design and optimization of spintronic devices.

Finally, we studied the relationship between temperature and resistance measurements in CoFeB-based MTJ nanopillars. Our findings revealed that resistance anomalies with step-like patterns and random telegraph noise are related. The high bias field compared to the saturation field indicated that the source of these anomalies was not magnetic in nature. Further investigation suggested that the cause of these anomalies was due to magneto-structural transitions at the interface between the free layer and tunneling layer of the MTJ. The results also showed that resistance and noise performance at room tem-

perature could be adjusted through temperature cycling, with slower heating correlating to a higher resistance fluctuation rate and, consequently, a higher RTN noise.

Bibliography

[1] R. Meckenstock, I. Barsukov, C. Bircan, A. Remhoff, D. Dietzel, and D. Spoddig. Imaging of ferromagnetic-resonance excitations in permalloy nanostructures on si using scanning near-field thermal microscopy. *Journal of Applied Physics*, 99(8):08C706, 2006. doi: 10.1063/1.2171929. URL `https://doi.org/10.1063/1.2171929`.

[2] Jacob Torrejon, Mathieu Riou, Flavio Abreu Araujo, Sumito Tsunegi, Guru Khalsa, Damien Querlioz, Paolo Bortolotti, Vincent Cros, Kay Yakushiji, Akio Fukushima, Hitoshi Kubota, Shinji Yuasa, Mark D Stiles, and Grollier Julie. Neuromorphic computing with nanoscale spintronic oscillators. *Nature*, 547(7664):428–431, 2017.

[3] Gouhei Tanaka, Toshiyuki Yamane, Jean Benoit Héroux, Ryosho Nakane, Naoki Kanazawa, Seiji Takeda, Hidetoshi Numata, Daiju Nakano, and Akira Hirose. Recent advances in physical reservoir computing: A review. *Neural Netw.*, 115:100 – 123, 2019. doi: https://doi.org/10.1016/j.neunet.2019.03.005.

[4] D. Marković, N. Leroux, M. Riou, F. Abreu Araujo, J. Torrejon, D. Querlioz, A. Fukushima, S. Yuasa, J. Trastoy, P. Bortolotti, and J. Grollier. Reservoir computing with the frequency, phase, and amplitude of spin-torque nano-oscillators. *Appl. Phys. Lett.*, 114(1):012409, 2019. doi: 10.1063/1.5079305.

[5] SSP Parkin, KP Roche, MG Samant, PM Rice, RB Beyers, RE Scheuerlein, EJ O'sullivan, SL Brown, J Bucchigano, DW Abraham, et al. Exchange-biased magnetic tunnel junctions and application to nonvolatile magnetic random access memory. *Journal of Applied Physics*, 85(8):5828–5833, 1999.

[6] Andrii V Chumak, Vitaliy I Vasyuchka, Alexander A Serga, and Burkard Hillebrands. Magnon spintronics. *Nat. Phys.*, 11(6):453–461, 2015.

[7] Arezoo Etesamirad, Rodolfo Rodriguez, Joshua Bocanegra, Roman Verba, Jordan Katine, Ilya N Krivorotov, Vasyl Tyberkevych, Boris Ivanov, and Igor Barsukov. Controlling magnon interaction by a nanoscale switch. *ACS Applied Materials & Interfaces*, 13(17):20288–20295, 2021.

[8] Rodolfo Rodriguez, Shirash Regmi, Hantao Zhang, Wei Yuan, Pavlo Makushko, Eric A. Montoya, Ihor Veremchuk, René Hübner, Denys Makarov, Jing Shi, Ran Cheng, and Igor Barsukov. Robust spin injection via thermal magnon pumping in antiferromagnet/ferromagnet hybrid systems. *Phys. Rev. Res.*, 4:033139, Aug 2022. doi: 10.1103/PhysRevResearch.4.033139. URL `https://link.aps.org/doi/10.1103/PhysRevResearch.4.033139`.

[9] T. C. Damen, Luis Via, J. E. Cunningham, Jagdeep Shah, and L. J. Sham. Subpicosecond spin relaxation dynamics of excitons and free carriers in gaas quantum wells. *Phys. Rev. Lett.*, 67:3432–3435, Dec 1991. doi: 10.1103/PhysRevLett.67.3432. URL `https://link.aps.org/doi/10.1103/PhysRevLett.67.3432`.

[10] J. A. Katine and Eric E. Fullerton. Device implications of spin-transfer torques. *J. Magn. Magn.*, 320(7):1217 – 1226, 2008. doi: https://doi.org/10.1016/j.jmmm.2007.12.013.

[11] D. Bedau, H. Liu, J.-J. Bouzaglou, A. D. Kent, J. Z. Sun, J. A. Katine, E. E. Fullerton, and S. Mangin. Ultrafast spin-transfer switching in spin valve nanopillars with perpendicular anisotropy. *Appl. Phys. Lett.*, 96(2):022514, 2010. doi: 10.1063/1.3284515.

[12] S. Ikeda, J. Hayakawa, Y. M. Lee, F. Matsukura, Y. Ohno, T. Hanyu, and H. Ohno. Magnetic tunnel junctions for spintronic memories and beyond. *IEEE Trans. Electron Devices*, 54(5):991–1002, 2007. doi: 10.1109/TED.2007.894617.

[13] S. Yuasa, A. Fukushima, K. Yakushiji, T. Nozaki, M. Konoto, H. Maehara, H. Kubota, T. Taniguchi, H. Arai, H. Imamura, K. Ando, Y. Shiota, F. Bonell, Y. Suzuki, N. Shimomura, E. Kitagawa, J. Ito, S. Fujita, K. Abe, K. Nomura, H. Noguchi, and H. Yoda. Future prospects of mram technologies. pages 3.1.1–3.1.4, 2013. doi: 10.1109/IEDM.2013.6724549.

[14] D. C. Worledge, G. Hu, David W. Abraham, J. Z. Sun, P. L. Trouilloud, J. Nowak, S. Brown, M. C. Gaidis, E. J. O'Sullivan, and R. P. Robertazzi. Spin torque switching of perpendicular ta/cofeb/mgo-based magnetic tunnel junctions. *Appl. Phys. Lett.*, 98(2):022501, 2011. doi: 10.1063/1.3536482.

[15] Vladislav E. Demidov, Sergei Urazhdin, Henning Ulrichs, Vasyl Tiberkevich, Andrei Slavin, Dietmar Baither, Guido Schmitz, and Sergej O. Demokritov. Magnetic nano-oscillator driven by pure spin current. *Nat. Mater.*, 11(12):1028–1031, 2012. doi: 10.1038/nmat3459.

[16] JC Sankey, IN Krivorotov, NC Emley, RJ Schoelkopf, RA Buhrman, and DC Ralph. Microwave oscillations of a nanomagnet driven by a spin-polarized current. *nature*, 425(6956):380–383, 2003.

[17] Alina M Deac, Akio Fukushima, Hitoshi Kubota, Hiroki Maehara, Yoshishige Suzuki, Shinji Yuasa, Yoshinori Nagamine, Koji Tsunekawa, David D Djayaprawira, and Naoki Watanabe. Bias-driven high-power microwave emission from mgo-based tunnel magnetoresistance devices. *Nat. Phys.*, 4(10):803–809, 2008.

[18] M Evelt, C Safranski, Mohammed Aldosary, V E Demidov, I Barsukov, A P Nosov, A B Rinkevich, K Sobotkiewich, Xiaoqin Li, Jing Shi, I. N. Krivorotov, and S. O. Demokritov. Spin hall-induced auto-oscillations in ultrathin yig grown on pt. *Sci. Rep.*, 8(1):1269, 2018.

[19] Eric Montoya, Thomas Sebastian, Helmut Schultheiss, Bret Heinrich, Robert E Camley, and Zbigniew Celinski. Magnetization dynamics. In *Handbook of Surface Science*, volume 5, pages 113–167. Elsevier, 2015.

[20] I. Barsukov, H. K. Lee, A. A. Jara, Y.-J. Chen, A. M. Gonçalves, C. Sha, J. A. Katine, R. E. Arias, B. A. Ivanov, and I. N. Krivorotov. Giant nonlinear damping in nanoscale ferromagnets. *Sci. Adv.*, 5(10):eaav6943, 2019. doi: 10.1126/sciadv.aav6943.

[21] Igor Žutić, Jaroslav Fabian, and S. Das Sarma. Spintronics: Fundamentals and applications. *Rev. Mod. Phys.*, 76:323–410, Apr 2004. doi: 10.1103/RevModPhys.76.323. URL `https://link.aps.org/doi/10.1103/RevModPhys.76.323`.

[22] Evgeny Y Tsymbal, Oleg N Mryasov, and Patrick R LeClair. Spin-dependent tunnelling in magnetic tunnel junctions. *Journal of Physics: Condensed Matter*, 15(4): R109, 2003.

[23] Bernard Diény. Giant magnetoresistance in spin-valve multilayers. *Journal of Magnetism and Magnetic Materials*, 136(3):335–359, 1994.

[24] John MD Coey. *Magnetism and magnetic materials*. Cambridge university press, 2010.

[25] S Yuasa and DD Djayaprawira. Giant tunnel magnetoresistance in magnetic tunnel junctions with a crystalline mgo (0 0 1) barrier. *Journal of Physics D: Applied Physics*, 40(21):R337, 2007.

[26] JM MacLaren, X-G Zhang, and WH Butler. Validity of the julliere model of spin-dependent tunneling. *Physical Review B*, 56(18):11827, 1997.

[27] Jian-Gang (Jimmy) Zhu and Chando Park. Magnetic tunnel junctions. *Materials Today*, 9(11):36–45, 2006. ISSN 1369-7021. doi: https://doi.org/10.1016/S1369-7021(06)71693-5. URL `https://www.sciencedirect.com/science/article/pii/S1369702106716935`.

[28] S Ikeda, J Hayakawa, Y Ashizawa, YM Lee, K Miura, H Hasegawa, M Tsunoda, F Matsukura, and H Ohno. Tunnel magnetoresistance of 604% at 300 k by suppression of ta diffusion in co fe b/ mg o/ co fe b pseudo-spin-valves annealed at high temperature. *Applied Physics Letters*, 93(8):082508, 2008.

[29] I. Barsukov, S. Mankovsky, A. Rubacheva, R. Meckenstock, D. Spoddig, J. Lindner, N. Melnichak, B. Krumme, S. I. Makarov, H. Wende, H. Ebert, and M. Farle. Magnetocrystalline anisotropy and gilbert damping in iron-rich $fe_{1-x}si_x$ thin films. *Phys. Rev. B*, 84:180405, Nov 2011. doi: 10.1103/PhysRevB.84.180405. URL `https://link.aps.org/doi/10.1103/PhysRevB.84.180405`.

[30] YN Zhang, JX Cao, I Barsukov, J Lindner, B Krumme, H Wende, and RQ Wu. Magnetocrystalline anisotropy of fe-si alloys on mgo (001). *Physical Review B*, 81 (14):144418, 2010.

[31] Yu Fu, I Barsukov, Jing Li, AM Gonçalves, CC Kuo, M Farle, and IN Krivorotov. Temperature dependence of perpendicular magnetic anisotropy in cofeb thin films. *Applied Physics Letters*, 108(14):142403, 2016.

[32] EB Myers, DC Ralph, JA Katine, RN Louie, and RA Buhrman. Current-induced switching of domains in magnetic multilayer devices. *Science*, 285(5429):867–870, 1999.

[33] J. A. Katine, F. J. Albert, R. A. Buhrman, E. B. Myers, and D. C. Ralph. Current-driven magnetization reversal and spin-wave excitations in co /cu /co pillars. *Phys. Rev. Lett.*, 84:3149–3152, Apr 2000. doi: 10.1103/PhysRevLett.84.3149. URL `https://link.aps.org/doi/10.1103/PhysRevLett.84.3149`.

[34] Charles Kittel. On the theory of ferromagnetic resonance absorption. *Phys. Rev.*, 73:155–161, Jan 1948. doi: 10.1103/PhysRev.73.155. URL `https://link.aps.org/doi/10.1103/PhysRev.73.155`.

[35] J.C. Slonczewski. Current-driven excitation of magnetic multilayers. *Journal of Magnetism and Magnetic Materials*, 159(1):L1–L7, 1996. ISSN 0304-8853. doi: https://doi.org/10.1016/0304-8853(96)00062-5. URL https://www.sciencedirect.com/science/article/pii/0304885396000625.

[36] L. Berger. Emission of spin waves by a magnetic multilayer traversed by a current. *Phys. Rev. B*, 54:9353–9358, Oct 1996. doi: 10.1103/PhysRevB.54.9353. URL https://link.aps.org/doi/10.1103/PhysRevB.54.9353.

[37] D.C. Ralph and M.D. Stiles. Spin transfer torques. *Journal of Magnetism and Magnetic Materials*, 320(7):1190–1216, 2008. ISSN 0304-8853. doi: https://doi.org/10.1016/j.jmmm.2007.12.019. URL https://www.sciencedirect.com/science/article/pii/S0304885307010116.

[38] Bassim Arkook, Christopher Safranski, Rodolfo Rodriguez, Ilya N Krivorotov, Tobias Schneider, Kilian Lenz, Jürgen Lindner, Houchen Chang, Mingzhong Wu, Yaroslav Tserkovnyak, et al. Thermally driven two-magnet nano-oscillator with large spin-charge conversion. *arXiv preprint arXiv:1909.12445*, 2019.

[39] Arnold Markovich Kosevich, BA Ivanov, and AS Kovalev. Magnetic solitons. *Physics Reports*, 194(3-4):117–238, 1990.

[40] Mingzhong Wu, Boris A Kalinikos, and Carl E Patton. Self-generation of chaotic solitary spin wave pulses in magnetic film active feedback rings. *Physical review letters*, 95(23):237202, 2005.

[41] H. Suhl. The theory of ferromagnetic resonance at high signal powers. *Journal of Physics and Chemistry of Solids*, 1(4):209–227, 1957. ISSN 0022-3697. doi: https://doi.org/10.1016/0022-3697(57)90010-0. URL https://www.sciencedirect.com/science/article/pii/0022369757900100.

[42] Hans G Bauer, Peter Majchrak, Torsten Kachel, Christian H Back, and Georg Woltersdorf. Nonlinear spin-wave excitations at low magnetic bias fields. *Nature Communications*, 6(1):8274, 2015.

[43] Yihong Cheng, Kai Chen, and Shufeng Zhang. Interplay of magnon and electron currents in magnetic heterostructure. *Physical Review B*, 96(2):024449, 2017.

[44] PTT Le, BD Hoi, and Mohsen Yarmohammadi. Magnon-impurity interaction effect on the magnonic heat capacity of the lieb lattice. *AIP Advances*, 8(12):125317, 2018.

[45] DA Bozhko, VI Vasyuchka, AV Chumak, and AA Serga. Magnon-phonon interactions in magnon spintronics. *Low Temperature Physics*, 46(4):383–399, 2020.

[46] M d'Aquino, A Quercia, V Scalera, S Perna, G Bertotti, ID Mayergoyz, and C Serpico. Analytical treatment of nonlinear ferromagnetic resonance in nanomagnets. *IEEE Transactions on Magnetics*, 53(11):1–5, 2017.

[47] CT Boone, JA Katine, JR Childress, Vasil Tiberkevich, Andrei Slavin, Jian Zhu, Xiao Cheng, and IN Krivorotov. Resonant nonlinear damping of quantized spin waves in ferromagnetic nanowires: A spin torque ferromagnetic resonance study. *Physical review letters*, 103(16):167601, 2009.

[48] Igor BARSUKOV, Han Kyu LEE, Alejandro A. JARA, Yu-Jin CHEN, Alexandre M. GONÇALVES, Chengcen SHA, Jordan A. KATINE, Rodrigo E. ARIAS, Boris A. IVANOV, and Ilya N. KRIVOROTOV. Inversion of the spin-torque effect in mtjs via resonant magnon scattering. In *2020 IEEE 31st Magnetic Recording Conference (TMRC)*, pages 1–2, 2020. doi: 10.1109/TMRC49521.2020.9366713.

[49] Feng Guo, Lyubov M. Belova, and Robert D. McMichael. Nonlinear ferromagnetic resonance shift in submicron permalloy ellipses. *Phys. Rev. B*, 91:064426, Feb 2015. doi: 10.1103/PhysRevB.91.064426.

[50] Hans T Nembach, Justin M Shaw, Carl T Boone, and Thomas J Silva. Mode-and size-dependent landau-lifshitz damping in magnetic nanostructures: evidence for nonlocal damping. *Physical review letters*, 110(11):117201, 2013.

[51] Andrei Slavin and Vasil Tiberkevich. Nonlinear auto-oscillator theory of microwave generation by spin-polarized current. *IEEE Trans. Magn.*, 45(4):1875–1918, 2009.

[52] Cheng P Wen. Coplanar waveguide: A surface strip transmission line suitable for nonreciprocal gyromagnetic device applications. *IEEE Transactions on Microwave Theory and Techniques*, 17(12):1087–1090, 1969.

[53] Yu-Jin Chen, Han Kyu Lee, Roman Verba, Jordan A Katine, Igor Barsukov, Vasil Tiberkevich, John Q Xiao, Andrei N Slavin, and Ilya N Krivorotov. Parametric resonance of magnetization excited by electric field. *Nano letters*, 17(1):572–577, 2017.

[54] J. C. Sankey, P. M. Braganca, A. G. F. Garcia, I. N. Krivorotov, R. A. Buhrman, and D. C. Ralph. Spin-transfer-driven ferromagnetic resonance of individual nanomagnets.

Phys. Rev. Lett., 96:227601, Jun 2006. doi: 10.1103/PhysRevLett.96.227601. URL https://link.aps.org/doi/10.1103/PhysRevLett.96.227601.

[55] A M Gonçalves, I Barsukov, Y J Chen, L Yang, J A Katine, and I N Krivorotov. Spin torque ferromagnetic resonance with magnetic field modulation. *Appl. Phys. Lett.*, 103(17):172406, 2013.

[56] I Barsukov, Yu Fu, A M Gonçalves, M Spasova, M Farle, L C Sampaio, R E Arias, and I N Krivorotov. Field-dependent perpendicular magnetic anisotropy in cofeb thin films. *Appl. Phys. Lett.*, 105(15):152403, 2014.

[57] S Rumyantsev, M Balinskiy, F Kargar, A Khitun, and AA Balandin. The discrete noise of magnons. *Applied Physics Letters*, 114(9):090601, 2019.

[58] Vasyl Tyberkevych, Andrei Slavin, Petro Artemchuk, and Graham Rowlands. Vector hamiltonian formalism for spin-wave dynamics. *arXiv:2011.13562*, 2020.

[59] GD Fuchs, JC Sankey, VS Pribiag, L Qian, PM Braganca, AGF Garcia, EM Ryan, Zhi-Pan Li, O Ozatay, DC Ralph, et al. Spin-torque ferromagnetic resonance measurements of damping in nanomagnets. *Applied Physics Letters*, 91(6):062507, 2007.

[60] Kh Zakeri, J Lindner, I Barsukov, R Meckenstock, M Farle, U Von Hörsten, H Wende, W Keune, J Rocker, SS Kalarickal, et al. Spin dynamics in ferromagnets: Gilbert damping and two-magnon scattering. *Physical Review B*, 76(10):104416, 2007.

[61] J Lindner, I Barsukov, C Raeder, C Hassel, O Posth, R Meckenstock, P Landeros, and DL Mills. Two-magnon damping in thin films in case of canted magnetization: Theory versus experiment. *Physical Review B*, 80(22):224421, 2009.

[62] Tobias Hula, Katrin Schultheiss, Aleksandr Buzdakov, Lukas Körber, Mauricio Bejarano, Luis Flacke, Lukas Liensberger, Mathias Weiler, Justin M. Shaw, Hans T. Nembach, Jürgen Fassbender, and Helmut Schultheiss. Nonlinear losses in magnon transport due to four-magnon scattering. *Appl. Phys. Lett.*, 117(4):042404, 2020. doi: 10.1063/5.0015269.

[63] H. Schultheiss, K. Vogt, and B. Hillebrands. Direct observation of nonlinear four-magnon scattering in spin-wave microconduits. *Phys. Rev. B*, 86:054414, Aug 2012. doi: 10.1103/PhysRevB.86.054414.

[64] GA Melkov, DV Slobodianiuk, VS Tiberkevich, G De Loubens, O Klein, and AN . Nonlinear ferromagnetic resonance in nanostructures having discrete spectrum of spin-wave modes. *IEEE Magnetics Letters*, 4:4000504–4000504, 2013.

[65] K. Schultheiss, R. Verba, F. Wehrmann, K. Wagner, L. Körber, T. Hula, T. Hache, A. Kákay, A. A. Awad, V. Tiberkevich, A. N. Slavin, J. Fassbender, and H. Schultheiss. Excitation of whispering gallery magnons in a magnetic vortex. *Phys. Rev. Lett.*, 122:097202, Mar 2019.

[66] P. K. Muduli, Ye. Pogoryelov, Y. Zhou, Fred Mancoff, and Johan Åkerman. Spin torque oscillators and rf currents—modulation, locking, and ringing. *Integr. Ferroelectr.*, 125(1):147–154, 2011. doi: 10.1080/10584587.2011.574478.

[67] Takaharu Saino, Shun Kanai, Motoya Shinozaki, Butsurin Jinnai, Hideo Sato, Shunsuke Fukami, and Hideo Ohno. Write-error rate of nanoscale magnetic tunnel junctions in the precessional regime. *Appl. Phys. Lett.*, 115(14):142406, 2019.

[68] Yuri Kobljanskyj, Gennady Melkov, Konstantin Guslienko, Valentyn Novosad, Samuel D Bader, Michael Kostylev, and Andrei Slavin. Nano-structured magnetic metamaterial with enhanced nonlinear properties. *Sci. Rep.*, 2:478, 2012.

[69] Denys V Slobodianiuk, Gennadiy A Melkov, Katrin Schultheiss, Helmut Schultheiss, and Roman V Verba. Nonlinear ferromagnetic resonance in the presence of three-magnon scattering in magnetic nanostructures. *IEEE Magn. Lett.*, 10:1–5, 2019.

[70] Aryan Navabi, Yuxiang Liu, Pramey Upadhyaya, Koichi Murata, Farbod Ebrahimi, Guoqiang Yu, Bo Ma, Yiheng Rao, Mohsen Yazdani, Mohammad Montazeri, Lei Pan, Ilya N. Krivorotov, Igor Barsukov, Qinghui Yang, Pedram Khalili Amiri, Yaroslav Tserkovnyak, and Kang L. Wang. Control of spin-wave damping in yig using spin currents from topological insulators. *Phys. Rev. Appl.*, 11(3):034046, 2019.

[71] Timo B. Noack, Vitaliy I. Vasyuchka, Dmytro A. Bozhko, Björn Heinz, Pascal Frey, Denys V. Slobodianiuk, Oleksandr V. Prokopenko, Gennadii A. Melkov, Peter Kopietz, Burkard Hillebrands, and Alexander A. Serga. Enhancement of the spin pumping effect by magnon confluence process in yig/pt bilayers. *Phys. Status Solidi B*, 256(9): 1900121, 2019. doi: https://doi.org/10.1002/pssb.201900121.

[72] Alexander G Gurevich and Gennadii A Melkov. *Magnetization Oscillations and Waves*. CRC press, 1996.

[73] Boris Divinskiy, Sergei Urazhdin, Sergej O Demokritov, and Vladislav E Demidov. Controlled nonlinear magnetic damping in spin-hall nano-devices. *Nat. Commun.*, 10 (1):1–7, 2019.

[74] Yutaka Tabuchi, Seiichiro Ishino, Atsushi Noguchi, Toyofumi Ishikawa, Rekishu Yamazaki, Koji Usami, and Yasunobu Nakamura. Coherent coupling between a ferromagnetic magnon and a superconducting qubit. *Science*, 349(6246):405–408, 2015. doi: 10.1126/science.aaa3693.

[75] Dany Lachance-Quirion, Samuel Piotr Wolski, Yutaka Tabuchi, Shingo Kono, Koji Usami, and Yasunobu Nakamura. Entanglement-based single-shot detection of a single magnon with a superconducting qubit. *Science*, 367(6476):425–428, 2020. doi: 10.1126/science.aaz9236.

[76] Justin T. Hou and Luqiao Liu. Strong coupling between microwave photons and nanomagnet magnons. *Phys. Rev. Lett.*, 123:107702, Sep 2019. doi: 10.1103/PhysRevLett.123.107702.

[77] Yi Li, Wei Zhang, Vasyl Tyberkevych, Wai-Kwong Kwok, Axel Hoffmann, and Valentine Novosad. Hybrid magnonics: Physics, circuits, and applications for coherent information processing. *J. Appl. Phys.*, 128(13):130902, 2020. doi: 10.1063/5.0020277.

[78] L. Körber, K. Schultheiss, T. Hula, R. Verba, J. Fassbender, A. Kákay, and H. Schultheiss. Nonlocal stimulation of three-magnon splitting in a magnetic vortex. *Phys. Rev. Lett.*, 125:207203, Nov 2020. doi: 10.1103/PhysRevLett.125.207203.

[79] Jiahao Han, Pengxiang Zhang, Justin T. Hou, Saima A. Siddiqui, and Luqiao Liu. Mutual control of coherent spin waves and magnetic domain walls in a magnonic device. *Science*, 366(6469):1121–1125, 2019. doi: 10.1126/science.aau2610.

[80] R. D. McMichael and M. D. Stiles. Magnetic normal modes of nanoelements. *J. Appl. Phys.*, 97(10):10J901, 2005. doi: 10.1063/1.1852191.

[81] Roman Verba, Lukas Körber, Katrin Schultheiss, Helmut Schultheiss, Vasil Tiberkevich, and Andrei Slavin. Theory of three-magnon interaction in a vortex-state magnetic nanodot. *Phys. Rev. B*, 103:014413, Jan 2021. doi: 10.1103/PhysRevB.103.014413. URL `https://link.aps.org/doi/10.1103/PhysRevB.103.014413`.

[82] N Yu Grigoryeva, DA Popov, and BA Kalinikos. Dipole-exchange spin wave spectrum in an anisotropic ferromagnetic waveguide with a rectangular cross section. *Phys. Solid*

State, 56(9):1806–1816, 2014.

[83] R. E. Camley. Three-magnon processes in magnetic nanoelements: Quantization and localized mode effects. *Phys. Rev. B*, 89:214402, Jun 2014.

[84] I. Barsukov, Yu Fu, C. Safranski, Y.-J. Chen, B. Youngblood, A. M. Gonçalves, M. Spasova, M. Farle, J. A. Katine, C. C. Kuo, and I. N. Krivorotov. Magnetic phase transitions in ta/cofeb/mgo multilayers. *Appl. Phys. Lett.*, 106(19):192407, 2015. doi: 10.1063/1.4921306.

[85] S. S. P. Parkin. Systematic variation of the strength and oscillation period of indirect magnetic exchange coupling through the 3d, 4d, and 5d transition metals. *Phys. Rev. Lett.*, 67:3598–3601, Dec 1991. doi: 10.1103/PhysRevLett.67.3598.

[86] A M Gonçalves, F Garcia, H K Lee, A Smith, P R Soledade, C A C Passos, M Costa, N M Souza-Neto, I N Krivorotov, L C Sampaio, and I Barsukov. Oscillatory interlayer coupling in spin hall systems. *Sci. Rep.*, 8(1):1–6, 2018.

[87] Shinji Yuasa, Taro Nagahama, Akio Fukushima, Yoshishige Suzuki, and Koji Ando. Giant room-temperature magnetoresistance in single-crystal fe/mgo/fe magnetic tunnel junctions. *Nat. Mater.*, 3(12):868–871, 2004.

[88] Mio Ishibashi, Yoichi Shiota, Tian Li, Shinsaku Funada, Takahiro Moriyama, and Teruo Ono. Switchable giant nonreciprocal frequency shift of propagating spin waves in synthetic antiferromagnets. *Sci. Adv.*, 6(17):eaaz6931, 2020. doi: 10.1126/sciadv.aaz6931.

[89] Sarah Jenkins, Andrea Meo, Luke E Elliott, Stephan K Piotrowski, Mukund Bapna, Roy W Chantrell, Sara A Majetich, and Richard F L Evans. Magnetic stray fields in nanoscale magnetic tunnel junctions. *J. Phys. D Appl. Phys.*, 53(4):044001, nov 2020.

[90] G. Dieterle, J. Förster, H. Stoll, A. S. Semisalova, S. Finizio, A. Gangwar, M. Weigand, M. Noske, M. Fähnle, I. Bykova, J. Gräfe, D. A. Bozhko, H. Yu. Musiienko-Shmarova, V. Tiberkevich, A. N. Slavin, C. H. Back, J. Raabe, G. Schütz, and S. Wintz. Coherent excitation of heterosymmetric spin waves with ultrashort wavelengths. *Phys. Rev. Lett.*, 122:117202, Mar 2019. doi: 10.1103/PhysRevLett.122.117202.

[91] R. V. Verba, A. Hierro-Rodriguez, D. Navas, J. Ding, X. M. Liu, A. O. Adeyeye, K. Y. Guslienko, and G. N. Kakazei. Spin-wave excitation modes in thick vortex-state circular ferromagnetic nanodots. *Phys. Rev. B*, 93:214437, Jun 2016. doi: 10.

1103/PhysRevB.93.214437.

[92] Arne Vansteenkiste, Jonathan Leliaert, Mykola Dvornik, Mathias Helsen, Felipe Garcia-Sanchez, and Bartel Van Waeyenberge. The design and verification of mumax3. *AIP Adv.*, 4(10):107133, 2014. doi: 10.1063/1.4899186.

[93] J.Z. Sun and D.C. Ralph. Magnetoresistance and spin-transfer torque in magnetic tunnel junctions. *J. Magn. Magn. Mater.*, 320(7):1227–1237, 2008. doi: https://doi.org/10.1016/j.jmmm.2007.12.008.

[94] T. M. Spicer, P. S. Keatley, T. H. J. Loughran, M. Dvornik, A. A. Awad, P. Dürrenfeld, A. Houshang, M. Ranjbar, J. Åkerman, V. V. Kruglyak, and R. J. Hicken. Spatial mapping of torques within a spin hall nano-oscillator. *Phys. Rev. B*, 98:214438, Dec 2018. doi: 10.1103/PhysRevB.98.214438.

[95] C. Wang, Y.-T. Cui, J. Z. Sun, J. A. Katine, R. A. Buhrman, and D. C. Ralph. Bias and angular dependence of spin-transfer torque in magnetic tunnel junctions. *Phys. Rev. B*, 79:224416, Jun 2009. doi: 10.1103/PhysRevB.79.224416.

[96] RY Chen, RQ Zhang, LY Liao, XZ Chen, YJ Zhou, YD Gu, MS Saleem, XF Zhou, F Pan, and C Song. Magnetic field direction dependent magnetization reversal in synthetic antiferromagnets. *Applied Physics Letters*, 115(13):132403, 2019.

[97] Yizhou Liu, Igor Barsukov, Yafis Barlas, Ilya N Krivorotov, and Roger K Lake. Synthetic antiferromagnet-based spin josephson oscillator. *Applied Physics Letters*, 116 (13):132409, 2020.

[98] Anabela Veloso and Paulo P Freitas. Spin valve sensors with synthetic free and pinned layers. *Journal of Applied Physics*, 87(9):5744–5746, 2000.

[99] J.K. Han, K.H. Shin, and S.H. Lim. Thermal stability of trilayer synthetic antiferromagnets. *Journal of Magnetism and Magnetic Materials*, 310 (2, Part 3):2339–2341, 2007. ISSN 0304-8853. doi: https://doi.org/10.1016/j.jmmm.2006.11.184. URL `https://www.sciencedirect.com/science/article/pii/S0304885306024231`. Proceedings of the 17th International Conference on Magnetism.

[100] Amalio Fernández-Pacheco, Elena Vedmedenko, Fanny Ummelen, Rhodri Mansell, Dorothée Petit, and Russell P Cowburn. Symmetry-breaking interlayer dzyaloshinskii–moriya interactions in synthetic antiferromagnets. *Nature materials*,

18(7):679–684, 2019.

[101] RA Duine, Kyung-Jin Lee, Stuart SP Parkin, and Mark D Stiles. Synthetic antiferromagnetic spintronics. *Nature physics*, 14(3):217–219, 2018.

[102] Changting Dai and Fusheng Ma. Strong magnon–magnon coupling in synthetic antiferromagnets. *Applied Physics Letters*, 118(11):112405, 2021.

[103] KY Kim, SH Jang, KH Shin, HJ Kim, and T Kang. Interlayer coupling field in spin valves with cofe/ru/cofe/femn synthetic antiferromagnets. *Journal of Applied Physics*, 89(11):7612–7615, 2001.

[104] GY Shi, CH Wan, YS Chang, F Li, XJ Zhou, PX Zhang, JW Cai, XF Han, F Pan, and C Song. Spin-orbit torque in mgo/cofeb/ta/cofeb/mgo symmetric structure with interlayer antiferromagnetic coupling. *Physical Review B*, 95(10):104435, 2017.

[105] Chong Bi, Hamid Almasi, Kyle Price, Ty Newhouse-Illige, Meng Xu, Shane R Allen, Xin Fan, and Weigang Wang. Anomalous spin-orbit torque switching in synthetic antiferromagnets. *Physical Review B*, 95(10):104434, 2017.

[106] PX Zhang, LY Liao, GY Shi, RQ Zhang, HQ Wu, YY Wang, F Pan, and C Song. Spin-orbit torque in a completely compensated synthetic antiferromagnet. *Physical Review B*, 97(21):214403, 2018.

[107] Ruyi Chen, Qirui Cui, Liyang Liao, Yingmei Zhu, Ruiqi Zhang, Hua Bai, Yongjian Zhou, Guozhong Xing, Feng Pan, Hongxin Yang, et al. Reducing dzyaloshinskii-moriya interaction and field-free spin-orbit torque switching in synthetic antiferromagnets. *Nature Communications*, 12(1):3113, 2021.

[108] Z. Q. Lei, G. J. Li, William F. Egelhoff, P. T. Lai, and Philip W. T. Pong. Review of noise sources in magnetic tunnel junction sensors. *IEEE Transactions on Magnetics*, 47(3):602–612, 2011. doi: 10.1109/TMAG.2010.2100814.

[109] S. Ingvarsson, Gang Xiao, S. S. P. Parkin, W. J. Gallagher, G. Grinstein, and R. H. Koch. Low-frequency magnetic noise in micron-scale magnetic tunnel junctions. *Phys. Rev. Lett.*, 85:3289–3292, Oct 2000. doi: 10.1103/PhysRevLett.85.3289. URL `https://link.aps.org/doi/10.1103/PhysRevLett.85.3289`.

[110] L. Jiang, E. R. Nowak, P. E. Scott, J. Johnson, J. M. Slaughter, J. J. Sun, and R. W. Dave. Low-frequency magnetic and resistance noise in magnetic tunnel junctions.

Phys. Rev. B, 69:054407, Feb 2004. doi: 10.1103/PhysRevB.69.054407. URL https://link.aps.org/doi/10.1103/PhysRevB.69.054407.

[111] P. Dhagat, A. Jander, and C. A. Nordman. Correlation of telegraph noise between parallel and antiparallel states of magnetic tunnel junctions. *Journal of Applied Physics*, 97(10):10C911, 2005. doi: 10.1063/1.1851952. URL https://doi.org/10.1063/1.1851952.

[112] E. R. Nowak, R. D. Merithew, M. B. Weissman, I. Bloom, and S. S. P. Parkin. Noise properties of ferromagnetic tunnel junctions. *Journal of Applied Physics*, 84(11):6195–6201, 1998. doi: 10.1063/1.368936. URL https://doi.org/10.1063/1.368936.

[113] S. Ingvarsson, Gang Xiao, R. A. Wanner, P. Trouilloud, Yu Lu, W. J. Gallagher, A. Marley, K. P. Roche, and S. S. P. Parkin. Electronic noise in magnetic tunnel junctions. *Journal of Applied Physics*, 85(8):5270–5272, 1999. doi: 10.1063/1.369851. URL https://doi.org/10.1063/1.369851.

[114] J. M. Almeida, R. Ferreira, P. P. Freitas, J. Langer, B. Ocker, and W. Maass. 1f noise in linearized low resistance mgo magnetic tunnel junctions. *Journal of Applied Physics*, 99(8):08B314, 2006. doi: 10.1063/1.2172179. URL https://doi.org/10.1063/1.2172179.

[115] Anis Faridah Md Nor, Takeharu Kato, Sung Jin Ahn, Tadaomi Daibou, Kazunaga Ono, Mikihiko Oogane, Yasuo Ando, and Terunobu Miyazaki. Low-frequency noise in mgo magnetic tunnel junctions. *Journal of Applied Physics*, 99(8):08T306, 2006. doi: 10.1063/1.2165142. URL https://doi.org/10.1063/1.2165142.

[116] Johan J. Åkerman, J. M. Slaughter, Renu Whig Dave, and Ivan K. Schuller. Tunneling criteria for magnetic-insulator-magnetic structures. *Applied Physics Letters*, 79 (19):3104–3106, 2001. doi: 10.1063/1.1413716. URL https://doi.org/10.1063/1.141371.

[117] U. Rüdiger, R. Calarco, U. May, K. Samm, J. Hauch, H. Kittur, M. Sperlich, and G. Güntherodt. Temperature dependent resistance of magnetic tunnel junctions as a quality proof of the barrier. *Journal of Applied Physics*, 89(11):7573–7575, 2001. doi: 10.1063/1.1361055. URL https://doi.org/10.1063/1.1361055.

[118] Christopher Safranski and Jonathan Z Sun. Interface moment dynamics and its contribution to spin-transfer torque switching process in magnetic tunnel junctions. *Physical Review B*, 100(1):014435, 2019.

[119] ZQ Lei, GJ Li, William F Egelhoff, PT Lai, and Philip WT Pong. Review of noise sources in magnetic tunnel junction sensors. *IEEE Transactions on Magnetics*, 47(3): 602–612, 2011.

[120] Anis Faridah Md Nor, Takeharu Kato, Sung Jin Ahn, Tadaomi Daibou, Kazunaga Ono, Mikihiko Oogane, Yasuo Ando, and Terunobu Miyazaki. Low-frequency noise in mgo magnetic tunnel junctions. *Journal of applied physics*, 99(8):08T306, 2006.

[121] Arijit Mitra, J. Mohapatra, S. S. Meena, C. V. Tomy, and M. Aslam. Verwey transition in ultrasmall-sized octahedral fe3o4 nanoparticles. *The Journal of Physical Chemistry C*, 118(33):19356–19362, 2014. doi: 10.1021/jp501652e. URL `https://doi.org/10.1021/jp501652e`.

[122] Jisoo Lee, Soon Gu Kwon, Je-Geun Park, and Taeghwan Hyeon. Size dependence of metal–insulator transition in stoichiometric fe3o4 nanocrystals. *Nano Letters*, 15 (7):4337–4342, 2015. doi: 10.1021/acs.nanolett.5b00331. URL `https://doi.org/10.1021/acs.nanolett.5b00331`.

[123] B. Raquet, J. M. D. Coey, S. Wirth, and S. von Molnár. $1/f$ noise in the half-metallic oxides cro_2, fe_3o_4, and $la_{2/3}sr_{1/3}mno_3$. *Phys. Rev. B*, 59:12435–12443, May 1999. doi: 10.1103/PhysRevB.59.12435. URL `https://link.aps.org/doi/10.1103/PhysRevB.59.12435`.

[124] Robert de Mello Koch and Hendrik JR van Zyl. Inelastic magnon scattering. *Physics Letters B*, 768:187–191, 2017.